LEVEL STUDIES OF SOME MASS 89 NUCLEI

LEVEL STUDIES OF SOME MASS 89 NUCLEI

by

JAMES EDGAR KITCHING, B. Sc.

A Thesis

Submitted to the Faculty of Graduate Studies

in Partial Fulfilment of the Requirements

for the Degree

Doctor of Philosophy

McMaster University

October 1966

DOCTOR OF PHILOSOPHY (1967)

McMASTER UNIVERSITY
Hamilton, Ontario

TITLE: Level Studies of Some Mass 89 Nuclei

AUTHOR: James Edgar Kitching, B.Sc. (McMaster University)

SUPERVISOR: Dr. M. W. Johns

NUMBER OF PAGES: xii, 176

SCOPE AND CONTENTS:

The decay of 14.9 min. ^{89}Rb to levels in ^{89}Sr has been studied by use of Ge(Li) detectors, NaI(Tl) detectors and a magnetic beta ray spectrometer. Fourteen gamma rays have been studied by γ-γ and β-γ coincidence experiments and establish levels at 0, 1.031, 2,000, 2.277, 2.567, 2.708, 2.770, 3.225 and 3.500 MeV. The Q value is 4.486 $\pm$ .012 MeV.

The techniques of beta and gamma ray spectroscopy using Ge(Li), NaI(Tl) and plastic beta detectors have been applied in the study of the decay of 3.2 min. ^{89}Kr to levels in ^{89}Rb. Seventy nine of the one hundred and eleven observed gamma rays have been classified in the proposed decay scheme. The Q value is 5.15 $\pm$ .03 MeV.

ACKNOWLEDGEMENTS

I wish to express my indebtedness to Professor M.W. Johns for his patience, encouragement and scholarly insight which have guided me during the years of my stay at this university. To the members of my supervisory committee, Dr. G. L. Keech and Dr. R.D. Macfarlane, I wish to express my gratitude.

The many valuable discussions and generous assistance provided me by the members of the beta and gamma ray spectroscopy group, with whom I have been associated, is gratefully acknowledged. Without their help many phases of this work would have been impossible. I would like to thank Dr. T. J. Kennett and his research group for the use of many of their experimental facilities and for help in carrying out some of the experiments. Their criticism of some of the work contained in this thesis has been most valuable. The assistance of Professor R. H. Tomlinson and Dr. J. Fiedler in the chemical aspects of this work is gratefully acknowledged.

It is a pleasure to thank the staffs of the McMaster reactor and the computation centre for their assistance in the inumerable sample irradiations and the running of the computor programmes used in this study.

The accurate typing of Mrs. Helen Kennelly and her uncanny ability to decipher my handwriting have been invaluable in the preparation of this thesis; to her I am greatly indebted.

To my wife, Marie, and to my son and daughter, Allan and Jamie, I owe a special thanks for their encouragement and understanding and for their

toleration of the amount of time which was devoted to this study.

This work has been financially supported by the National Research Council of Canada.

TABLE OF CONTENTS

LIST OF TABLES

LIST OF FIGURES

CHAPTER I

INTRODUCTION

Nuclear phenomena involve three of the four known forces; the strong, weak, and electro-magnetic interactions. The weak and electromagnetic interactions have now been adequately described and have become the prime means of investigating the strong interactions. This interaction, despite the efforts of physicists for the past seventy years, is still lacking in an adequate description. Furthermore a complete description of nuclear phenomena must involve the interplay of the three forces as well as embody the conservation principles that are apparent in the physical universe.

Nuclear phenomena belong to the sub-atomic domain and as such the mode of description is cast in the language of the quantum theory. The ideas making up this theory have been continuously evolving since the turn of the century. Despite the fact it is not complete in all respects this theory has been successful in describing a vast quantity of physical phenomena .

The decay processes of finite nuclei are concerned with the three forces and therefore a brief description of each is given below.

a The Weak Interaction

The weak interaction manifests itself in nuclei in the beta decay process. For radioactive decay the emitted beta particles form a continuous distribution from zero to the maximum beta energy available. This distribution appears to violate the conservation of energy and was

first explained by Pauli[1] in 1933 by the postulate of the existence of the neutrino. This particle was finally detected by Cowan and Reines[2] in 1957. The description of the beta decay process was first described by Fermi[3] in 1934. In this process, an electron-neutrino pair (the Leptons) is ejected from the nucleus with a consequent rearrangement of the nuclear charge and internal structure. An allowed beta transition is one in which no orbital angular momentum is carried off by the Leptons. Transitions in which one, two etc. units of orbital angular momentum are carried off are classified as first, second, etc. forbidden transitions. Forbidden transitions are much less probable than allowed ones, and can normally be observed only when the spins and parities of the initial and final nuclear states strictly forbid the allowed transitions. Moreover these spectra will not normally have the allowed or statistical shape.

Mathematically the beta decay process may be written as[4]

$$N(p)dp = g^2 \frac{m^5c^4}{2\pi^3\hbar^7} |M_{if}|^2 F(z,p)(W_o-W)^2 S_n(z,p)\, p^2 dp \qquad (1)$$

Here $N(p)dp$ is the probability that the beta particles are emitted between p and p + dp where p is their momentum and g^2 is the coupling constant for the beta decay process.

$|M_{if}|$ is the matrix element of the transition and $S_n(z,p)$ is the "shape factor"[5] dependent on the order of forbiddenness.

For an allowed transition

$$S_o(z,p) = 1$$

$F(z,p)$ is the electron screening function which is due to the effect of the Coulomb field of the nucleus on the emerging electrons.

The probability of decay, λ, is obtained by integrating (1) over all permitted values of momentum to give

$$\lambda = \text{const}^* |M_{if}|^2 f(z,p)$$

or $$ft = cons/|Mif|^2$$

where

$$f(z,p) = \int_0^{pmax} F(z,p)(W_o - W)^2 S_n(z,p) p^2 dp \ .$$

f can be expressed analytically for allowed transitions where $S_o = 1$; for forbidden transitions it is more difficult to express f_1, f_2 etc and these are usually evaluated in terms of f_o.

The quantity ft is inversely proportional to the square of the matrix element. The ft values are dependent on the degree of forbiddeness of the decay process; characteristically a change of one in the order of forbiddeness will cause the ft value to change by about two orders of magnitude.

A rigorous treatment[6] of the process is relativistic and as such involves four component spinors. The Hamiltonian must be a scalar and therefore the spinors are combined in various ways to form the final scalar. When the condition of relativistic invariance is imposed, five possible combinations exist: the scalar, the vector, the tensor, the axial-vector and the pseudo-scalar. Of these, experiments[4] have shown that only the vector and axial vector combinations occur in nature. In these decay processes the Leptons may be emitted in either the singlet or triplet states. The situation is summarized in the table below for the simplest selection rules.

Interaction Type	Allowed		1st Forbidden		2nd Forbidden	
	$\Delta\pi$	ΔJ	$\Delta\pi$	ΔJ	$\Delta\pi$	ΔJ
(Singlet) Vector	No	0	Yes	1,0	No	2
(Triplet) Axial Vector	No	1,0	Yes	0,1,2*	No	1,2,3*

TABLE 1
Beta Decay Selection Rules

The two entries marked with an asterisk are said to be "unique" transitions. For these, the shape factors, $S_n(z,p)$, are uniquely defined and sharply different from $S_o(z,p)$. For the other forbidden transitions $S_n(z,p)$ involves the summation of a number of terms which results in cancellations that make $S_n(z,p)$ almost indistinguishable from $S_o(z,p)$. The log ft values for a given type of spectrum is a slowly changing function of nuclidic mass. The average over all masses[7] for allowed is 5.7 ± 1.1, for first forbidden 7.5 ± 1.5, for first forbidden unique 8.5 ± 0.7, and for second forbidden 12.1 ± 1.0. It is more meaningful to look at the mass region of immediate concern to this thesis. Figure 1 displays a histogram of the experimental log ft values in the mass range 80 to 100. Since this region crosses a closed shell the distribution is not truly representative of the mass 89 region but unfortunately to limit the region more sharply would make the sample statistically unusable.

b The Electro-Magnetic Interaction

The electro-magnetic interaction is well described by Maxwell's equations and the concepts of quantum electrodynamics. It can therefore be used with confidence as one of the most important tools of nuclear physics. Since the radiated field characteristic of gamma radiation is electromagnetic in origin, it carries off angular momentum and has an angular distribution pattern which depends on the parity and on the amount of angular momentum in the field.

The transition probability, T, of an electromagnetic transition of energy $\hbar\omega$, which carries off ℓ units of angular momentum can be written as[6]

DISTRIBUTION OF LOG FT VALUES FOR $80 \leq A \leq 100$

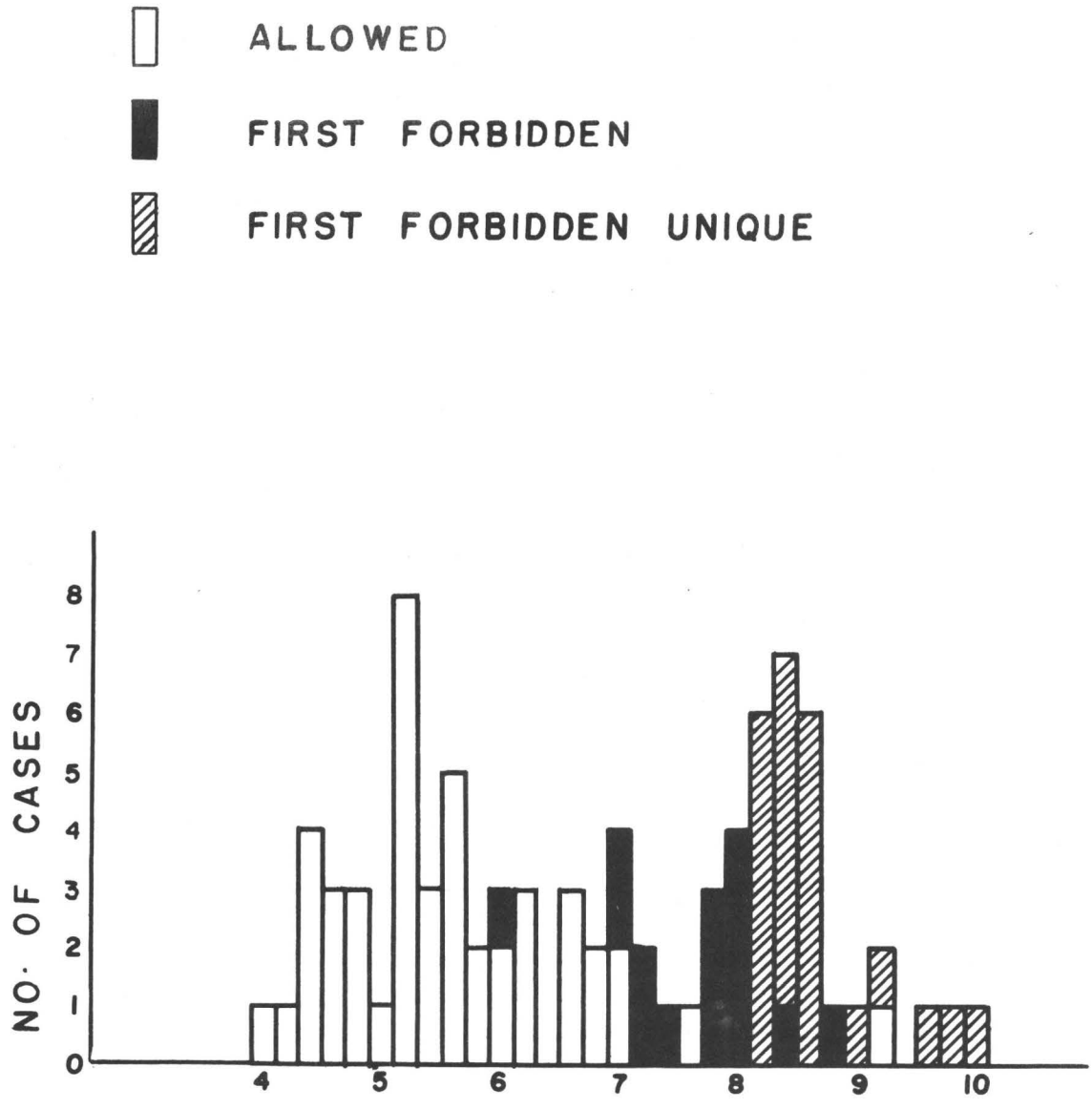

FIGURE 1

$$T(\sigma,\ell) = \frac{8\pi(\ell+1)}{\ell\left[(2\ell+1)!!\right]^2}\left(\frac{k^{2\ell+1}}{\hbar}\right) B(\sigma,\ell)$$

where $k = \frac{\omega}{c}$ and σ is labelled E or M for electric or magnetic transitions respectively.

The term $B(\sigma,\ell)$ is the reduced matrix element of the transition and involves the electro magnetic operator and a knowledge of the initial and final nuclear wave functions. The selection rules restrict the spins and parities of the states coupled by this transition to

$$|J_i - J_f| \leq \ell \leq |J_i + J_f|$$

$$\pi_i \pi_f = (-)^\ell \text{ for } E\ell \text{ transitions}$$

$$= -(-)^\ell \text{ for } M\ell \text{ transitions.}$$

The quantity $B(\sigma,L)$ may be evaluated by use of nuclear wave functions obtained from a model. The simplest possible model to assume is that the transition is due to the vibration of a single nuclear proton. The transition probabilities derived on this assumption are called the single particle or **Weiskopf**[8] estimates. Actual transition rates are conveniently expressed in terms of these "Weiskopf units". If one assumes that the reduced transition probabilities for gamma ray transitions of the same multipole order are the same then it is apparent that the relative intensities of such transitions originating in a common nuclear level will be proportional to $\left(\frac{E_1}{E_2}\right)^{2\ell+1}$.

The multipolarity of the radiations may also be obtained by the study of the angular distribution of the emitted radiation or by the method of internal conversion[9]. In the internal conversion process, the nuclear transition energy is given directly to a bound electron in the atom which is thereupon emitted with an energy equal to the transition

energy less the binding energy of the electron. The competition between gamma ray and conversion electron emission is a strong function of multipole order, emission energy, and of atomic number. In the low Z nuclides discussed in this thesis the transitions are expected to be dipole in character and of high energy, thus the intensities of the conversion electrons are expected to be low.

The angular correlation pattern[9] between successive gamma ray transitions is most easily interpreted when the transition energies are large and the lifetime of the intermediate states are small. These conditions are well satisfied for the nuclides of interest here. The probability of emission of a photon is generally a function of the angle between the emission direction and the nuclear spin axis. At very low temperatures an assemblage of radioactive nuclei may be partially aligned and the angular correlation pattern of the emitted photons directly observed. At normal temperatures no such alignment is possible with the result that the probability of emission is an isotropic function of direction. The coincidence rate between cascading radiations is generally a function of the angle between the two emitted radiations and depends on the multipole order of the radiations and the spins of the initial, final and intermediate states. This correlation results from an uneven population of magnetic substates of the intermediate level brought about by detecting the initial photon in the Z direction. A change of $\pm$ 1 in the Z component of angular momentum must occur for emission in this direction with the result the second radiation is emitted from a level of unequally populated magnetic substates. This uneven population results in an angular correlation function which is

mathematically described by[6]

$$W(\theta) = \sum_{n=0}^{N} A_{2n} P_{2n} (\cos \theta)$$

Here N is the minimum of (ℓ, $J_{int.}$, ℓ_2) and θ is the angle between the two emissions. P_{2n} is the usual legendre polynomials while A_{2n} is a function of Clebsch-Gordon and Racah coefficients. The possibility of the transitions proceeding by mixed modes may also be included in these coefficients. The method of angular correlations cannot distinguish between magnetic or electric transitions.

c The Strong Interaction

The nuclear force involves the interaction of nucleons and as such is held responsible for observed phenomenon involving clusters of from two to a few hundred nucleons. A description of this interaction must therefore account for a large body of data extending from two body nucleon-nucleon scattering to the structure of finite nuclei.

The two body scattering data represents information concerning the nuclear interaction in its simplest form. This data has been described by a large number of "potentials"[10] some of which yield reasonably good fits over a wide range of energy. In addition, potentials which fit this data have been successful in fitting simple finite systems such as the deuteron and triton. However, no unique potential exists at the present time. Potentials in use indicate that any description of the nuclear interaction must contain (a) a repulsive core (b) a tensor component (c) at least the one pion exchange and (d) a spin orbit term.

The application of nucleon-nucleon potentials to the many particle configurations characteristic of finite nuclei has proved to be very difficult. From the experimental point of view, any theory of nuclear forces

must account for a number of deductions arising from observations concerning actual nuclei. The nuclear force must (i) be approximately charge independent (ii) be short range (iii) be saturable and (iv) be capable of accounting for the large spin orbit effect in real nuclei. Brueckner et al[11,12,13,14] have pioneered the application of potentials which fit the scattering data to the many nucleon problem, however this approach is still in the developmental stage. More useful descriptions of real nuclei have resulted from the "model" approach in which most of the nucleon-nucleon interaction effects are absorbed in an inert core. At the present time no one model is applicable to all nuclei; in fact it may be necessary to use several models to account for the phenomenon observed in a single nuclide.

d The Shell Model - Particle excitations in a spherical potential well.

The shell model was postulated in 1947[15,16] in analogy with atomic phenomenon. In order to account for the observed structure it was necessary to postulate both a central field and a strong L.S coupling forces. This model suggests that the predominant angular momentum coupling mode is J-J in character and that the potential can be written as $V(r) = V_o + V_1 (L.S)$. The potential used is intermediate between a square well and a harmonic oscillator and the levels, for a given ℓ value, are split in two with $j = \ell + s$ and $j = \ell - s$. The splitting between levels of the same ℓ value increases rapidly with ℓ, and the $\ell + s$ state of the pair is depressed to lower excitations. The order of filling is determined by the excitation energy of the levels and by Pauli's principle. The basic tenets of the model are;

(1) Protons and neutrons fill shells independently.

(2) The spin of the nucleus is usually due to the unpaired nucleon.

(3) The nucleons tend to form zero spin pairs.

(4) A closed shell configuration is abnormally stable.

This model regards all nucleons in a shell are degenerate and does not account for vibrational and rotational excitations. More modern treatments of the shell model[17] include a residual interaction to remove the degeneracy within the j orbitals. The residual interaction plus the use of Racah algebra has enabled the shell model to be applied in a quantitative manner to the prediction of excited states, binding energies, etc. The concept of seniority has been shown[18,19] to be of importance in regard to the form the residual interaction may take. If seniority is a good quantum number the residual interaction is limited to a bilinear function of the spin operators σ_1 and σ_2. For example seniority is found to be a good quantum number[20] for the proton $g_{9/2}^{n-2}\ p_{1/2}^{2}$ configuration in the zirconium isotopes. A test of this quantum number for similar neutron configurations in the strontium isotopes is hampered by lack of experimental data.

e The Nilsson Model - Particle Motion in a deformed potential well.

The coupling of a non-spherical potential well to the shell model leads to the Nilsson model[21] which has a Hamiltonian of the form

$$H = \frac{p^2}{2m} + \frac{m}{2}(\omega_x^2 X^2 + \omega_y^2 Y^2 + \omega_z^2 Z^2) + C\ \ell.s + D\ell^2$$

In this expression, the first term is the kinetic energy; the second is the anharmonic oscillator energy, the third is the $\ell.s$ force contribution and the last term is arbitrarily included to reduce the energy of the higher angular momentum states. In such a deformed potential only one pair of particles may be placed in each state and the level

filling order is dependent on the degree of deformation of the particular nucleus under study.

f Vibrational Motion

In addition to single particle motions a large number of nucleons may contribute to collective effects which manifest themselves in vibrational and rotational degrees of freedom. In particular, oscillations of the nucleus about the equilibrium shape occur for low energy excitations in the form of quadrupole and octopole vibrations. In the first approximation the oscillations are treated as harmonic in analogy with the classical liquid drop. Since the oscillations are harmonic the levels are equally spaced of separation $\hbar\omega$. The states are degenerate and have angular momentum 2 for the one phonon state; 0, 2 and 4 for the two phonon state and so on. Any anharmonic component removes the degeneracy of the levels. Such anharmonic components may arise from coupling of the vibrational motion to other excitation modes.

For quadrupole excitations large reduced E2 transition probabilities occur between adjacent levels; the existence of which is interpreted as evidence for collective motion. The strontium and krypton isotopes at or below the closed 50 neutron shell have well developed vibrational levels. The stable $^{88}_{35}Sr_{50}$ isotope shows octopole vibrations in addition to vibrations of quadrupole character.

g Rotational Motion

It is found that in some mass regions unusually large quadrupole moments exist and level sequences similar to those expected for a rigid rotator are found. These observations have led to the construction of a rotational model[22] for nuclear structure. This model assumes a

non-spherical nuclear surface rotating about an axis perpendicular to the symmetry axis. The motion of the nucleons may be viewed either as a rigid rotator or as a system undergoing irrotational fluid flow. Experimentally one finds that the behaviour of real nuclei corresponds to a picture intermediate between these extremes.

For an even-even system the energy can be written as

$$E_{rot} = \frac{\hbar^2}{2\mathcal{I}} J(J+1)$$

where J = 0 for the ground state and 2,4,6 etc for successive excited states. The level spacings given by this formulae are in good agreement with experiment for nuclei in the rare earth region. This agreement may be improved by adding a second anharmonic term in $[J(J+1)]^2$. For odd A nuclei, the level spacing is interpreted as being due to the coupling of the even-even core to the odd particle. The energy of such a system is written as

$$E_{rot} = \frac{\hbar^2}{2\mathcal{I}} \left[J(J+1) + a(-)^{J+\frac{1}{2}} (J+\tfrac{1}{2})\, \delta_{\Omega,\frac{1}{2}} \right]$$

where $J = \Omega, \Omega+1$ etc. and

$$a = \sum_j (-1)^{j-\frac{1}{2}} (j+\tfrac{1}{2}) |C_j|^2 \qquad \text{and } |C_j|^2$$

is the probability that the last added particle has angular momentum j. In this expression δ is the usual Kronecker delta function, and Ω represents the coupling of the angular momentum of the individual particles to the angular momentum of the core.

h Pairing Model ÷ particle-particle and particle-vibrational coupling.

The pairing force[23] is similar in character to a delta function force $V_{12}\delta(r_1-r_2)$. However, it interacts only on conjugate pairs (ie those

with m values of the same magnitude but of opposite sign) and does not require the particles to be in close proximity in order to act. Such a long range force accounts for the collective behaviour of nuclear matter. Bardeen, Cooper and Schrieffer[24] have shown that in a Fermion system no matter how weak the pairing force a gap in energy will be in evidence between the ground and first excited states. In a many Fermion system without pairing effects, the potential well is filled to the Fermi level. In the presence of a strong pairing force, such as the seniority coupling scheme, the levels are filled in pairs. The actual pairing force lies between these extremes with the Fermi surface being slightly diffuse because particles near the surface are scattered in pairs to higher levels.

For an even-even system of nucleons the ground state wave function is formed as the sum of wave functions for states with two, four and higher particle excitations. The Hamiltonian is not diagonal in this scheme and therefore a canonical transformation is carried out leaving the Hamiltonian approximately diagonal. In this treatment particle and hole states can no longer be identified; both being replaced by quasi particles. The energy of a single quasi particle in the j^{th} orbital is given by[26]

$$E = \sqrt{(\varepsilon_j - \lambda)^2 + \Delta^2}$$

where ε_j is the single particle excitation energy;

λ is the chemical potential or Fermi energy; and

Δ is the gap energy - the energy required to break a pair.

The wave function of the system is

$$\psi_N = \prod (U_{jm} + V_{jm}\, a^+_{jm}\, a^+_{j-m}) \,|0\rangle$$

where $U^2_{jm} + V^2_{jm} = 1$.

In this description U^2_{jm} is the probability of finding a quasi particle state unfilled and V^2_{jm} the probability of finding it filled. a^+_{jm} and a^+_{j-m} are creation operators operating on the vacuum state. $|0\rangle$

The U^2_j and V^2_j are expressed in terms of the other parameters as

$$U^2_{jm} = \tfrac{1}{2}\left(1 + \frac{\epsilon_j - \lambda}{E_j}\right), \quad V^2_{jm} = \tfrac{1}{2}\left(1 - \frac{\epsilon_j - \lambda}{E_j}\right)$$

and $V_{jm}\, U_{jm} = \dfrac{\Delta}{2E_j}$

Particle-vibrational coupling is introduced into the model by means of a long range quadrupole force[27]. The effect of the pairing force is to maintain spherical stability while the quadrupole force tends to deform the nucleus.

CHAPTER II

FISSION PRODUCTS AND EARLY WORK ON KRYPTON AND RUBIDIUM ISOTOPES

(a) Fission

The phenomenon of fission, the splitting of a heavy nucleus into medium weight nuclei, was discovered by Hahn and Strassman[28,29]. This process was given its name by Meitner and Frisch[30] who were the first to correctly interpret the work of Hahn and Strassman. The concept of a fission yield curve, the probability of a nuclide of atomic mass A being formed in fission, was introduced by Fermi[31] who carried out one of the first studies of this quantity. Figure 2 shows typical fission yield curves for U^{233} and Pu^{239}[32]. It is apparent from these figures that large changes in yield occur for relatively small changes in the mass of the fissile material. In addition to these gross changes it was soon recognized[33] that fine structure exists on the curves and that part of this structure was related to delayed neutron emission from fission products[34,35].

For a given mass, the probability of finding a specific Z value in spontaneous fission is given by

$$P(z) = \frac{1}{\sigma\sqrt{2\pi}} \exp - \frac{(Z-Zp)^2}{2\sigma^2}$$ where

the variance of the distribution, σ, is ~ 0.59[36] and Z_p is the most probable charge for a given mass chain.

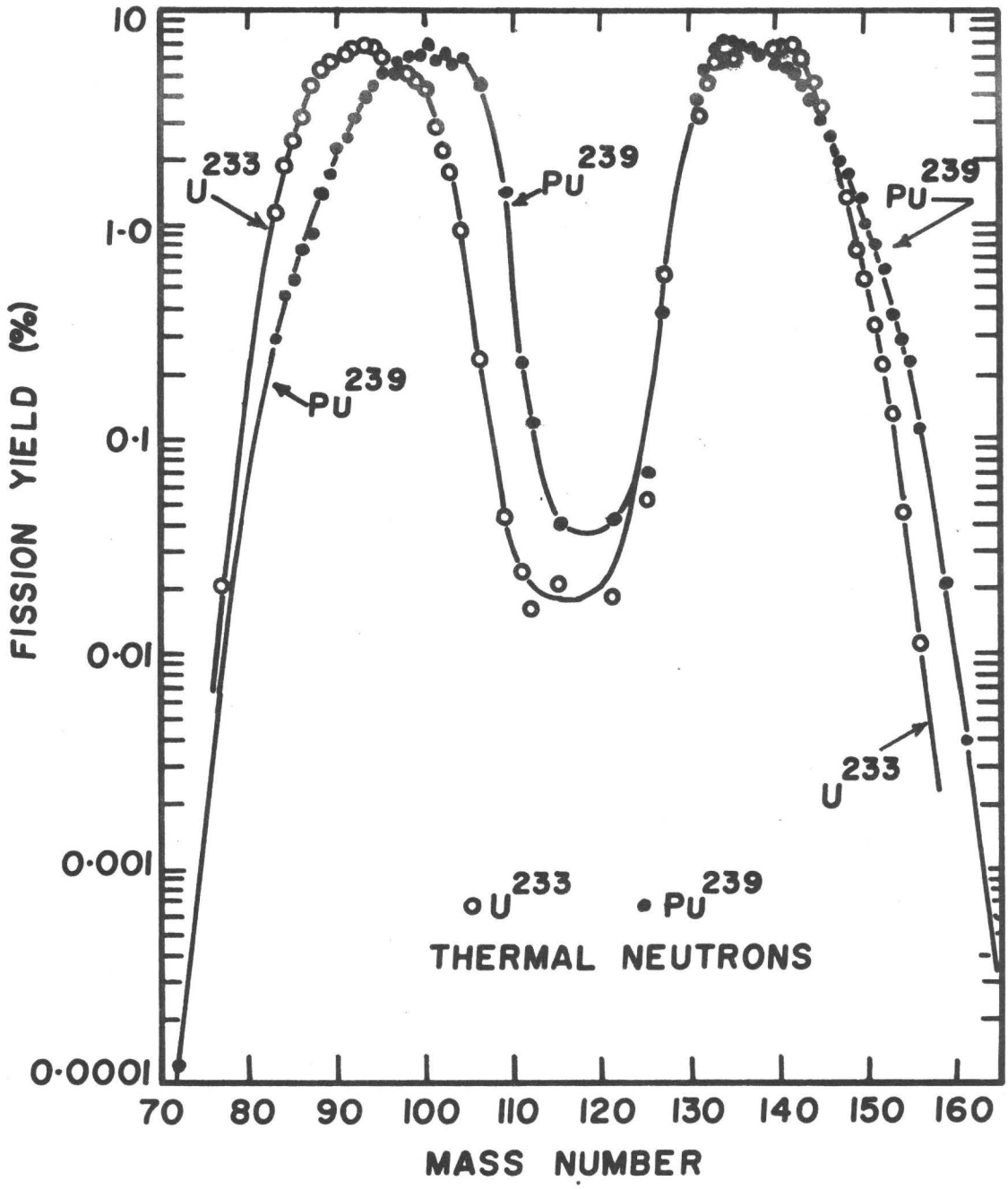
10
1·0
0·1
0·01
0·001
0·0001
FISSION YIELD (%)
U233
PU239
PU239
PU239
U233
o U233
• PU239
THERMAL NEUTRONS
70
80
90
100
110
120
130
140
150
160
MASS NUMBER

FIGURE 2

This expression was first derived by Glendenin[37]. The half lives of the nuclides in the short lived krypton decay chains are shown in Table 2. Fractional cumulative yields for the krypton isotopes as well as other pertinant information concerning the relative fission yields of ^{233}U, ^{235}U and ^{239}Pu are presented in Table 3.

(b) Properties of Fission Products

Heavy fissionable nuclei have a neutron excess due to the Coulomb force. In the fission process lower mass nuclei are formed with a neutron excess relative to stable nuclei and therefore decay by beta emission. An isobaric plot of mass versus Z leads to a parabolic curve with the most stable nuclide falling at or near the minimum. For an even A nuclide two parabolic curves occur for a given mass due to the pairing energy gain of an even-even system over an odd-odd system. It was first shown by Glueckauf[46] that a similar but smaller effect occurs for odd A nuclei reflecting the difference between the neutron and proton pairing strengths. This effect is small and is neglected in the discussion below. For an odd A system the decay energy between neighbouring nuclei is given by $\Delta E = b(Z - Z_o)$[47] where Z_o is the Z value for the parabolic minimum. This relationship results from the parabolic nature of the isobaric mass plots. This equation clearly indicates that for nuclei far removed from stability, large Q values will be in evidence. Similar equations hold for the case of even A systems.

From this analysis, one may draw certain conclusions for nuclides far removed from stability. In the first place the decay energy will eventually exceed the neutron binding energy and spon-

TABLE 2

Krypton Isotope Decay Chains

(a) $^{95}Kr \xrightarrow{\text{(short)}} {}^{95}Rb \xrightarrow{\leq 2.5\ \text{sec}} {}^{95}Sr \xrightarrow{33\ \text{sec}} {}^{95}Y \xrightarrow{10.9\ \text{min}}$

(a) $^{94}Kr \xrightarrow{\leq 1\ \text{sec}} {}^{94}Rb \xrightarrow{2.4\ \text{sec}} {}^{94}Sr \xrightarrow{82\ \text{sec}} {}^{94}Y \xrightarrow{20\ \text{min}}$

(a) $^{93}Kr \xrightarrow{1.17\ \text{sec}} {}^{93}Rb \xrightarrow{5.1\ \text{sec}} {}^{93}Sr \xrightarrow{7.54\ \text{min}} {}^{93}Y \xrightarrow{10.25\ \text{hr}}$

(a) $^{92}Kr \xrightarrow{1.92\ \text{sec}} {}^{92}Rb \xrightarrow{4.1\ \text{sec}} {}^{92}Sr \xrightarrow{2.71\ \text{hrs}} {}^{92}Y \xrightarrow{3.53\ \text{hrs}}$

$^{91}Kr \xrightarrow{8.4\ \text{sec}}{}^{(b)} {}^{91}Rb \xrightarrow{72\ \text{sec}} {}^{91}Sr \xrightarrow{9.7\ \text{h}} {}^{91}Y \xrightarrow{59\ \text{d}}$

$^{90}Kr \xrightarrow{32\ \text{sec}}{}^{(b)} {}^{90}Rb \xrightarrow{2.91\ \text{min}} {}^{90}Sr \xrightarrow{28\text{Y}} {}^{90}Y \xrightarrow{64\ \text{hrs}}$

$^{89}Kr \xrightarrow{3.1\ \text{min}}{}^{(b)} {}^{89}Rb \xrightarrow{14.9\ \text{min}} {}^{89}Sr \xrightarrow{50.4\text{d}} {}^{89}Y \xrightarrow{\text{Stable}}$

$^{88}Kr \xrightarrow{2\ \text{hr}} {}^{88}Rb \xrightarrow{18\ \text{min}} {}^{88}Sr \xrightarrow{\text{Stable}}$

$^{87}Kr \xrightarrow{76\ \text{min}} {}^{87}Rb \xrightarrow{4.7\times10^{10}\text{Y}} {}^{87}Sr \xrightarrow{\text{Stable}}$

$^{86}Kr \xrightarrow{\text{Stable}}$

(a) Half lives in these chains from the compilation of ref. (38)

(b) from ref. (39)

(c) Remaining half lives from ref. (7)

TABLE 3

Comparison of Fission Properties for
^{233}U, ^{235}U and ^{239}Pu

	+Fractional Cumulative Yield[30,40]			% Thermal Yield for Most Stable Mass in chain[a]		
	^{233}U	^{235}U	^{239}Pu	^{233}U	^{235}U	^{239}Pu
^{95}Kr	4×10^{-4}	1.1×10^{-3}	2.4×10^{-3}	6.11	6.27	5.03
^{94}Kr		.015		6.68	6.40	4.48
^{93}Kr	.023	.075	.021	6.98	6.45	3.97
^{92}Kr	.127	.312	.113	6.64	6.03	3.14
^{91}Kr	.33	.59	.31	6.43	5.84	2.61
^{90}Kr	.67	.86	.64	6.43	5.77	2.25
^{89}Kr	.86	.96	.86	5.86	4.79	1.71
^{88}Kr	.95*	.97*	.99*	5.37	3.57	1.42
^{87}Kr	.99*	1.0*	1.0*	4.56	2.49	0.92
^{86}Kr	1.0*	1.0*	1.0*	3.27	2.02	0.76

Total Cross Section in Barns: ^{233}U (524)[43], ^{235}U (580)[44], ^{239}Pu (754)[45]

(a) From the compilation of ref. (41)

* Estimated from ref. (42)

\+ The fractional cumulative yield of a given nuclide is the fraction of the cumulative yield which is created by the decay of that nuclide.

taneous neutron emission will result. In the second place because the level density increases rapidly with excitation energy a large number of levels are open to population. The deexcitation of many of these levels will proceed directly to the ground state by gamma radiation and the stopover transitions may be expected to be rather weak. The decay schemes of such nuclei are expected to be very complex. Finally, because the probability of beta decay is approximately proportional to ρ^5_{max} where ρ_{max} is the maximum momentum of the emitted particle, one may expect these nuclides to have short half lives. For most of these nuclides which are highly unstable little information aside from half-lives is known.

(c) Early Work on Krypton Isotopes

Because the krypton and xenon fission products are chemically inert, they are easily separated from other fission products but difficult to separate from each other. Dillard et al[48], by passing an unseparated mixture of krypton and xenon over a moving charged wire were able to determine the half lives of the gas fission products by measuring the distribution of decay products along the wire. These workers obtained half lives for all the krypton isotopes from mass 89 to 97. Koefoed-Hansen and Nielson[49] used a mass separator to determine the half lives and beta end points of the krypton isotopes of mass numbers 89, 90 and 91.

Gas sweeping techniques were developed fairly early in the study of fission yields. These techniques were used with highly emanating compounds of fissile material in the study of krypton and their rubidium daughter products. Wahl et al[50] determined fractional cumulative yields of short lived krypton isotopes by use of highly

emanating sterate compounds. Prakash[51], using a solution of uranyl nitrate and gas sweeping techniques based on differential absorption made an early gamma ray spectrum study of ^{89}Kr and postulated the decay scheme shown in Figure 3. Koch and Grady[52] first applied gas chromatography using activated charcoal to separate xenon and krypton gas fractions. Using their techniques Wahlgren and Meinke[52] made the first extensive study of the gamma spectra of short lived krypton activities. These workers were able to make "core to counter" separations in about 24 seconds and obtained the gamma spectra of various nuclides including ^{89}Kr and ^{90}Kr. Ockenden and Tomlinson[54] combined the emanating power of uranyl stearate compounds with the techniques of gas chromatography to produce krypton samples separated in 10 seconds. A diagram of the apparatus used by these workers is shown in Figure 4. Their results are in essential agreement with those of Wahlgren et al. as is shown in Table 4. Goodman, Kitching and Johns[55] applied coincidence techniques using the apparatus of Ockenden and Tomlinson, to study the decay of ^{90}Kr to levels in ^{90}Rb. Their decay scheme is shown in Figure 5.

(d) Early Work on Rubidium Isotopes

Seelman-Eggebert et al[56] were the first workers to identify rubidium as a daughter product of a rare gas precursor. Hahn and Strassman[57], using a mass separator, assigned a 15 minute activity as ^{89}Rb and a 2.7 minute activity as ^{90}Rb. Glasoe and Steigman[58] further investigated the properties of ^{89}Rb by aluminum absorption techniques, and postulated a beta end point of 3.8 MeV. This end point was recalculated by Bleuler and Zunti[59] who proposed a Q value

DECAY OF ^{89}Kr (PRAKASH 1960)

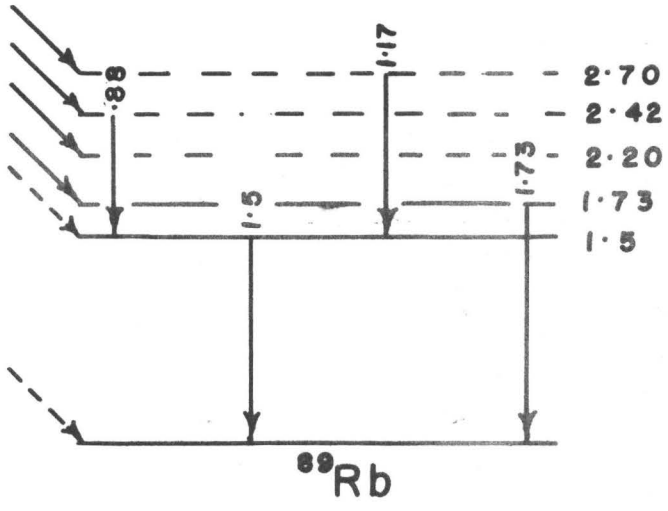

FIGURE 3

SOME EARLIER MEASURMENTS OF ^{89}Kr GAMMA RAYS

ENERGY	0·215	0·375	0·430	0·510	0·595	0·730	0·880	1·12	1·32
INTENSITY	80	35	33	49	100	39	58	50	34
WAHLGREN (1961)	1·52	1·67	1·90	2·05	2·23	2·35	2·62	2·70	2·85
	70	31	16	26	14	25	8·0	5·7	18
ENERGY	0·23	0·36	0·43	0·51	0·60	0·74	0·88	1·12	1·29
INTENSITY	85	28	29	42	100	32	65	45	31
OCKENDEN (1962)	1·51	1·71	1·93	2·04	2·23	2·42	2·57		2·84
	88	34	10	16	10	22	10		25

TABLE 4

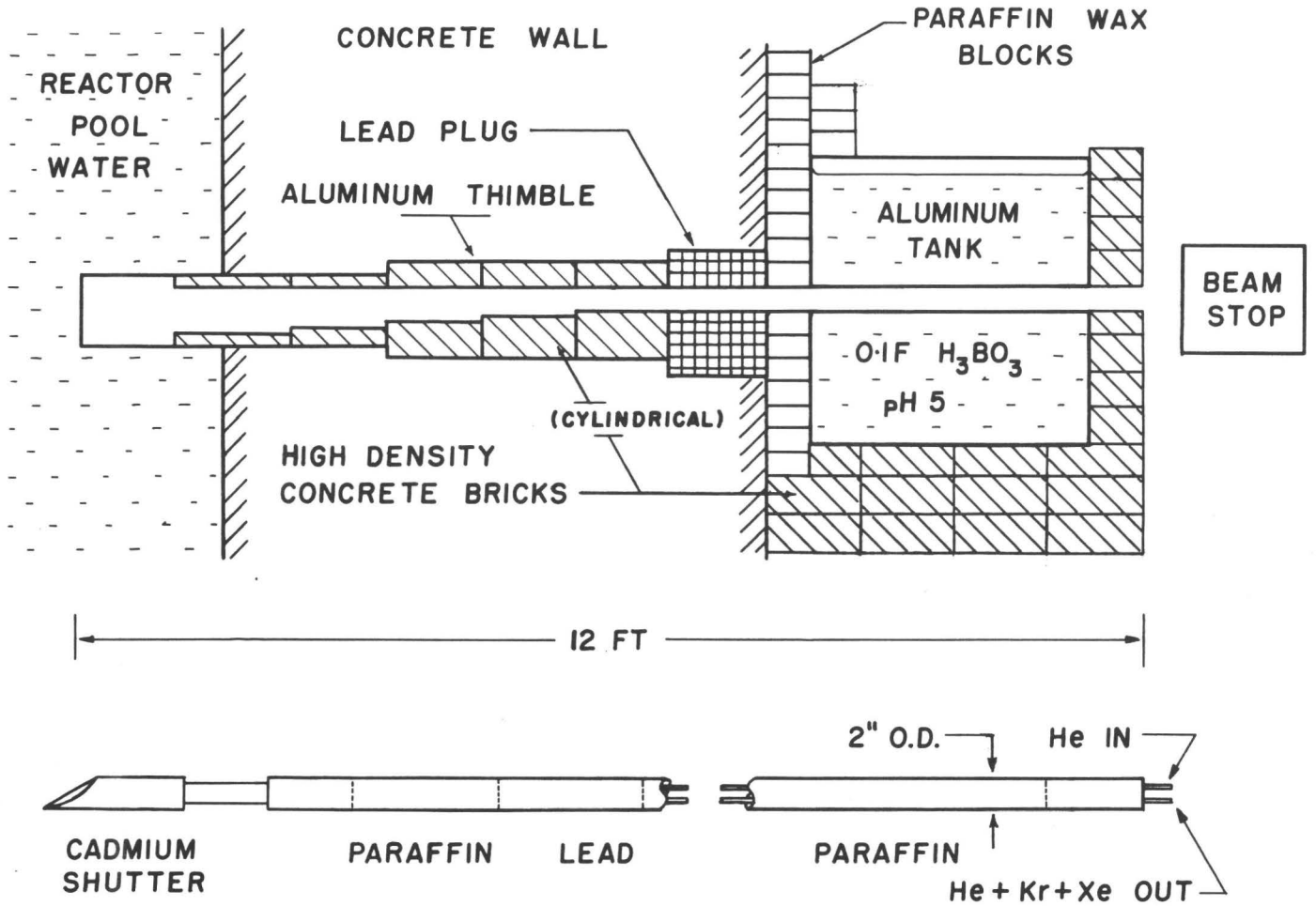

CROSS SECTION OF BEAM PORT

FIGURE 4

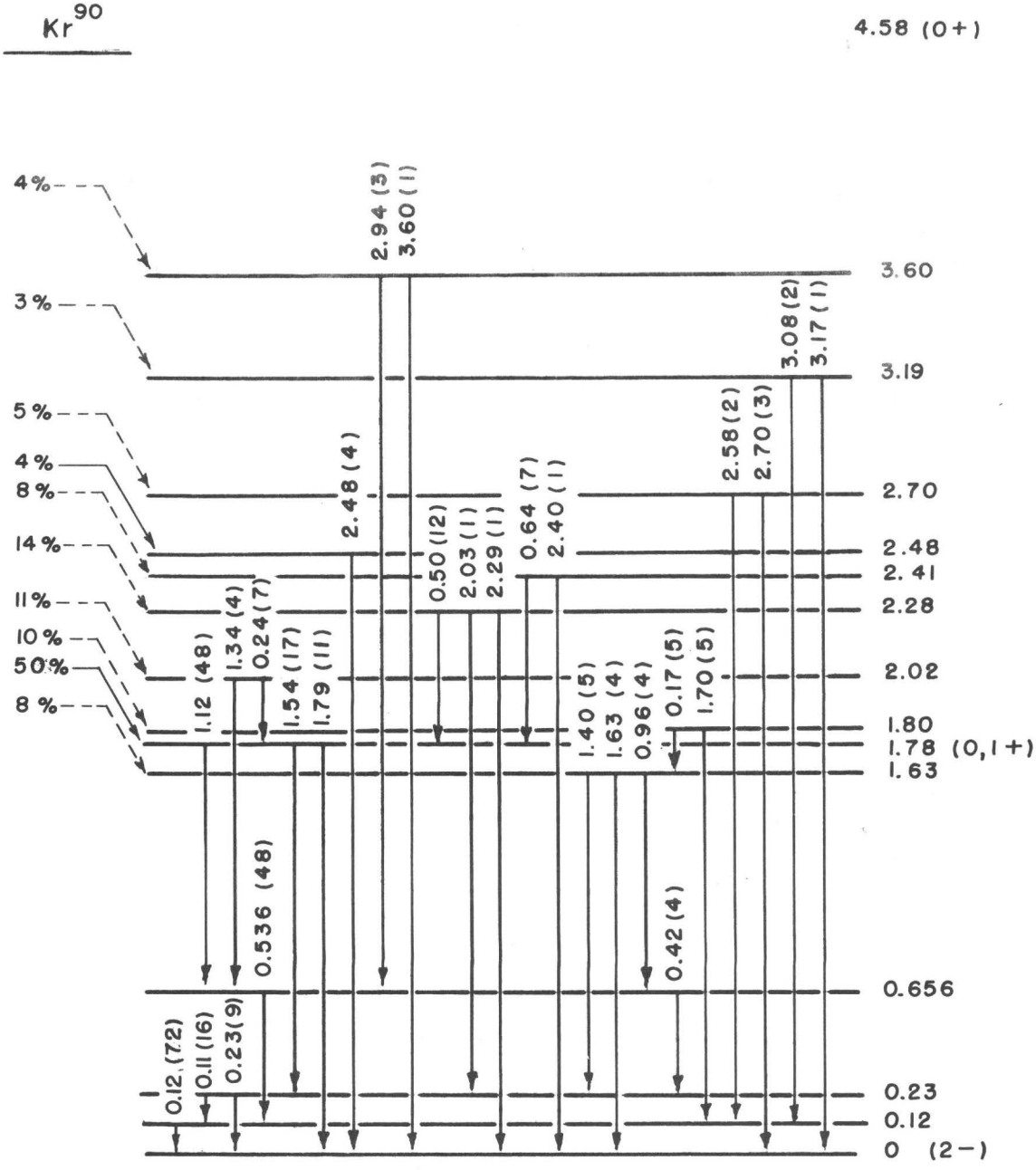

DECAY SCHEME OF Kr^{90} AS PROPOSED BY R.H. GOODMAN ET AL

FIGURE 5

of 4.5 ± 0.3 MeV. O'Kelley et al[60] made a detailed study of the decay properties of ^{89}Rb and established a half life of 14.9 ± 0.3 minutes for this isotope. These workers made use of a rabbit delivery system, a technique of aluminum absorption of the recoil xenon atoms to obtain pure krypton, and milking procedures to obtain ^{89}Rb samples. The ^{89}Rb was electrostatically collected and studied in detail with 3" x 3" NaI(Tℓ) detectors, a twenty channel analyser, an anthracene beta detector and a 4π counter. Figure 6 presents the pertinent information concerning the decay scheme of ^{89}Rb as found by these workers. Later O'Kelly et al[61] proposed the decay scheme of ^{90}Rb shown in Figure 7 using gas chromatography and the techniques of beta and gamma ray spectroscopy.

(e) Reaction Work on ^{89}Sr

Cohen[62] reported results of d-p reaction work on ^{89}Sr(d,p)^{89}Sr as part of a larger programme devoted to the determination of single particle states in the mass 90 region. Preston , Martin and Sampson[63] performed a similar work with essential agreement with Cohen's results. Sass , Rosner and Schneid[64] repeated these experiments and redetermined the values of some of the spectroscopic factors. The results of d-p reactions are shown in Figure 8.

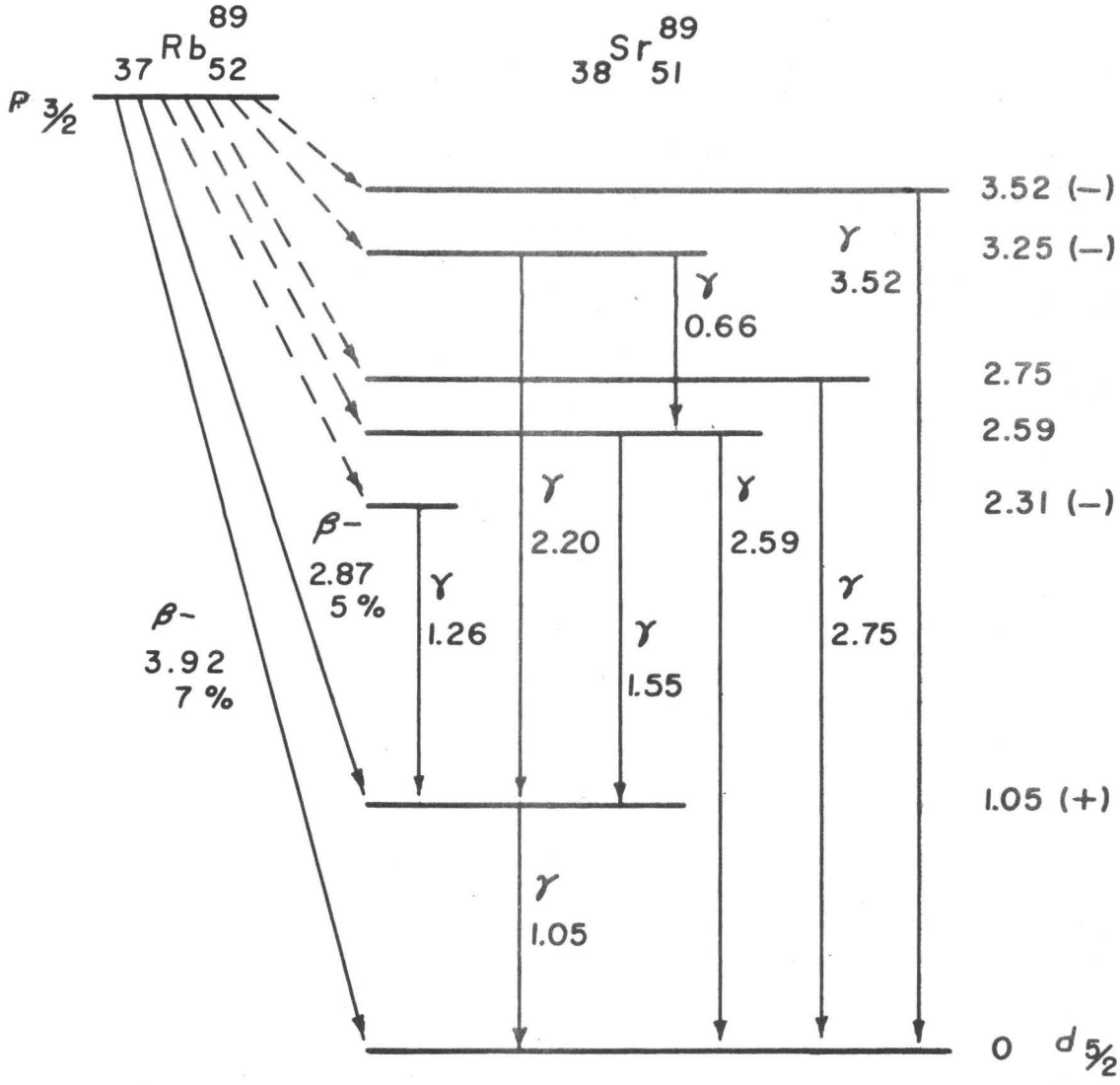

DECAY SCHEME OF Rb^{89} AS PROPOSED BY O'KELLEY ET AL

FIGURE 6

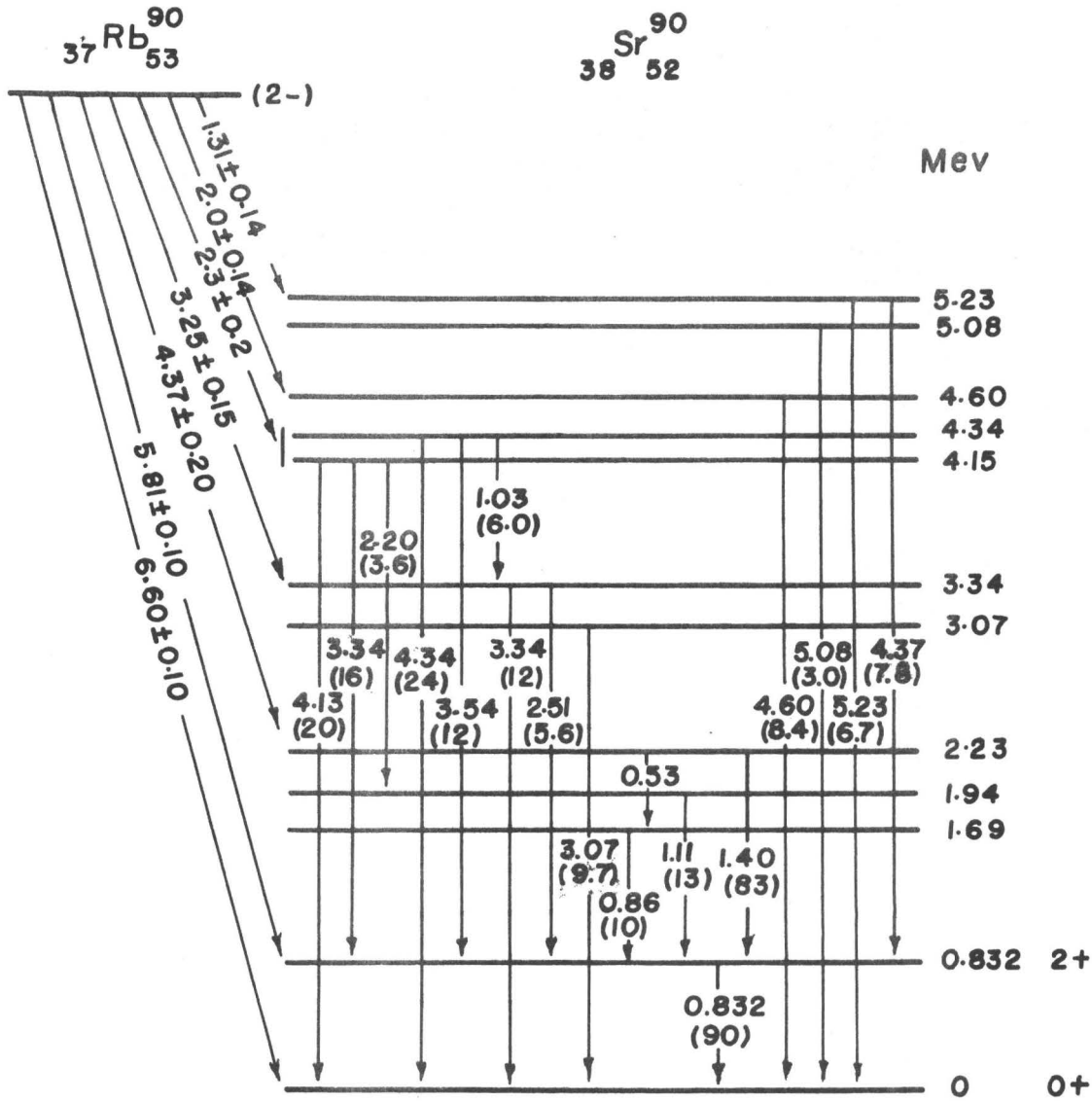

DECAY OF Rb^{90} AS PROPOSED BY JOHNSON ET AL

FIGURE 7

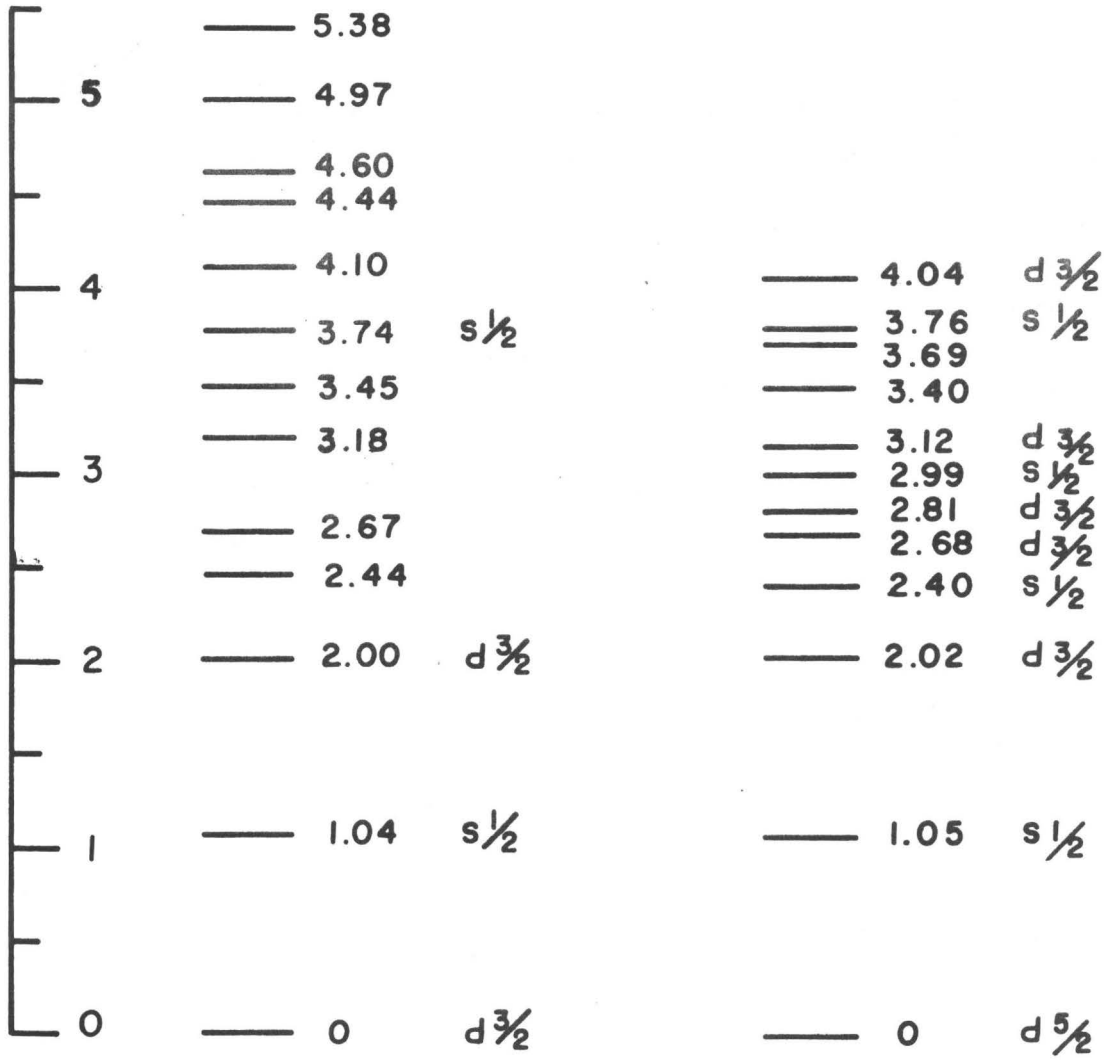

LEVELS IN Sr^{89} FROM (d,p) REACTIONS

FIGURE 8

CHAPTER III

SOURCE PREPARATION

(a) Apparatus

Sources of 3.2 minute ^{89}Kr were produced by means of a gas sweeping apparatus described by Ockenden and Tomlinson[54]. This apparatus, shown in Figure 9, consists of a fission chamber mounted on one end of a twelve foot tube which is inserted into one of the reactor beam tubes. The chamber is provided with a gas inlet and outlet, permitting helium carrier to sweep the chamber picking up rare gas fission products which are then swept to chromatographic apparatus external to the beam tube. The fission chamber was loaded with 0.5 gm of ^{233}U deposited on hydrous zirconium oxide by a technique due to Fiedler[65]. This material was chosen due to the high yield of ^{89}Kr relative to higher mass krypton isotopes produced in fission. See Table 3. Fission of the ^{233}U was induced by withdrawal of a cadmium sheath which shielded the fission chamber of the probe and thus exposed the ^{233}U to a flux of about 4×10^{10} $n/cm^2/sec$.

The chromatographic apparatus, shown schematically in Figure 10, consists of a pyrex U-tube packed with glass wool (6 mm. o.d. x 15 cm. length) and held at liquid nitrogen temperatures. The chromatographic column retained the xenon fraction[66] while passing the krypton fraction plus helium carrier. The flow path of the gases was controlled by a set of solenoid valves in a manner shown in Figure 10.

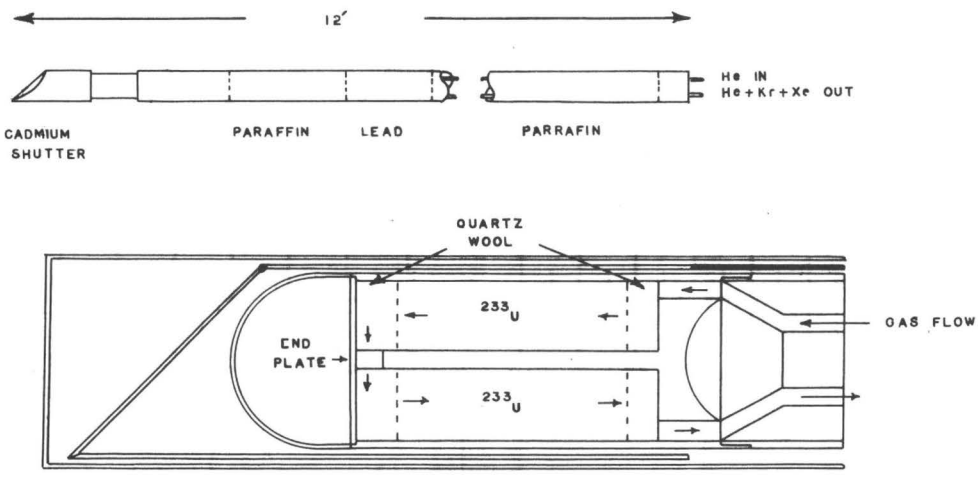

FIGURE 9 FISSION CHAMBER

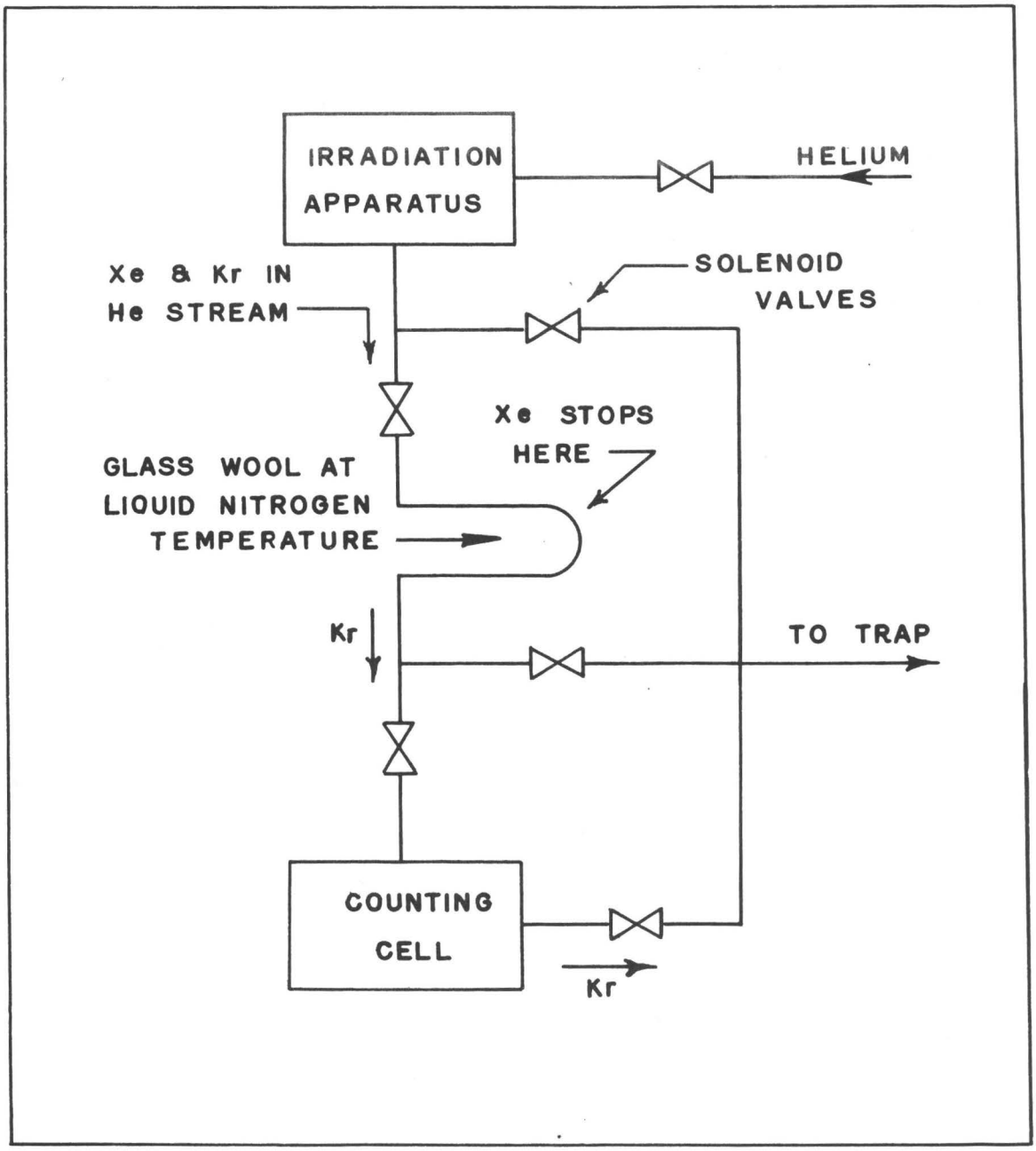

FIGURE 10 CHROMATOGRAPIC APPARATUS

Various combinations of valves could be simultaneously rendered operative by means of electrical relays to perform the function desired. Because the emanating chamber had a volume of about 30 cc., it was necessary to concentrate the krypton gas on a few milligrams of cold activated charcoal deposited in U-tubes in order to obtain "point sources" for measurement.

Following irradiation the tube containing the fission chamber was withdrawn $\approx 2'$ from its normal position, in addition to the cadmium shutter being closed. This was done to permit a cooling period which would be undisturbed by fission events induced by stray neutrons. Following the cooling period the samples were driven into the collection chamber through the chromatograph column in ≈ 7 seconds. No trace of xenon activity was observed in any of the krypton samples prepared in this way indicating that this activity is less than the experimentally detectible limit of $\approx 0.01\%$.

(b) ^{89}Kr Sample Preparation

The length of the irradiation and cooling periods determine which krypton isotope is maximized in the final sample. Normally an irradiation period of 4 seconds followed by a 4 minute cooling period produced krypton samples with a relatively high concentration of ^{89}Kr. The 4 minute cooling period effectively removes all of the 10 second ^{91}Kr and the 33 second ^{90}Kr activities. The resulting ^{89}Kr was found to be contaminated with about 11% ^{88}Kr(2.8 hours) and ^{87}Kr (75 min).[7] These contaminants have a lower Q value than ^{89}Kr, simpler gamma spectra, and much greater half lives and are thus easily identifiable.

Since ^{89}Kr (3.2 minutes) decays rapidly to ^{89}Rb (15 minutes) it becomes a major contaminant in a decay scheme study of ^{89}Kr unless it is continuously removed. For gamma ray experiments the sample chamber shown in Figure 11 was found to be effective for this purpose. It consists of an inverted test tube sealed at both ends and provided with inlets and outlets for both gas and water. Water is pumped continuously into the central water inlet to form a small diameter jet which strikes the smooth top of the test tube and then forms a thin water film over its entire inner surface. The hydrostatic pressure in the chamber is such that approximately 2 cc of water are collected at the bottom of the tube thus effectively covering the water and gas inlets and outlets. With a water flow rate of $\sim$ 1800 cc/hr, the water spends no more than 4 seconds in the chamber. Krypton gas samples, after being collected on activated charcoal, are driven into the chamber by the action of the helium gas stream and isolated there by solenoid and toggle valves. The efficiency of removing rubidium is simply related to the ratio of the area of the chamber covered with water to the total area and is greater than 99%. This efficiency is confirmed by the observation that no rubidium could be observed in the chamber above background. This chamber was used for all γ-γ and γ-singles spectra recorded with NaI(Tl) detectors.

Samples for use with Ge(Li) detectors were prepared by collecting the gas on activated charcoal contained in small U-tubes. These detectors possess high resolving power and therefore the strong ^{89}Rb gamma rays served as convenient internal standards.

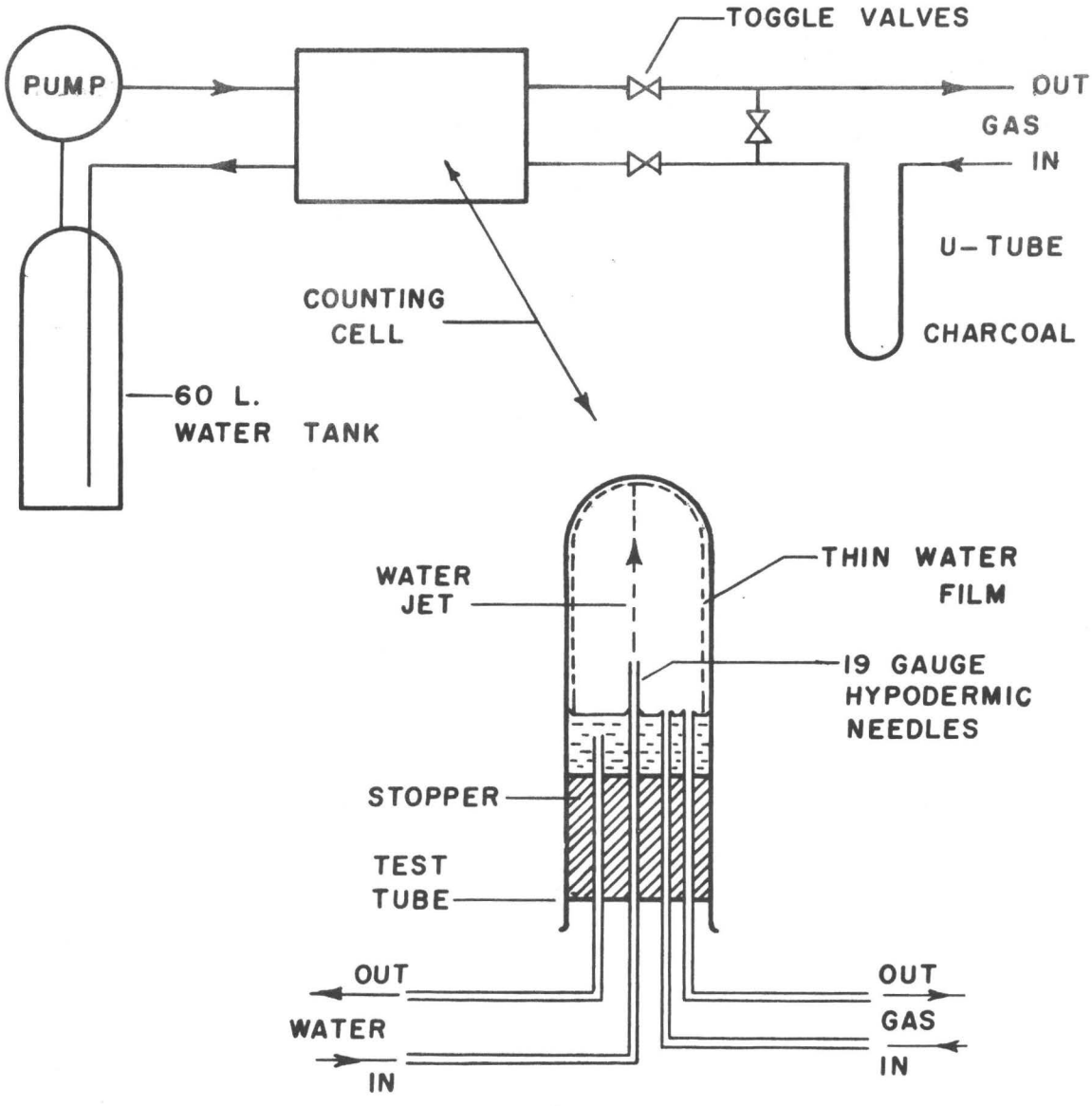

FIGURE 11 — GAS COUNTING CELL

^{89}Kr beta ray spectra, on the other hand, suffer severe distortion due to ^{89}Rb contamination. In order to remove the ^{89}Rb from the samples a small diameter hole (1.5 cm) was cut into one of the walls of the chamber shown in Figure 11 and covered with "saran"wrap windows ($\approx$ 1.5 mg/cm^2). By fabricating a small internal "lip" around the hole no water film could reach the window. This results in a small amount of ^{89}Rb build up on the windows, therefore a new chamber was necessary for each sample of ^{89}Kr activity. The efficiency of this device is approximately 80% . By viewing only the window region of the chamber reasonably pure and undistorted beta ray spectra could be obtained.

The ^{89}Kr β-γ and β singles experiments described in this work were actually done using sources prepared with the moving charged wire chamber used by N. Archer of this laboratory for his studies on xenon isotopes. This was done simply as a matter of convenience, since the chamber was available and located close to a large multidimensional analyser (64 x 64 channels). Dr. Archer's device[66] consisted of a negatively charged moving wire (speed 4 to 13 ft per min) pulled through a positively charged chamber (2" long by 0.5" diameter) whose wall was made of gold plated 0.25 mil mylar. The wall thickness of this device was 0.91 mg/cm^2.

Krypton samples were collected on activated charcoal contained in small pyrex U-tubes which were sealed with rubber serum stoppers. After warming, the U tube was coupled by a hypodermic needle to the inlet of the charged wire chamber and the gas pushed into the chamber by use of a syringe filled with helium.

(c) ^{89}Rb Sample Preparation

^{89}Rb is prepared by milking the ^{89}Kr parent. Samples of ^{89}Kr were collected on activated charcoal in pyrex U-tubes in the usual manner and allowed to decay for a period of 4 to 5 minutes. At the end of this time the sample holders were heated and purged of krypton activity by a helium gas stream. The ^{89}Rb samples prepared in this way contained $\approx$ 1% ^{90}Rb and ^{88}Rb and were used for NaI(Tℓ) and Ge(Li) detector work.

The sources of ^{89}Rb activity used in the beta ray spectrum work were prepared by electrostatic collection on 4 mm diameter aluminum foils ($\sim$5 mg/cm^2). The ^{89}Kr parent was first collected on activated charcoal in a copper U-tube which was connected via a set of stopcocks to an evacuated electrostatic collection chamber. The U-tube was then heated allowing the krypton activity to evolve from the charcoal then connected to the chamber. There the ^{89}Rb daughter was collected on the aluminum foils for a period of 4 to 5 minutes by the action of a 45 volt potential. At the end of the collection period the chamber was purged with helium and the foil mounted on the source holders which were then delivered by a pneumatic delivery system to the beta ray spectrometer laboratory. This mode of source preparation was also used in some of the Ge(Li) detector work; the spectra were indistinguishable from those prepared in the pyrex U-tubes described above.

CHAPTER IV

INSTRUMENTATION AND TECHNIQUE

a Detection of Radiation

The disintegration of radioactive nuclei leads to information concerning decay schemes through a study of the resulting alpha, beta and gamma ray emissions. These emissions are not directly observable and their presence must be determined by intermediate devices (detectors) placed between the event and the human observer. Detectors in general may serve two functions; in the first place they may determine if an event has occurred and in the second place they may yield information concerning the energy or momentum associated with the event. Detectors or detection systems which carry out both functions independently are in general high precision devices. A beta ray spectrometer makes use of a magnetic field to select a momentum interval and an independent scintillation spectrometer to detect an event occurring in this momentum interval. Detection systems combining both functions in a single device have normally had limited precision. The NaI(Tℓ) detector belongs to this class of instrument since both the energy of the incident radiation and its presence are determined simultaneously. On the other hand the recently developed lithium drifted germanium detectors which also measure the energy and detect simultaneously are a high precision device.

The detection of radiation is made possible by the processes

of ionization and scintillation. These processes are directly dependant on three main phenomenon which occur when radiation interacts with matter. This interaction occurs with atomic electrons through the mechanisms of the photoelectric effect, the Compton effect and the pair production[9]

The photoelectric effect is a process in which the total kinetic energy of the incident radiation is given to a bound atomic electron. The kinetic energy given to an electron ejected from the i^{th} shell by radiation of energy $h\nu$ is given by $h\nu - B_i$ where B_i is the binding energy of the i^{th} electron in the atom. For photons of energy well above the K shell binding energy about 80% of the photoelectric events occur in the K shell with the remaining 20% in the other shells. The excited atom whose electron was ejected deexcites by Auger electron emission or fluorescent x-ray emission which are competing processes. The photoelectric cross section varies roughly as Z^5 where Z is the atomic number of the interacting medium and as $E^{-7/2}$ where E is the energy of the incident radiation.

The Compton effect is a scattering phenomenon in which the energy of the scattered radiation $h\nu'$, scattered at an angle ϕ by a free electron is given by $h\nu' = h\nu \Big/ \left[1 + \frac{h\nu}{m_o c^2}(1 - \cos\phi)\right]$. For gamma ray energies well above the K shell binding energy, most of the electrons in the atom may be considered as free. The cross section for the entire atom is, therefore, Z times that of one electron. The differential cross section for a free electron is given by the Klein Nishina[67] formulae .

For incident photon energies above $2 m_o c^2$ pair production com-

petes with the Compton and photoelectric processes described above. In this process a positron-electron pair is created in the field of the nucleus. The cross section per atom for this process increases roughly as Z^2 and rises rapidly with $(h\nu-2m_oc^2)$.

The three processes described above are in competition at high photon energies. For low Z materials the photoelectric cross section is most important for energies less than 0.1 MeV, the Compton effect is dominant in the range of 0.1 to 1 MeV and pair production becomes important for energies of several MeV. All three processes transfer energy to an electron (or electrons) which subsequently, in a medium of finite extent, lose energy by ionization. The positron produced in pair production first loses its energy in this manner and then annihilates by association with a negative electron to produce two quanta of energy 511 keV. In a sufficiently large detector, every photon will eventually give up all its energy to the detector by a series of multiple interactions. For small detectors, many photons will only be partially absorbed, with the scattered Compton or annihilation radiation escaping from the sensitive volume. If, in a significant fraction of the interactions, the photons reaching the detector are completely absorbed, the size of the pulse may be used to measure the incident photon energy.

Because of incomplete absorption of radiation and to other effects associated with the transfer of the absorbed energy into electrical pulses, the output of a detector, which results from a field of monoergic radiation, shows a characteristic statistical distribution of pulse heights known as the response function of the detector.

The response is also influenced by source to detector distance, by the material in the neighbourhood of the detector and by the electronic system used to amplify and sort the pulses. Figure 12 presents a typical response function for a 7.6 x 7.6 cm NaI(Tℓ) detector to incident gamma radiation of energy 1.78 MeV. This response function is characterized by a full energy peak and a Compton distribution. The full energy peak is chiefly due to multiple interactions in which all the scattered radiation is absorbed in the detector while the Compton distribution is due to events in which some scattered radiation escapes from the detector. Imposed on this distribution are the escape peaks resulting from annihilation photons leaving the detector. Small angle scattering in absorbing material placed between the source and detector produce an energy degradation of the primary radiation which fills in the valley between the photopeak and Compton distribution. Compton scattering processes in the surrounding material produce the "back-scatter" peak as well as other minor distortions of the response. Pair production in material outside the detector produces a 0.511 MeV peak whose intensity is a function of the geometry and of the intensity of the gamma radiation from the source of energy greater than 1.022 MeV. The low energy distribution is distorted by the presence of bremsstrahlung radiation originating from the stopping of beta particles in the beta source itself and in absorbers.

Fortunately, these distortions remain constant in any given geometry and therefore it is wise to carry out as many experiments as possible in the same geometry. Most of the NaI(Tℓ) experiments were performed in a standard geometry and response functions for monoergic

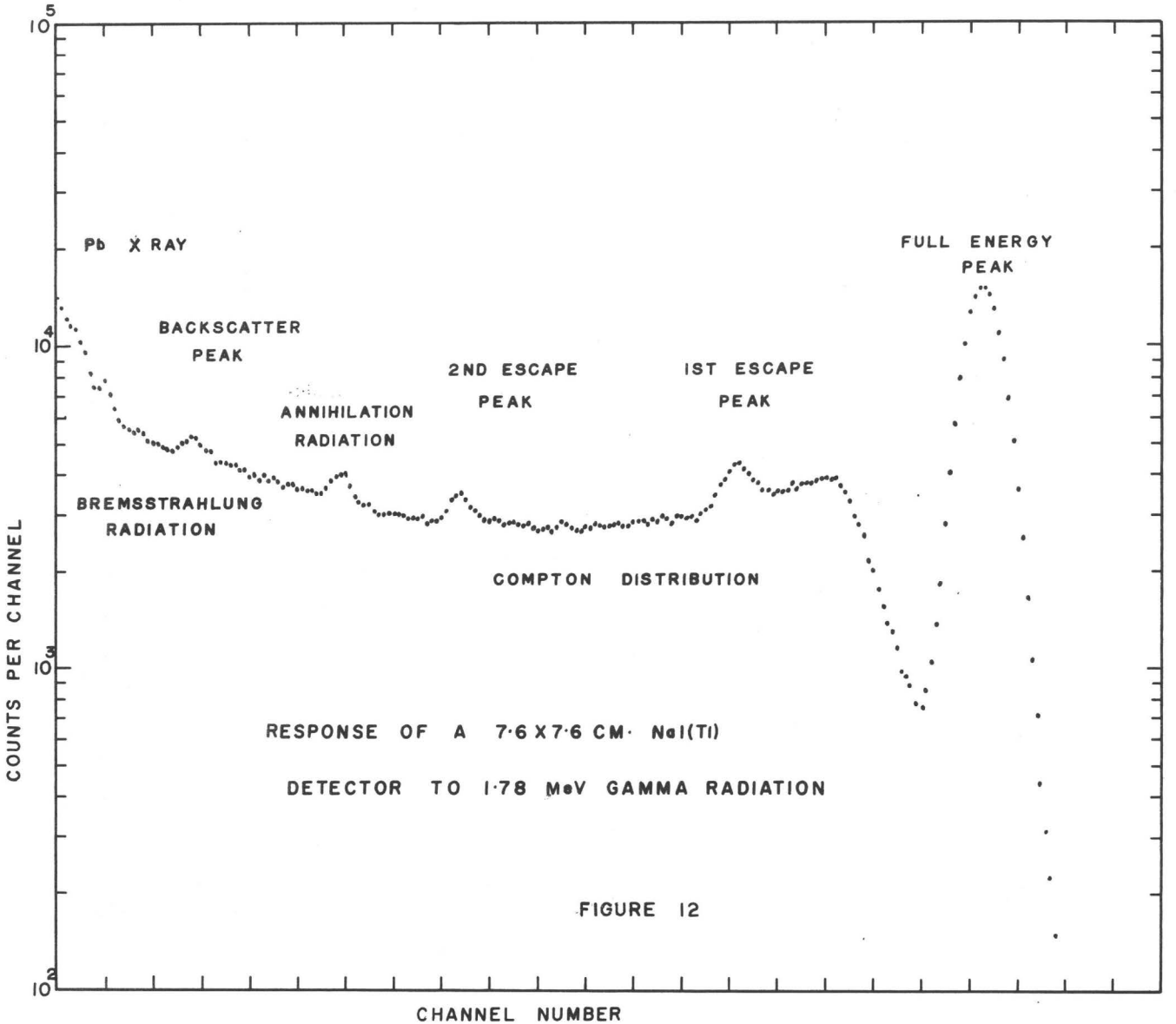
Pb X RAY
BACKSCATTER PEAK
ANNIHILATION RADIATION
2ND ESCAPE PEAK
IST ESCAPE PEAK
FULL ENERGY PEAK
BREMSSTRAHLUNG RADIATION
COMPTON DISTRIBUTION
RESPONSE OF A 7·6 X 7·6 CM· NaI(Tl)
DETECTOR TO 1·78 MeV GAMMA RADIATION
COUNTS PER CHANNEL
CHANNEL NUMBER
10^5
10^4
10^3
10^2

FIGURE 12

gamma rays carefully determined under these conditions.

Because of the short half lives of the nuclides studied, the γ-γ and γ singles experiments were carried out in the reactor building and were, therefore, subject to high background radiation. This was reduced by placing the detectors within a large "cave" of interior volume one cubic meter. This structure, fabricated from high density concrete blocks, was lined with 1/8" of lead to reduce the magnitude of the backscattered radiation . The interior volume housing the detector was continually flushed with air obtained from sources external to the reactor building to remove the ^{41}Ar contaminant always present around the reactor. Each detector was shielded against beta radiation by means of lucite disks (2.54 cm thick) covering the front faces of the detectors and lucite cylinders (0.3 cm thick) enclosing their sides.

The NaI(Tℓ) detector operates on the scintillation principle. The absorption of photon or particle energy leaves the atoms of the scintillator in excited states which subsequently decay by emitting light. A useful scintillator must be transparent to its own emitted radiation so that this light may be collected on the photocathode of a photomultiplier. The photo electrons produced in this cathode are then accelerated to a set of dynodes which multiply the electron flow by secondary emission. By a suitable choice of dynode material one can obtain a gain of four per stage. Thus an n stage photomultiplier can be expected to have a gain of 4^n. Since the light output of the scintillator is very nearly proportional to the energy deposited, the output of the photomultiplier is closely proportional to the energy

of the incident radiations.

The chain of events described above is indicated below.

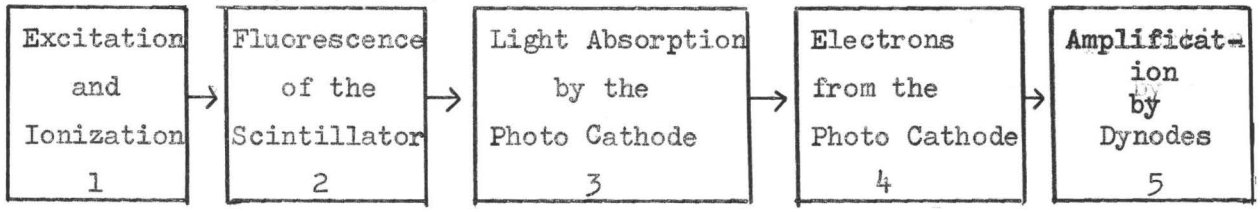

Each of these steps involves a probability factor[68] which eventually manifests itself in the finite resolution of the detector. Providing good light collection between 2 and 3 is ensured, this resolution or instrumental line width is determined mainly by step number 4 with a smaller contribution from the photomultiplier in stage 5. If all the energy in the light from the scintillator could be converted into an electrical pulse, NaI(Tℓ) crystals would have a resolution of a few keV. However, because of the inefficient conversion of light quanta to electrons in the photo cathode, a large statistical uncertainty in the number of ejected photo electrons results. Since the number of electrons ejected varies from one scintillation to the next a line broadening occurs which has a characteristic Gaussian distribution. In addition to the variance associated with this conversion process an additional contribution to the instrumental response results from the variance associated with the electron avalanche produced by a single photo electron in the photomultiplier tube[69]. Typically these effects result in a line width for a 0.662 MeV incident radiation of approximately 7.2% (47 keV) for the detectors used in this work.

In addition to the effects so far described NaI(Tℓ) detectors show a small nonlinearity between pulse output and energy input [69,70]

and corrections for this effect must be made if the detector is to be used for precise energy measurements.

Solid state detectors on the other hand show much narrower line widths (see Figure 13) because the conversion of energy to electrical pulses takes place by a more direct process. The small volume of these detectors makes multiple scattering in the detector improbable with the result that the full energy peak is chiefly due to the photo electric effect. These detectors make use of the ionization principle to convert radiation into electrical pulses. The energy required to produce an average ion pair is constant for a given material (~32 eV/ion pair for gases and 3 to 4 eV/ion pair for solids). This implies that if all the ion pairs could be collected a solid state detector would have a resolution of less than 2 keV for a 0.662 MeV radiation. By applying suitable voltages to the faces of the volume in which ionization has taken place the ion pairs may be swept out to form a current pulse. Since the energy required to produce an ion pair is constant, the total number of ions produced is proportional to the incident photon radiation energy.

In solid state detectors high sweeping fields are required in order to collect the ions before recombination occurs. Such fields are produced by fabricating the detector in the form of a diode which is then reverse biased to cause a high field gradient across the intrinsic compensated region in which ionization occurs. Such diodes are produced by drifting techniques[71] using lithium or phosphorous as donors in high resistivity germanium or silicon. Because of crystal imperfections and other effects, losses of ion pairs occur with a sub-

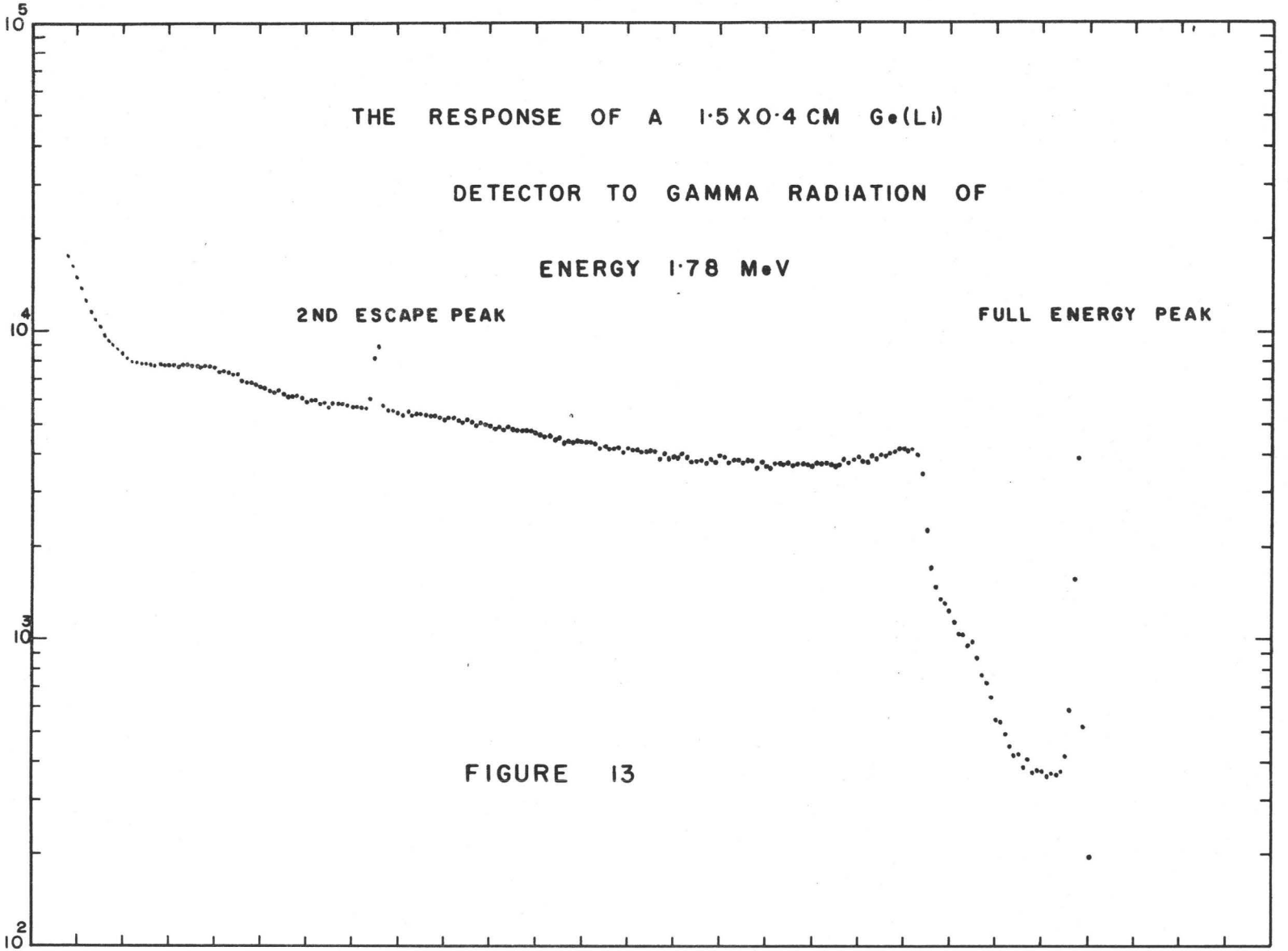
THE RESPONSE OF A 1·5 X 0·4 CM Ge(Li)
DETECTOR TO GAMMA RADIATION OF
ENERGY 1·78 MeV
2ND ESCAPE PEAK
FULL ENERGY PEAK
10^5
10^4
10^3
10^2

FIGURE 13

sequent line broadening. The best Ge(Li) detector used in this work had a line width of 2.3 keV at 0.662 MeV under favorable conditions. The detectors used in the earlier experiments were much poorer - with a line width of 5-7 keV for the ^{137}Cs line.

Beta particles may be determined by either of the two methods outlined above. Silicon detectors, which operate on the ionization principle, have the high resolution characterized by such devices and are very popular for the study of internal conversion spectra. These detectors are not as useful for the study of beta ray continua because they have a rather complex response function and are not easily available in thicknesses sufficient to stop energetic beta rays. Plastic detectors, which operate on the scintillation principle, have characteristicly poor resolution but are very useful for the study of beta continua because they may be obtained in large sizes and because their response characteristics may be precisely determined. The response function of a plastic scintillator, such as NE102* is characterized by a Gaussian full energy peak plus a flat backscattered tail extending from the full energy peak to zero energy. Freedman et al(72) have shown that the ratio of the heights of the backscattered distribution to the full energy peak is a constant for the energy range $0.2 \leq E_o \leq 1.0$ MeV. Techniques used to correct the data for response effects will be discussed in the following chapter.

A magnetic beta ray spectrometer is a high precision device with good resolution. The Gerholm type spectrometer(73) shown in Figure 15

---

* Nuclear Enterprises, 544 Berry St., Winnipeg, Manitoba

was used in the present work. The electrons in this spectrometer are focussed by an axially symmetric magnetic field whose axial component rises linearly along the axis of the instrument from zero at the source to a maximum just in front of the detector. The electrons spiral about the lines of force, are brought to a ring focus a few cm in front of the detector, and are momentum selected by a ring baffle located at this focus. Detection of the electrons which pass through the ring baffle is carried out on a large (2.5 cm diameter) disc of plastic or anthracene scintillator coupled to a photo multiplier by a light pipe. The focussed momentum is determined by the magnetic field strength which in turn is determined by the current passing through the coils. The beta active material was spread uniformly over a disc of diameter 4 mm on an aluminum leaf backing and introduced into the instrument by means of an air lock. With such sources, the baffle system could be adjusted to yield a resolution of 2.7% in momentum and a transmission of about 2%.

b Energy Measurement from Pulse Analysis

The pulses produced by scintillation or ionization detectors require amplification of the order of 10^3 to 10^4 before they can be subjected to pulse analysis. It is usual to obtain part of this amplification in a preamplifier located close to the detector and the remainder in a post amplifier placed near the analysing equipment.

The preamplifier, whether of the charge or voltage sensitive type, amplifies the detector pulses by a factor of ≈ 10 and feeds them to the amplifier through a low impedence line. This allows the detector to be separated from the amplifying system by a considerable

distance without introducing undue disturbances from noise or signal losses. For a scintillation counter the fluorescent decay time determines the pulse rise time whereas the capacity of the preamplifier circuit determines the pulse decay time. The preamplifier capacity was chosen to give a very large decay constant. This insured efficient charge collection and produced pulses which appeared as steps on the slowly decaying portion of the preceding pulse. Such step-function pulses are suitable for determining relative pulse heights.

In the main amplifier the pulses were clipped to a length of 0.7 μs and double differentiated by means of delay lines. This alters a step pulse to a square pulse whose height above the base line is independent of pulse repetition rate. These shaped pulses were then linearly amplified to a maximum of $\pm$ 10 volts. It is found experimentally that the zero crossover point of a double differentiated pulse is independent of the pulse amplitude to within $\approx$ 20 ns. This crossover point thus becomes a convenient reference point for time correlations between pulses.

In order to obtain energy measurements from the detector the shaped pulses from the amplifier must be sorted according to height. This sorting was carried out in the present work by a Nuclear Data Model 121,512 channel analyser. This device sorts a 10 volt range of pulse amplitude into 512 equal steps or bins. This sorting procedure is carried out by allowing the pulse to charge a condensor and then measuring the time (by means of a high frequency clock) required for the condensor to discharge to a predetermined voltage level through a constant current leak. The time of decay is thus a digital representation of the pulse amplitude and the device carrying out the trans-

formation from a pulse basis to a digital basis is called the analogue-to-digital converter. (A.D.C.) The bin corresponding to this digit is then activated to register a count.

c Time Correlations from Pulse Analysis

It is often very useful to establish if two nuclear radiations are emitted in sequence (i.e. are time correlated) in the decay of a given nucleus. Since the time required for the completion of such a sequence is in general much shorter than the smallest times that can be measured electronically, a time-correlated pair of events will appear to be in coincidence. A study of the coincidence relationships present among the radiations emitted from a given nuclide can yield important information concerning the sequences present in the decay process.

A typical coincidence circuit arrangement, used for gamma-gamma coincidence experiments, is shown in Figure 14. Two detectors "view" the same radiation source and produce pulses which are amplified and shaped by the preamplifiers (P.A.) and double delay line amplifiers (D.D.2). The cathode followers (C.F) isolate the amplifiers from the logic circuits. The fast-slow units generate timing markers when the double differentiated pulses pass through the crossover points. The wires carrying these marker pulses (or fast pulses) are shown in the figure by dotted lines. Marker pulses from the fast slow units associated with the two detectors are fed to coincidence units which generate routing or gating pulses whenever two fast pulses arrive within a time 2τ, known as the resolving time of the circuit (about 70 ns in these experiments). The production of such a routing

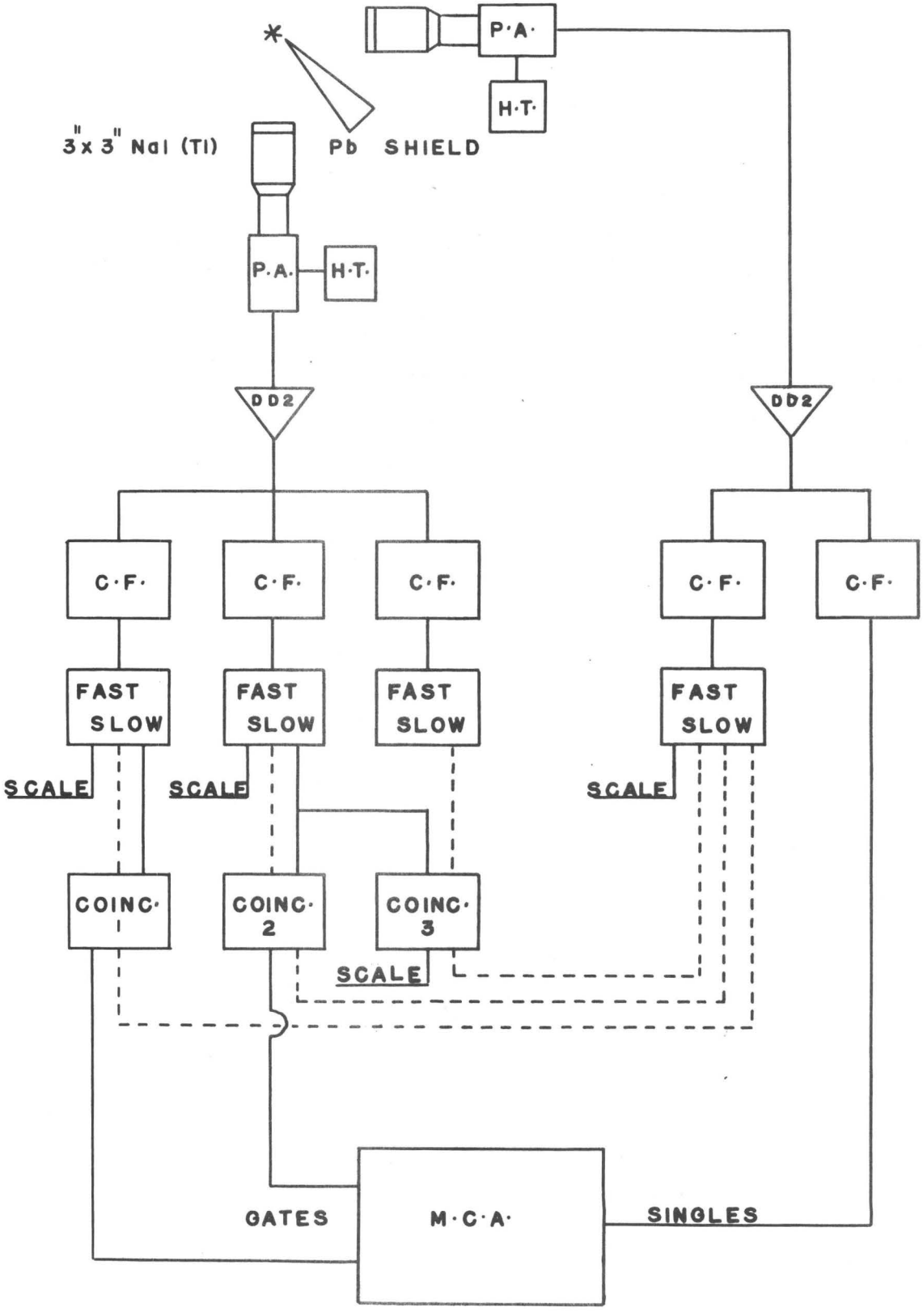

FIGURE 14 GAMMA GAMMA COINCIDENCE CIRCUIT

pulse thus indicates a coincidence pair of events. The value of 2τ can be varied by broadening the marker pulses and the time of production of these pulses may be delayed up to $3\mu s$.

The fast slow units also may act as single channel analysers which generate pulses whenever the input pulse height falls between V and V + ΔV, where both V and ΔV are independently variable. These pulses ("slow pulses") are carried along the solid lines in the figure to the coincidence circuits or to scalars. The inclusion of a slow channel in the coincidence circuit imposes the condition that routing pulses from the coincidence unit are produced only if a fast pulse from one detector and both fast and slow pulses from the other detector are in coincidence. Such a routing pulse then indicates a coincidence between a pulse of height V to V + ΔV from one detector (the gating detector) and a pulse of any height from the other (analysing detector).

In the figure, the lower crystal is the gating detector and the one on the right is the analysing detector. Pulses from the latter are fed directly to the multi channel analyser via the amplifying system. These can only enter the analyser if a routing pulse from the coincidence unit opens a gate in this device. Thus the analyser records the gamma ray spectrum of the analysing crystal in coincidence with the portion of spectrum of the gating detector which is passed by the single channel analyser of the fast-slow unit. In practice, the 512 channel analyser was used as two 256 channel instruments with gating pulses derived from two separate fast-slow discriminators set on different portions of the spectrum. The third fast-slow discriminator and coincidence circuit 3 shown in the figure were used to measure

chance events in the manner to be described later.

Beta-gamma coincidence measurements were carried out using the apparatus and circuitry schematically outlined in Figure 15. These measurements were designed to determine the gamma radiation in coincidence with the monoergic beta rays focussed by the magnetic beta ray spectrometer. In these experiments a 7.6 x 7.6 cm NaI(Tℓ) detector was inserted into one end of the Gerholm type beta ray spectrometer and was shielded from stray magnetic fields by a Mu-metal shield and a soft iron cylinder. Shielding from scattered gamma radiation was obtained by use of a lead cone placed between the detector and source.

The coincidence circuit used was very similar to that used in the γ-γ coincidence experiments. However, it made use of fast pulses only, with the coincidence gamma ray spectrum being accumulated in the multi channel analyser. From a set of such coincidence spectra, accumulated for different momentum settings of the beta ray spectrometer, the beta ray spectrum in coincidence with each particular gamma ray emitted by the nuclide was established. These data were used to form Fermi plots from which the end points and intensities of these partial beta spectra were determined. Because the nuclide under study had a short half life, it was impossible to obtain the complete series of gamma spectra with one source. Multiple sources of the same physical size were used and normalization was obtained by recording a portion of the gamma ray singles spectrum continuously throughout each run. The use of this normalization procedure made it unnecessary to measure source strengths or to record counting times, the number of counts accumulated providing all the information required.

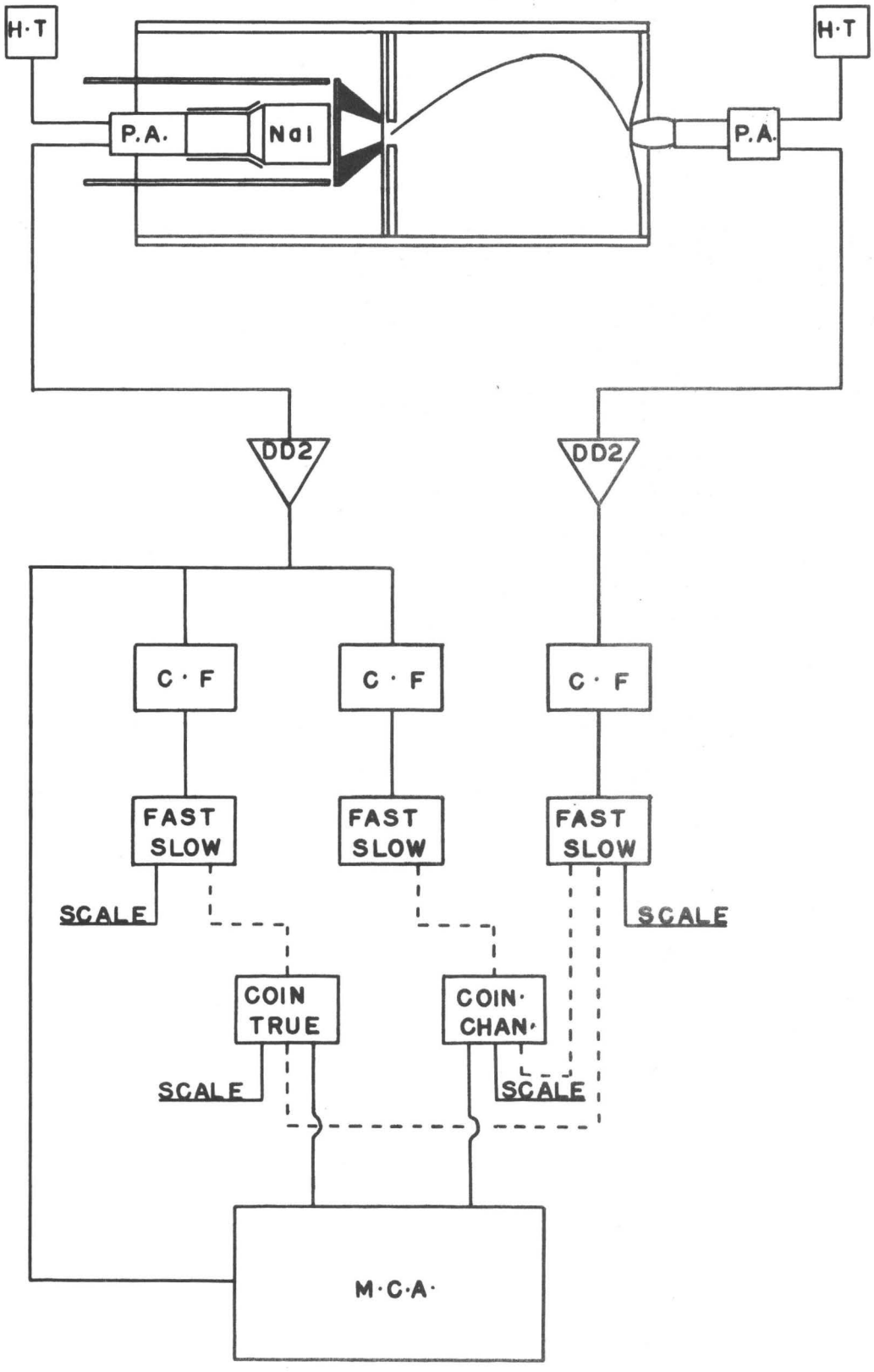

FIGURE 15 BETA — GAMMA COINCIDENCE CIRCUIT

For some of the experiments with short lived nuclides, which could not be carried out with the magnetic spectrometer, a plastic beta detector (5 cm by 5 cm) was used for both beta singles and beta-gamma coincidence measurements. In this case a two dimensional analyser was used with both coincidence beta and gamma rays being stored in a 64 x 64 channel grid. The coincidence circuitry employed is identical to that used for the gamma-gamma coincidence work, with the exception that only fast pulses were used. For these experiments a rather complex correction for the beta detector response function was necessary before the data could be rendered meaningful.

d Angular Correlations from Pulse and Spatial Analysis

It has already been shown in Chapter I that the angular correlation pattern for cascading gamma rays may give useful information about nuclear spins. This investigation was carried out with the apparatus schematically outlined in Figure 16. Three identical 7.6 x 7.6 cm NaI(Tℓ) detectors plus standard coincidence circuitry were used. The monitoring and gating detectors were held at 90° to each other while the third counter (the analysing detector) was movable. Coincidences between the gating and monitoring detectors, and between the gating and analysing detectors were recorded simultaneously. Since any window drifts in the gating detector will affect both coincidence rates in the same proportion, the ratio of the two recorded rates is independent of window drifts. These ratios were determined for 90°, 135° and 180° and the data accumulated in a multi channel analyser. Spectral distortions due to backscattering and chance contributions (section e) were eliminated before analysis of the data.

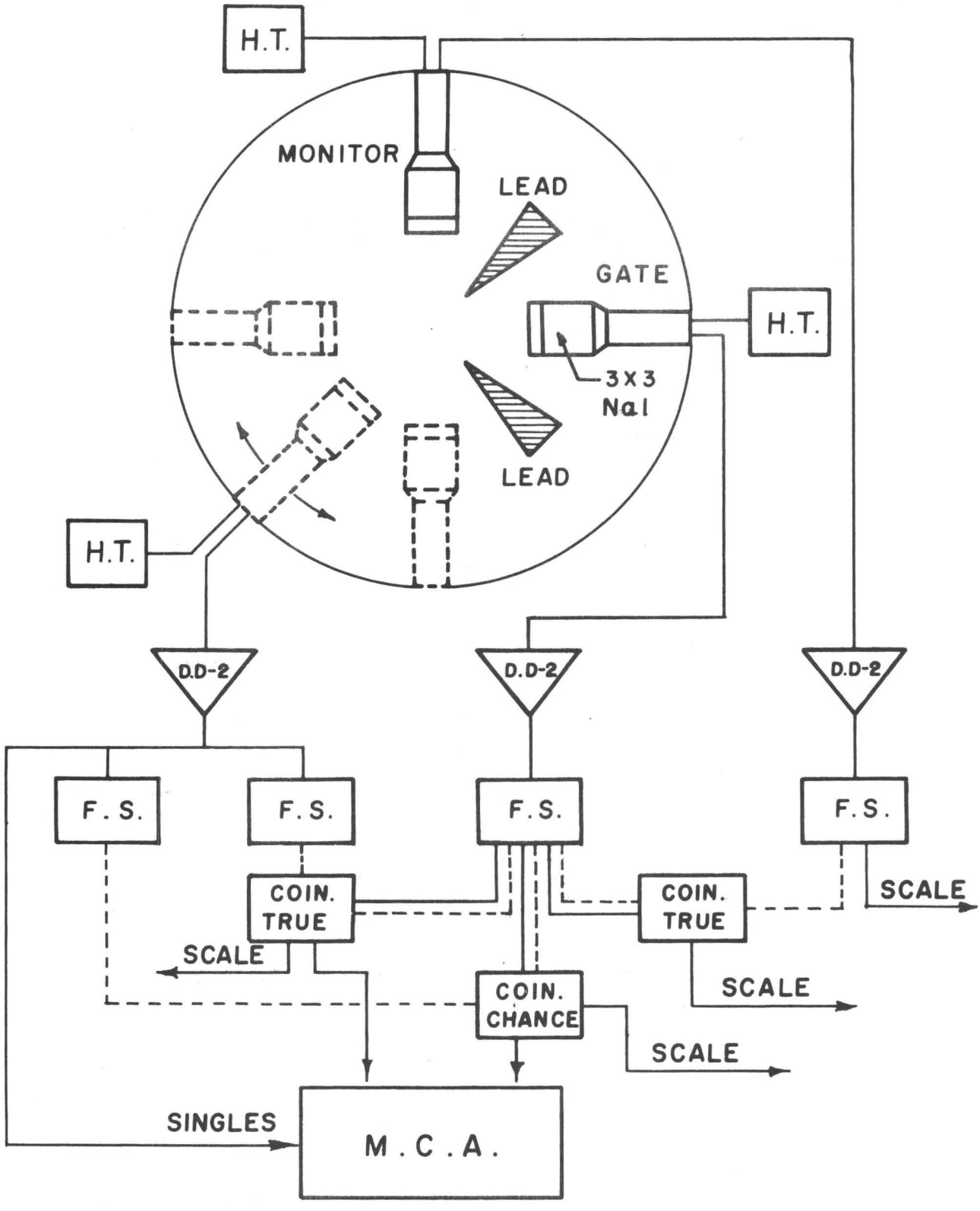

FIGURE 16 ANGULAR CORRELATION CIRCUIT

e Spectral Distortion in Pulse Analysis

Because of the random nature of nuclear decay processes and because a coincidence circuit registers as simultaneous any events occurring within a finite time interval 2τ, the recorded coincidences rate is partially due to events registered on an accidental basis. Since any event from detector one sensitizes the coincidence circuit for τ seconds, an event from detector two occurring within this time will be registered as a coincidence. Since the roles of detector one and two in this process are interchangeable, it is easily seen that the number of chance events recorded will be $2\tau N_1 N_2$ where N_1 and N_2 are the counting rates in the two detectors. The chance coincidence spectrum associated with any gate is identical in shape to the singles spectrum.

The gamma-gamma coincidence circuit presented in Figure 14 contains electronic provisions for determining the number of chance events occurring in the accumulated coincidence spectrum. This provision consists of a fast-slow discriminator plus coincidence circuit number 3. By delaying the slow pulses from the fast-slow unit for two microseconds before passing them to the coincidence unit, all time correlations between the events viewed by the detectors are destroyed. The inclusion of the same slow channel in conjunction with coincidence circuit number 2 imposes the condition that the recorded chance rate will be that of circuit number 2 provided all resolving times are identical. Furthermore, by scaling the number of events passing through the slow channel of circuits one and two and by determining the resolving times of all circuits involved, the chance spectrum may be

calculated for all recorded coincidence spectra from this one measurement. These provisions for determining chance rates were included in all coincidence circuitry (see Figure 15 and Figure 16).

The detection of accidentally coincident or time-correlated events occurring within the same detector leads to a distortion of both singles and coincidence spectra. If a detector is recording events which are time correlated then there exists a finite probability that two such events will fall on the detector simultaneously with the result that the pulse output is the sum of the pulse heights of each event separately. Such distortion is known as coincidence summing and leads to spurious peaks in the spectrum. In addition, since detection systems possess a characteristic time interval τ within which they are incapable of distinguishing two events as separate, any events falling on a detector and separated by a time less than τ are recorded as a single event. Such events may occur on a purely accidental basis. If y_1 and y_2 represent the pulse heights of the two events then the detector will sense the combined event as a pulse whose high ranges from the smaller of y_1 and y_2 to $y_1 + y_2$[74]. The time interval τ is determined by the clipping time of the amplifiers which were $\approx 0.7\ \mu s$ in the present work. The electronic circuit presented in Figure 17 shows a schematic arrangement of the apparatus used to record the coincidence and random sum events that distort a singles spectrum. Pulses from two identical NaI(Tℓ) detectors were balanced for gain and added. These added pulses as well as the singles pulses from each detector were fed to amplifying systems. The added pulses were fed directly to the multichannel analyser while the singles pulses were used to generate

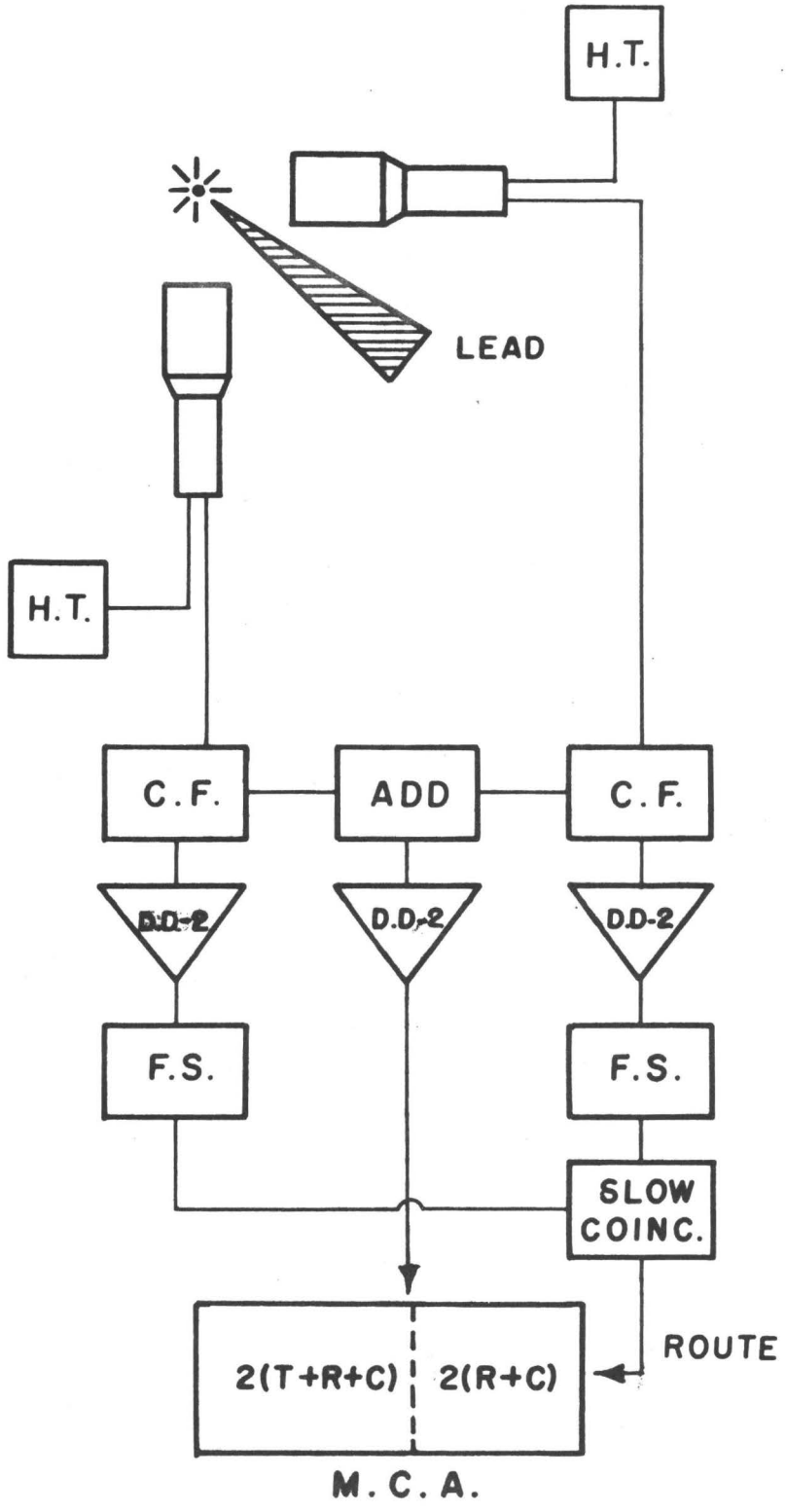

FIGURE 17 SUM CIRCUIT

timing markers. The coincidence circuit ($2\tau \approx 1.5\mu s$), then registered all coincidence events between the detectors. By means of the routing pulses those events which registered coincidences and which were added were routed to the second half of the analyser.

Since the pulses from two detectors were added the first half of the analyser contained twice the number of singles and twice the number of random and coincidence added pulses which had registered in each detector separately. The second half of the analyser contained the added pulses originating from both detectors; i.e. twice the random plus twice the coincidence added pulses.

Figure 18 presents a spectrum of radiations from the nuclide ^{24}Na in which the primary distortion is due to coincidence summing. The ability of the apparatus to register sum events is clearly shown.

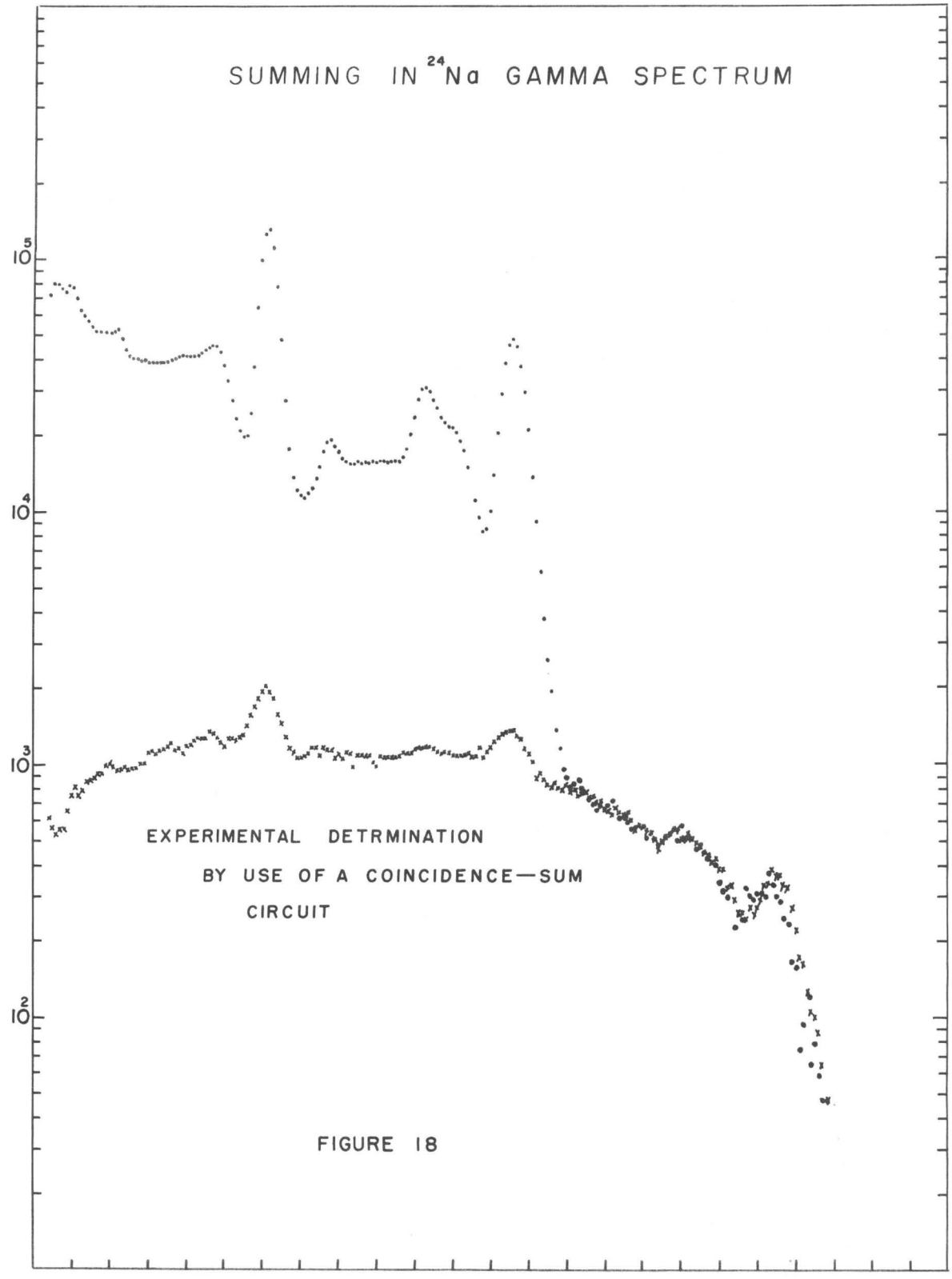
SUMMING IN ^{24}Na GAMMA SPECTRUM
10^5
10^4
10^3
10^2
EXPERIMENTAL DETRMINATION
BY USE OF A COINCIDENCE—SUM
CIRCUIT

FIGURE 18

CHAPTER V

DATA REDUCTION

a The Relationship Between the Observed and the True Spectrum

Data analysis is the reduction of experimentally obtained information to meaningful numbers. The spectrum observed by a detection system is the result of combining the response function of the detector with the true spectrum (whether a series of monoergic photon or particle groups, or a continuum). The first step in the reduction process is the correction of raw data for detector response in order to obtain the true spectrum. This spectrum may then be dealt with in an appropriate manner. This "unfolding" of the response functions is described below.

An observed spectrum, $\underline{M}$, is related to the "true" spectrum, $\underline{N}$, by the expression

$$\underline{M} = \underline{R}\,\underline{N} + \underline{V}$$

Where $\underline{R}$ is the response matrix corresponding to the detector response functions and $\underline{V}$ is the variance vector associated with the statistical nature of radioactive decay. If $\underline{V}$ were not present in the measured spectrum one could pass from this spectrum to the "true" spectrum exactly since

$$\underline{N} = \underline{R}^{-1}\underline{M} \qquad \text{provided } \underline{R}^{-1} \text{ exists.}$$

Due to the presence of $\underline{V}$ one must settle for the most probable value of $\underline{N}$. If $\underline{W}$ represents the weight matrix then the expression

$$\underline{N} = (\underline{R}^{T}\underline{W}\underline{R})^{-1}(\underline{R}^{T}\underline{W}\underline{M})$$

is the best estimate (unbiased) of the true spectrum N. This method of estimation is based on the method of least squares.

Every detection system possesses a response characteristic of the system, which must be known before interpretation of the data is possible. In many cases it is not necessary to perform the computation outlined above since the type of information desired may not require such a detailed procedure.

b NaI(Tℓ) Spectra - Analysis by "Hand Stripping"

Because of their high efficiency, NAI(Tℓ) detectors are normally employed in γ-γ and β-γ coincidence work even though their poor resolution limits the quality of the information that can be obtained. One may attempt to resolve a complex spectrum into its component responses by "hand stripping". In this process, one removes the contribution of the highest energy gamma ray in the spectrum by fitting its known response function to the spectrum both in gain and intensity. Upon subtraction of this component, a residual spectrum is obtained which is the measured spectrum less one component gamma ray. The stripping procedure can now be applied to this residual spectrum to remove the next highest energy gamma ray and so on until the entire spectrum has been resolved into its components. Although this method is capable of extracting reasonably reliable data for the stronger components, the fact that the errors are cumulative makes it difficult to trust the analysis for weaker components. Moreover the process is very laborious and time consuming and much better performed by an electronic computer. With the aid of such a computer, it becomes possible to carry out a simultaneous least squares fit, both in gain and intensity, for all the response functions comprising the

spectrum with the elimination of the cumulative errors associated with the "hand stripping" process.

c NaI(Tℓ) Spectra - Analysis by Use of a Computer

The use of a computer to analyze the response of a NaI(Tℓ) detector to a complex spectrum of gamma rays has been studied by many workers and a large number of programs of varying degrees of sophistication have been described in the literature[75].

The advent of lithium-drifted solid state detectors has made the problem of spectral analysis much simpler, since it is now possible to make high resolution studies of the gamma rays from radioactive nuclei, without the laborious point-by-point examination required by external conversion measurements with a magnetic spectrometer. Thus one can readily determine the photon energies present in the spectrum with a high resolution device before one uses the NaI(Tℓ) detector with its higher efficiency to carry out the coincidence experiments necessary to establish the decay scheme. The problem thus reduces to developing the appropriate intensities to yield the composite spectrum under study. Finally, small adjustments in the positions of the components may be made to adjust for non-linearities and energy calibration errors. It should be noted that, once the response functions for the various photons present in a spectrum are known, these same response functions will be applicable to the analysis of all the β-γ or γ-γ spectra recorded with the detector in the same geometry.

The problem breaks into two parts: (1) the generation of the response function for each of the gamma rays present in the spectrum; and (2) the fitting of these in intensity, together with slight adjustments

in energy, to minimize the chi-squared parameter. The method employed for generating the response functions is essentially that of Heath[76] but it will be described below for completeness. The fitting procedure involves a non-linear application of the least squares method which automatically adjusts the line positions and intensities to minimize the following parameter* in the sense of least squares, i.e.

$$\chi^2 = \sum_{x=1}^{N} W(x)\left\{Y(x) - B(x)\right\}^2 \qquad (1)$$

where Y(x) is the measured response of the detector to the spectrum

B(x) is the model function generated from the known responses of lines in the spectrum

W(x) is a weighting function

N is the number of data points.

d Generation of the Response Surface

The response surface represents a function relating the incident photon energy to the detector response. Specifically it is a surface in a three dimensional space in which the dimensions are count rate, channel number and incident photon energy. This surface is obtained by least squares fitting to a finite number of response functions (line shapes) determined experimentally for a series of monoergic photon energies over the range of interest. When this response surface has once been defined in analytic form, the response function for any other photon energy can be obtained by interpolation.

A flow diagram describing the process of response surface generation is presented in Fig. 19. The experimental line shapes are first

* The weighted sum of the squared residuals

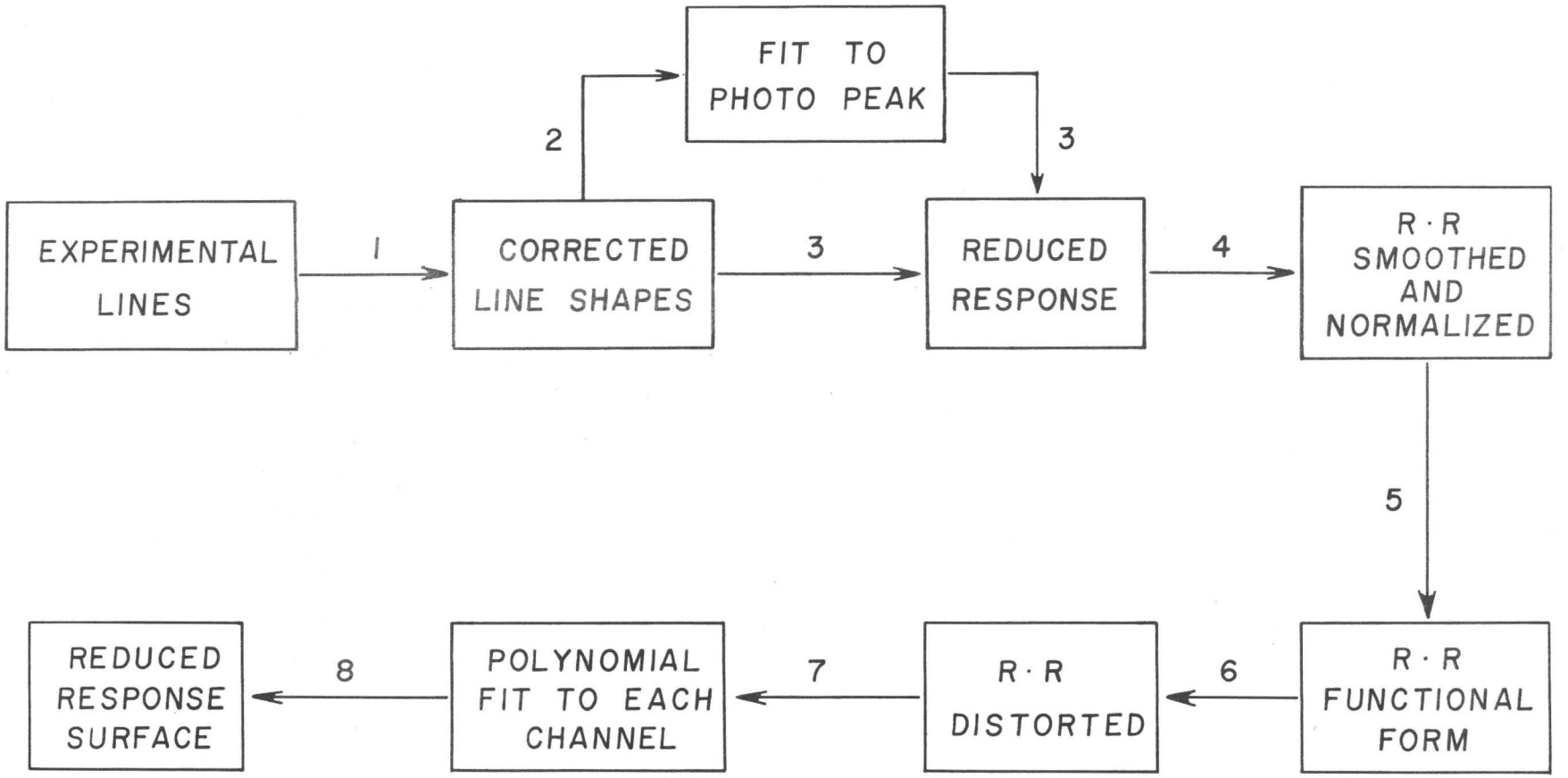

FIGURE 19 GENERATION OF RESPONSE SURFACE

modified to remove the contribution of X-rays, bremsstrahlung, etc. (step 1) so that they will represent as closely as possible functions of the detector for a series of monoergic photons of specified energies.

The only part of the response function of NaI(Tℓ) detectors that lends itself to a simple analytic description is the full energy peak, which approximates a Gaussian very closely, particularly on the high energy side. In step 2, the full energy photo peak is fitted to a function of the form

$$Y = A \exp\left[\frac{(x - x_o)^2}{2\sigma^2}\right] \qquad (2)$$

using a non-linear least squares fitting technique to be described later. In this expression A is the peak height, x_o is the centroid of the Gaussian and σ is the variance of the Gaussian. The initial values of A, x_o and σ are obtained by graphical estimates. The parameter σ is a function of incident photon energy and is fitted to an expression of the form

$$\sigma(E) = \frac{a}{E} + b + CE \qquad (3)$$

The fit to the Gaussian is made with data points ranging from $(x_o - 0.7\sigma)$ to $(x_o + \sigma)$ over the peak. The low energy side of the peak tends to be distorted by small angle Compton scattering from the thick beta stoppers required for high energy beta rays. The high energy side of the peak tends to be distorted beyond $(x_o + \sigma)$ by the effects of random summing. It was thus felt wise to fit the Gaussian using only points relatively near the peak of the distribution. The Gaussian portion so fitted is subtracted from the total response function to yield the reduced response function which is then normalized to correspond to the re-

sponse for a Gaussian peak of 10^4 counts (Step 3). It should be noted that this reduced response overlaps the lower side of the Gaussian peak because of small angle compton scattering from material surrounding the detector.

The remaining response is smoothed (Step 4) to reduce statistical fluctuations from channel to channel by the application of a standard smoothing function[77] of the form

$$\bar{y}(x) = \frac{1}{21}\left[-2y(x-3) + 3y(x-2) + 6y(X-1) + 7y(x) + 6y(x+1) + 3y(x+2) - 2y(x+3)\right] \quad (4)$$

where $y(x)$ is the data point to be smoothed and $\bar{y}(x)$ is the smoothed value. The function (4) represents a least squares fit to the seven points in the neighbourhood of x.

The shape of the response function of a NaI(Tℓ) detector changes rather rapidly with photon energy and becomes increasingly complex as that energy increases. It is convenient to break the response surface into three sections corresponding to photon energies (i) from 0.06 MeV to 0.411 MeV (ii) 0.411 MeV to 1.368 MeV and (iii) 1.368 MeV to 3.100 MeV. The division has been made in this way because the appearance of the response function does not alter greatly within each section but changes quite dramatically from one to another. Section (i) is characterized by a prominent iodine escape peak and a growing Compton edge. Section (ii) is marked by a strongly developed Compton edge while section (3) shows Compton edges and escape peaks of growing prominence.*

* It was also necessary to analyze spectra containing gamma rays above 3.1 MeV. For such spectra, the third group may be replaced by a group which extended from 1.368 MeV to 5.0 MeV. Experimental line shapes above 3.1 MeV are not easily obtainable since the most favourable cases (Ca^{49}) are only simple down to about 3 MeV. It was thus felt wise to choose a section of the response surface for which good standards were available over about half of the section, and to augment these by a few higher energy standards whose responses could be accurately determined for energies above 3 MeV. The low energy portion of the response functions calculated for gamma rays above 3 MeV are not as securely established as those for the three regions discussed above but have proven to be adequate.

Within each of these sections, a Fourier fit is made to the response function at each of the standard photon energies, using an expression of the form

$$f(x) = a_o + \sum_{n=1}^{M} \left[a_n \cos \frac{2\pi nx}{d} + b_n \sin \frac{2\pi nx}{d} \right] \qquad (5)$$

where d is the total number of channels in the spectrum, x is the channel number and $M = \frac{d}{2}$ or $\frac{d-1}{2}$ depending on whether d is even or odd. The result of this procedure (step 5) is to produce a description of the reduced response function in analytic form.

Although the responses in a section are more or less similar, they do vary quite rapidly with photon energy. To achieve the maximum in accuracy in the interpolation procedure, it is convenient to divide the response function for each section into segments within which the response function changes rather gradually with photon energy. The boundaries between segments are chosen to correspond to the sharp changes in slope of the response functions with channel number created by backscatter peaks, Compton edges, etc. The segments and segment boundaries chosen for each of the three sections of the response surface are described in the first two columns in Table 5. The backscatter boundary was calculated from the formula $E_{B.S.} = E_\gamma' \left[1 + 1.76\ E_\gamma / 0.511 \right]^{-1}$ where E_γ' is expressed in channel numbers by X the centroid of the appropriate Gaussian for this photon energy. This is not quite the position of the 180° backscatter peak but represented very closely the observed backscatter peak in the geometry of our experiments. Similarly, the Compton edge was empirically defined by the formula $E_c = E_\gamma' \left[1 - \left\{ 1 + \frac{1.42}{0.511} \cdot E_\gamma \right\}^{-1} \right]$ which is close to but below the theoretical Compton

TABLE 5

Description of Segments of Response Surface

Section	Segments Used	Number of Channels in a Segment of the Distorted Spectrum	Number of High Energy Overlap Channels in Distortrd Spectrum	Total Number of Channels of Distorted Segment for Purposes of Analysis	Total Number of Channels in Distorted Response Function
0.059 to 0.411 MeV	Zero to Eγ	150	-	150	150
0.411 MeV to 1.368 MeV	(i) Zero to back-scatter	40	10	50	
	(ii) Back-scatter to Compton edge	70	10	80	170
	(iii) Compton to Eγ	40	0	40	
1.368 MeV to 3.1 MeV	(i) Zero to back-scatter	32	8	40	
	(ii) Back-scatter to second escape peak	70	10	80	
	(iii) Second Escape peak to first escape peak	50	6	56	248
	(iv) First escape peak to Compton edge	32	8	40	
	(v) Compton edge to Eγ	32	0	32	

edge. The first and second pair escape peak boundaries were located at the theoretical values of $E_\gamma - m_o c^2$ and $E_\gamma - 2 m_o c^2$ respectively.

Each of the segments of the response function defined by these boundaries was then compressed or stretched into an appropriate number of channels (Step 6), as described in column 3 of Table 5. Although this choice is in large measure arbitrary, enough channels must be chosen to make certain that no detail is lost in the distortion process. Each segment is extended on the high energy side to include sufficient overlap channels of the next segment to avoid discontinuities at the boundaries. The distorted response function was then found in the manner described below, using the Fourier coefficients provided by equation (5) at each standard photon energy. If r(E) is defined as the ratio of the number of channels in a segment of the undistorted spectrum to the fixed number of channels in the corresponding segment of the distorted spectrum, and if λ is the channel number in the distorted spectrum corresponding to channel x in the undistorted spectrum, it can easily be shown by integration of equation (5) that

$$F(\lambda,E) = a_o + \sum_{n=1}^{M} \frac{\sin \frac{\pi r n}{d}}{\frac{\pi r n}{d}} \left\{ a_n \frac{2\pi\lambda r}{d} + b_n \sin \frac{2\pi\lambda r}{d} \right\} \text{where } \lambda = x/r \qquad (6)$$

is the channel in the distorted response corresponding to channel x of the actual response and $F(\lambda)$ is the distorted response function. The variable λ for each segment runs over the range of values specified by the sum of the values in columns 4 and 5 of Table 5. The smallest value of λ for each segment is x_o/r where x_o the lower bound of the segment, is calculated in the manner described above. Figure (20) graphically represents the relationship between a response and a re-

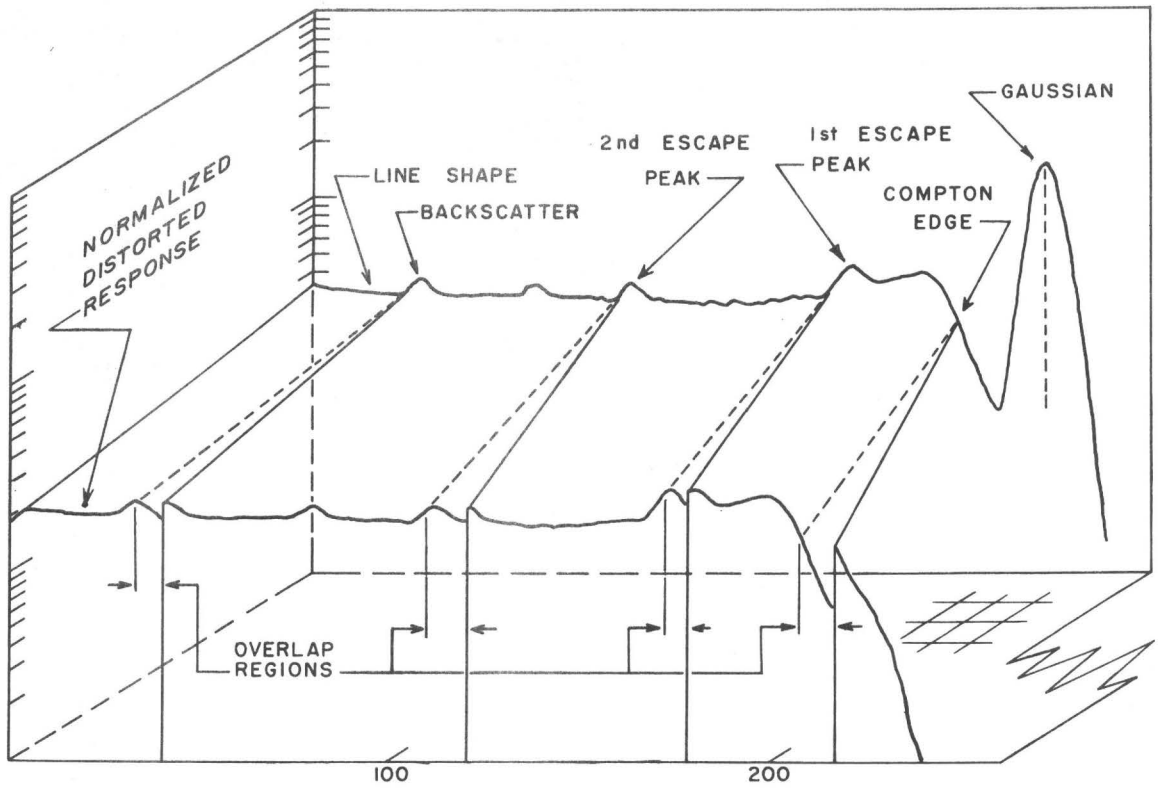

FIGURE-20 A NORMALIZED DISTORTED RESPONSE AT 1·78 MeV AND THE ORIGINAL RESPONSE

normalized distortion response.

The response surface is now generated by least squares fitting the $F(\lambda.E)$ values obtained from equation (6) for each λ within each segment to a polynomial of the form $F(\lambda,E_j) = \sum_{i=1}^{L} a_{\lambda i} E_j^{i-1}$ (7) where the number of coefficients (L) for each channel of the segment is less than the number of standard photon energies measured in the section (Step 7). In practice five or six standard lines were available for each section of the spectrum and so L was chosen to be one or two smaller than this number. By keeping L below the number of lines available, a certain amount of smoothing of the data is automatically achieved. The response surface is now represented by the coefficients $a_{\lambda i}$ which form three N by L matrices, one for each section of the spectrum (Step 8). The value of N is the total number of channels in the distorted response function (column 6 of Table I).

e Generation of Line Shapes

The flow pattern for the generation of the line shape for a photon of energy E is presented in Fig. 21 . The coefficient matrix, $a_{\lambda i}$, and expression (7) immediately yield (Step 1) the values of $F(\lambda,E)$ for any desired photon energy. In order to return to the undistorted spectrum, a Fourier fit of the form of equation (5) is applied to the $F(\lambda,E)$ values for each photon energy over the channels in each segment, including overlap (Step 2). This analytic expression for the response function for photon energy E in the distorted spectrum can be integrated (Step 3) to yield the undistorted response function using essentially the same procedure as was used to pass from the undistorted to the distorted response function in generating the distorted response surface.

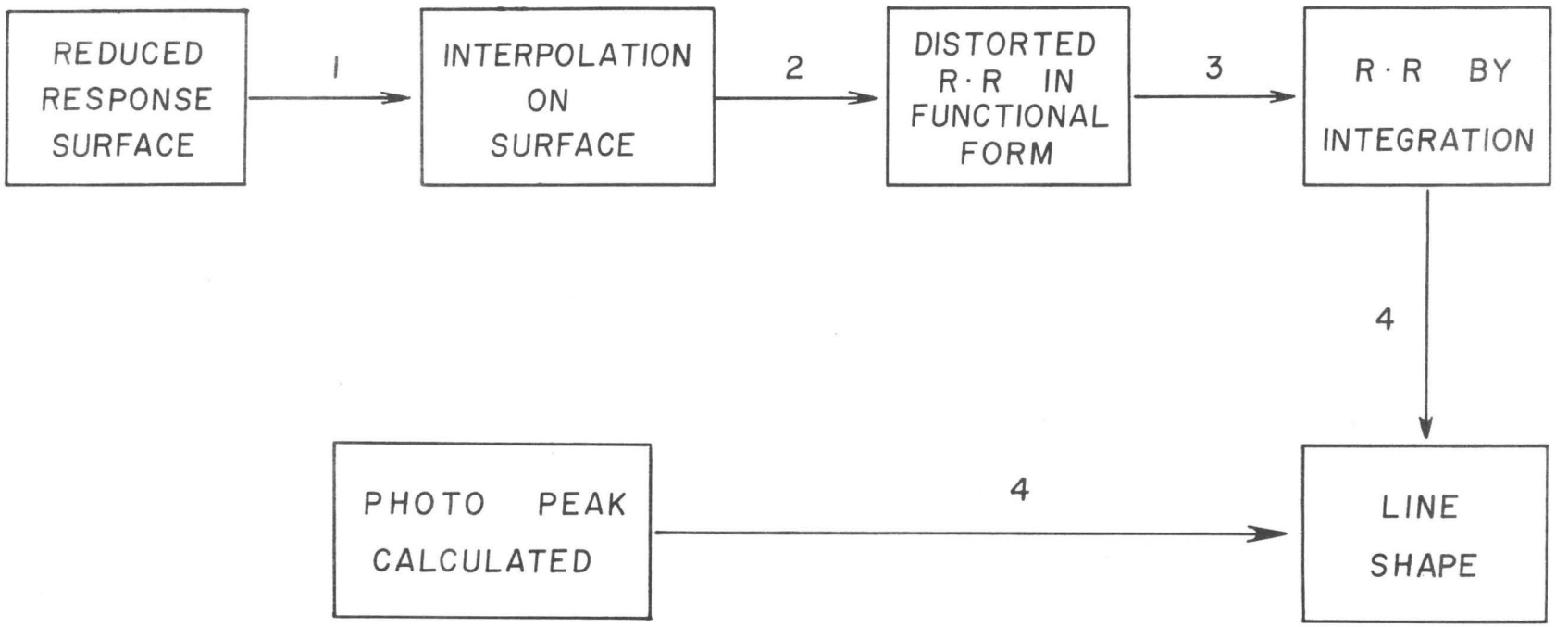

FIGURE 21 GENERATION OF LINE SHAPE FOR ARBITRARY ENERGY

In order to achieve a smooth transition from one segment to the next, the integration procedure is extended into the overlap region. This procedure eliminates discontinuities that may occur at the boundaries of the segments. The specific segment boundaries for the photon whose response was being calculated were derived from the same formulae used to set the boundaries for the standard lines.

The reduced response function was then combined with an appropriate Gaussian whose value was found using equation (3) to yield the total response function for the desired photon energy (step 4). In carrying out this process, the Gaussian was first calculated and then integrated into position. Figure 22 presents the experimental data points for the 0.411 MeV radiation of Au^{198} taken in the geometry of these experiments together with the response function generated in the manner described above. (The corrected input response represents the experimental response with the characteristic X-rays removed). The result of smoothing is clearly evident, but the agreement between the experimental and generated response functions is excellent.

Since the Fourier coefficients (Step 3) are sufficient to characterize a specific distorted response these were used in the analysis part to be described in section (g) below. This procedure eliminates step 1 and 2 of Figure 21 and results in a large saving in computer time.

It need hardly be pointed out that the response functions generated by any method can be no better than the experimental functions fed into the program. The errors which affect the standard line shapes (statistical errors, distortion through random summing, bremsstrahlung,

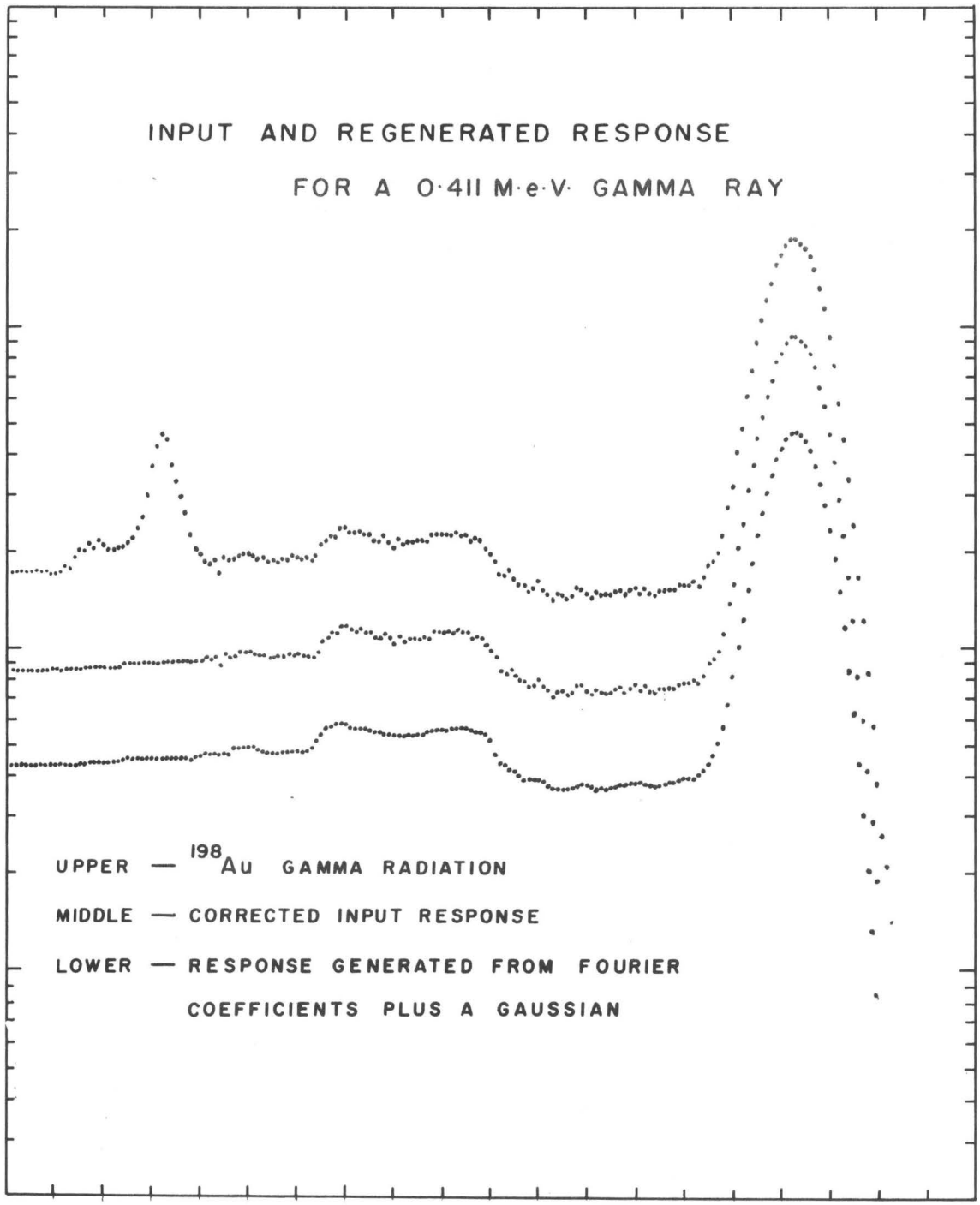
INPUT AND REGENERATED RESPONSE
FOR A 0·411 M·e·V· GAMMA RAY
UPPER — ^{198}Au GAMMA RADIATION
MIDDLE — CORRECTED INPUT RESPONSE
LOWER — RESPONSE GENERATED FROM FOURIER COEFFICIENTS PLUS A GAUSSIAN

FIGURE 22

non-linearity in the analyzer, etc.) also affect the spectra to be analyzed but in different ways. In dealing with rapidly decaying radioactive sources such as the fission product acitivities studied here, one soon reaches the place of diminishing returns in improving the quality of the response function by correcting for these effects.

f The Non-Linear Least Squares Fitting Procedure

This section deals with the general theory of non linear least squares fitting while its application to NaI spectra will be presented in section (g) below.

An examination of the residuals arising from a least squares fitting of the response functions to the data will reveal immediately any errors in the channel positions of the components and it would in principle be possible to readjust the set of photon positions slightly by inspection and then repeat the calculation until the residuals have been minimized. The program to be described is designed to ask the computer to discover and make the necessary adjustments in the photon energies to minimize the residuals without any interference from the operator. The method is introduced in its general form for completeness.

The response functions we are concerned with may be either linear or non-linear functions of the parameters and therefore the method must be applicable to both types of functions.

Suppose $L_\rho(\alpha^\nu)$ to be a set of ρ model functions (ρ=1, --- m) hereafter designated as $L_\rho{}^\nu$. Each model function is defined by a set of parameters α^ν(ν = 1, --- k). Let M(x) be the measured experimental function which is to be described in terms of the set $L_\rho{}^\nu$ and let W(x)

be the weight function of the parent distribution from which M(x) was obtained.

The method of least squares consists in finding values of the set α^{ν} which will minimize the sum

$$\chi^2 = \sum_{x=1}^{N} W(x) \left[M(x) - \sum_{\rho,\nu=1}^{m,k} L_{\rho}^{\nu} \right]^2 \qquad (8)$$

Here, M(x) is the measured spectra, a function of the channel number x.

W(x) is the weight function

L_{ρ}^{ν} is the set of model functions.

If L_{ρ}^{ν} is a linear function of the parameter α_{ρ}^{ν}, the mk normal equations can be derived from equation (8) by equating the partial derivatives of χ^2, with respect to each of the parameters, separately to zero. The normal equation derived for the parameter α_{λ}^{π} is

$$\sum_{x=1}^{N} W(x)\, M(x)\, \frac{\partial L_{\lambda}^{\nu}}{\partial \alpha_{\lambda}^{\pi}} = \sum_{x=1}^{m,k} W(x) \left[\sum_{\rho,\nu=1}^{m,k} L_{\rho}^{\nu} \right] \cdot \frac{\partial L_{\lambda}^{\nu}}{\partial \alpha_{\lambda}^{\pi}} \qquad (9)$$

and the set of mk linear equations of this form can readily be solved to give the mk parameters α_{ρ}^{ν}.

If the functions L_{ρ}^{ν} are non-linear functions of the parameters, the problem may be reduced to the linear least squares case by choosing a set of trial coefficients, $\alpha_{o\rho}^{\nu}$, fairly close to the true values, evaluating the L_{ρ}^{ν} functions in a Taylor expansion about $L^{\nu}(\alpha_{o\rho}^{\nu})$, and retaining only the first order term. Thus, for the λ^{th} model function,

$$L_{\lambda}^{\nu}(\alpha^{\nu}) = L_{\lambda}^{\nu}(\alpha_{o\lambda}^{\nu}) + \sum_{\nu=1}^{k} \left[\frac{\partial L_{\lambda}^{\nu}}{\partial \alpha_{\lambda}^{\nu}} \right]_{\alpha_{o\lambda}^{\nu}} \cdot \Delta\alpha_{\lambda}^{\nu} . \qquad (10)$$

The normal equation derived from the $\Delta\alpha_{\lambda}^{\pi}$ coefficient is now

$$\sum_{x=1}^{N} W(x)\, R(x) \left[\frac{\partial L_\lambda^\nu}{\partial \alpha_\lambda^\pi}\right]_{\alpha_{o\lambda}^\pi} = \sum_{x=1}^{N} W(x) \cdot \sum_{\substack{\rho=1 \\ \nu=1}}^{m,k} \left[\frac{\partial L_\rho^\nu}{\partial \alpha_\rho^\nu}\right]_{\alpha_{o\rho}^\nu} \cdot \Delta\alpha^\nu \cdot \left[\frac{\partial L_\lambda^\nu}{\partial \alpha_\lambda^\pi}\right]_{\alpha_{o\lambda}^\pi} \tag{11}$$

where $R(x)$, the residual in the x^{th} channel resulting from the choice $\alpha_{o\rho}^\nu$ in the parameters is

$$R(x) = M(x) - \sum_{\rho,\nu=1}^{m,k} L^\nu(\alpha_{o\rho}^\nu) \tag{12}$$

Equation (11) represents mk linear equations in the mk parameters $\Delta\alpha_\rho^\nu$ and can be dealt with in the same manner as equation (9). The solution of (11) can be used to generate new values of $\alpha_{o\rho}^\nu$ and the cycle repeated as often as needed.

In the matrix notation, we can write equation (11) as $M = LA$ where

$$M = \sum_{x=1}^{N} W(x)\, R(x) \left[\frac{\partial L^\nu}{\partial \alpha_\lambda^\pi}\right]_{\alpha_{o\lambda}^\pi} \quad \text{and} \quad A = \Delta\alpha_\lambda^\nu$$

are one column matrices with mk elements.

and

$$L = \sum_{x}^{N} W(x) \left[\sum_{\rho\,\nu}^{m,k}\right] \frac{\partial L_\rho^\nu}{\partial \alpha_\rho^\nu}\, \alpha_{o\rho}^\nu \left[\frac{\partial L_\lambda^\nu}{\partial \alpha_\lambda^\pi}\right]_{\alpha_{o\lambda}^\pi} \tag{12}$$

is a square matrix with mk x mk elements.

The solution of (11) is obtained by inverting L to yield

$$L^{-1} \times M = A \tag{13}$$

The errors in the coefficients $\Delta\alpha_i^\nu$ are given by the diagonal terms in L^{-1} through the relation

$$\sigma_{ii}^{\,2}(\alpha_i^\nu) = \frac{\chi^2}{N-mk} \cdot L_{ii}^{-1}$$

g Application to Complex Spectra

The complex spectrum is to be described as the sum of a number of response functions, each characterized by two adjustable parameters, the photopeak height, A, and the photo-peak position, X. In terms of the formalism above, the model function L^{ν}_{ρ} is the response function for the ρ^{th} gamma ray and it is characterized by two variables A and X (corresponding to $\nu = 1$ and $\nu = 2$). We can thus specify the response functions as L (A,X) where L is a linear function of A and a non-linear function of X. The measured function M(x) is the complex gamma ray spectrum which is to be resolved into L_{ρ} model functions with ρ taking values 1 to m.

The solution of the problem is given by equation (11). The zeroth order approximation to the fit is given by assigning values A_{oj} and X_{oj} to the intensity and photopeak position for each of the gamma rays in the spectrum. An examination of the L matrix (equation 12) reveals that a number of approximations and simplifications are possible. To see this, it is expanded below with certain changes in notation.

$$\text{Let} \quad f_j f_k = \sum_{x=1}^{N} W(x) \left[\frac{\partial L_j}{\partial A_j}\right]_o \cdot \left[\frac{\partial L_k}{\partial A_k}\right]_o$$

$$g_j g_k = \sum_{x=1}^{N} W(x) \left[\frac{\partial L_j}{\partial X_j}\right]_o \cdot \left[\frac{\partial L_k}{\partial X_k}\right]_o$$

$$g_j f_k = \sum_{x=1}^{N} W(x) \left[\frac{\partial L_j}{\partial X_j}\right]_o \cdot \left[\frac{\partial L_k}{\partial A_k}\right]_o$$

$\left[\frac{\partial L_j}{\partial A_j}\right]_o$ indicates that the partial derivative is to be evaluated at (A_{oj}, X_{oj}). In terms of these expressions, the L matrix may be expanded as

$$L = \begin{array}{cc} f_1f_1 \text{ ------- } f_1f_m & f_1g_1 \text{ ------- } g_1g_m \\ \vdots \qquad\qquad \vdots & \vdots \qquad\qquad \vdots \\ f_mf_1 \text{ ------- } f_mf_m & g_mf_1 \text{ ------- } f_mg_m \\ g_1f_1 \text{ ------- } g_1f_m & g_1g_1 \text{ ------- } g_1g_m \\ \vdots \qquad\qquad \vdots & \vdots \qquad\qquad \vdots \\ g_mf_1 \text{ ------- } g_mf_m & g_mg_1 \text{ ------- } g_mg_m \end{array}$$

The elements f_jf_k in this matrix are all formed as sums of weighted products of partial derivates of response functions with respect to their intensity parameters. Since these derivates all have the same shape as the response functions themselves, their products are all positive quantities and so all the elements, f_jf_k, are positive and relatively large with the largest elements along the diagonal. The elements g_jg_k are similar sums of products of partial derivatives of the response functions taken with respect to X. Since a change in X is merely a change in the scale of the response function along the channel axis, it is evident that $\frac{\partial L}{\partial x} = -\frac{\partial L}{\partial X}$ and that these partial derivates are very small except on the sides of the photopeaks. See Figure 23. We can thus expect all the elements to be very small except for the diagonal terms g_jg_j. The elements of the other two quadrants, f_jg_k, will also tend to be small since all elements of the sum are roughly equally distributed with respect to algebraic sign.

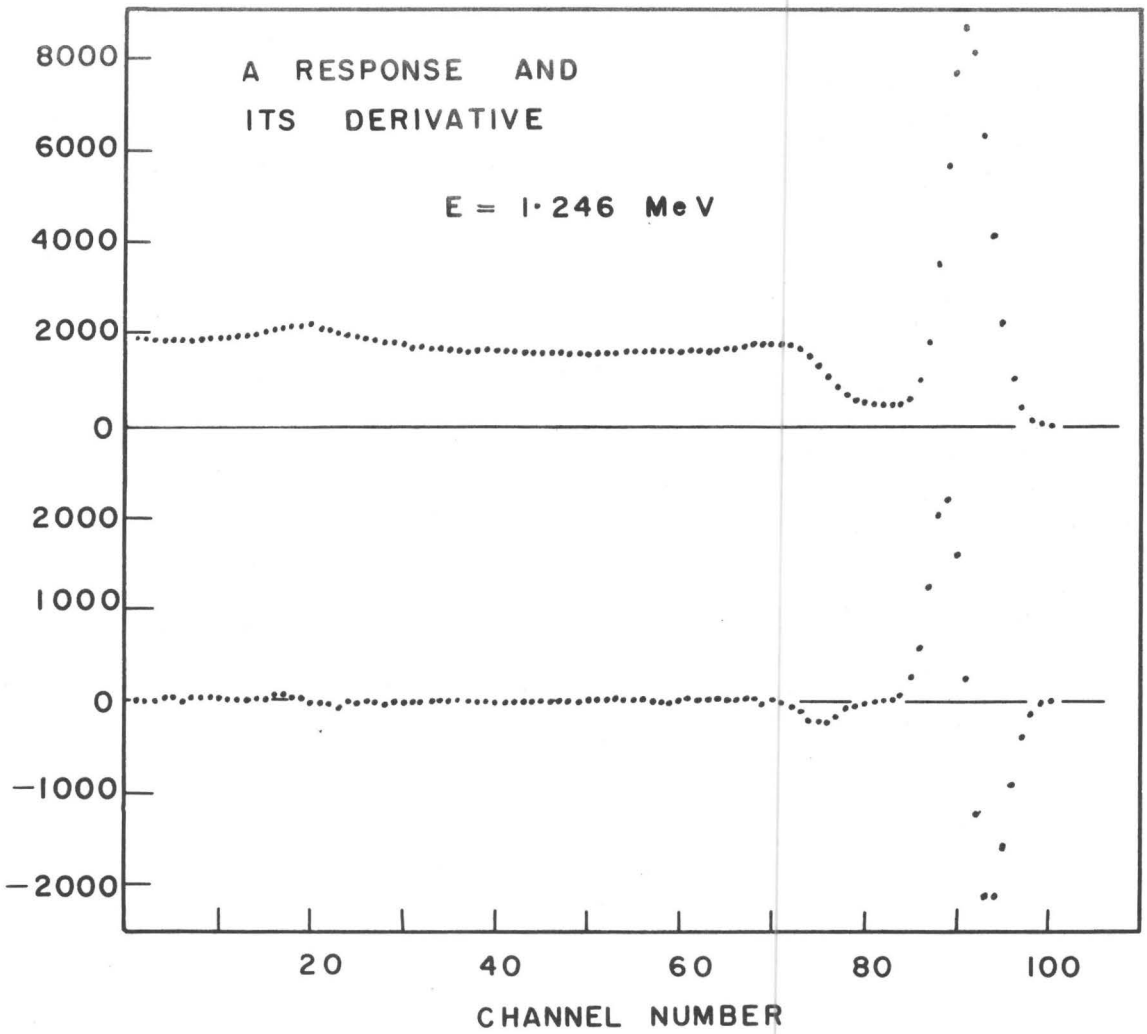
A RESPONSE AND
ITS DERIVATIVE
E = 1·246 MeV
8000
6000
4000
2000
0
2000
1000
0
−1000
−2000
20
40
60
80
100
CHANNEL NUMBER

FIGURE 23

If the L matrix is not too large, it may be inverted as it stands and the values of ΔA_j and ΔX_j obtained from equation (13) used to adjust the zeroth order estimates (A_{oj}, X_{oj}). These adjusted values may then be used to compute a new L matrix and the process recycled. It converges rapidly so that only one or two iterations are required. The original values of A_{oj} and X_{oj} are estimated visually from the spectrum.

Since in many cases it is necessary to analyze spectra containing many components one can be faced with inverting very large matrices. In such cases, several approximate methods are adequate. The first of these takes advantage of the fact that the elements $f_j g_k$ are generally small and assumes all elements in the first and third quadrants of the L matrix are zero. With this assumption, the L matrix breaks into two m x m matrices; the inverted $f_i f_j$ matrix leading directly to the A_j parameters and the inverted $g_j g_k$ matrix leading to a set of corrections ΔA_j to the zeroth order approximations x_{oj} for the photopeak positions. Again the process converges rapidly, with only one or two iterations required to minimize the χ^2 parameter. In this approximation the solution for the A_j's may be carried out by linear least squares methods.

To reduce the complexity of the problem even further, one can set the small off diagonal terms of the $g_j g_k$ matrix equal to zero. In this approximation, inverting the $g_j g_k$ matrix becomes a trivial operation and the values of ΔX_j may be written down directly by an inspection of equation (11).

$$\Delta X_j = \frac{\sum_{x=1}^{N} W(x)\, R(x) \left[\frac{\partial L_j}{\partial X_j}\right]_o}{\sum_{x=1}^{N} W(x) \left[\frac{\partial L_j}{\partial X_j}\right]^2} \qquad (14)$$

Since most of the contribution to the sums in equation (14) comes from channels on the flanks of the photopeak and since we are only interested in making small adjustments to this channel position of the photopeak, one can limit the summation to the region from $x_o - \rho$ to $X_o + \rho$ without loss of accuracy. Equation (14) then becomes

$$\Delta X_j = \frac{\sum_{x=X_o-\sigma}^{X_o+\sigma} W(x)\, R(x) \left[\frac{\partial L_j}{\partial X_j}\right]_o}{\sum_{x=X_o-\sigma}^{X_o+\sigma} W(x) \left[\frac{\partial L_j}{\partial X_j}\right]_o^2} \qquad (15)$$

Equation (15) can be used to calculate each ΔX_{jo} and the results so obtained used to create new model functions for the next iteration. Usually only one or two iterations are needed to minimize χ^2.

Figure 24 presents graphically the results of an incorrect choice of X and A in the fitting of L to the measured spectrum. The three columns in the figure show the situation corresponding to the cases where X is larger and smaller than the true value and where A is smaller than its true value.

The measured and model spectra are shown in the first row of each column and the corresponding residuals in the second row. The next set of diagrams show $(\frac{\partial L}{\partial X})_o$ while the fourth series of sketches present the functions within the summation sign of the numerator of equation (15). Since the denominator of equation (15) is always positive, it is clear that the sign of ΔX is determined by the sign of the area under the curves of the last row of Figure 24. The fact that the area of the curve in the fourth row of the last column is zero for the case where the amplitude of the lines was incorrectly chosen merely stresses the fact

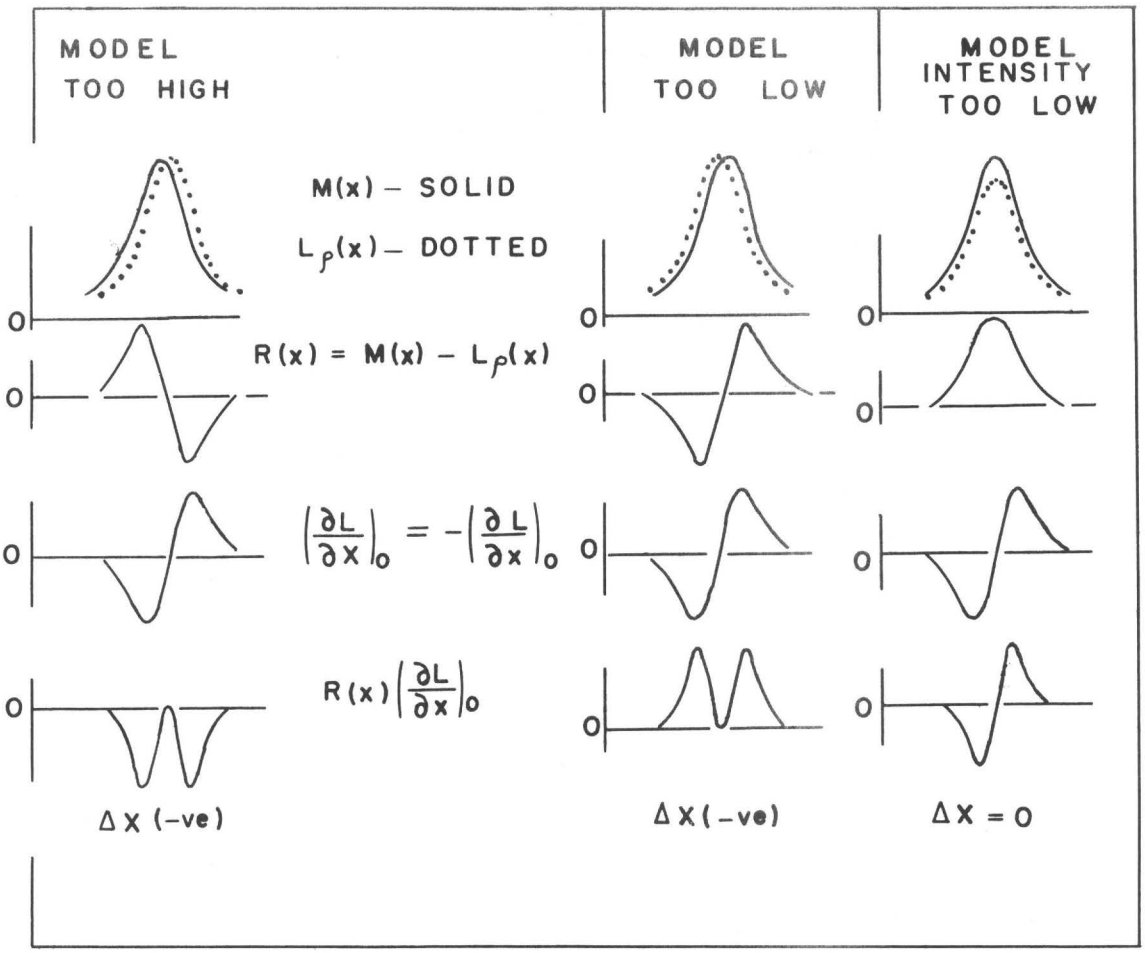

FIGURE 24

GRAPHICAL INTERPRETATION OF EQ'N 15

that to first order, adjustments of A and X can be made independently.

h Computational Details

Since the component gamma ray energies are assumed to be known the procedure outlined above is used to construct Fourier coefficients describing each member of the set of gamma rays present in the spectra. Once such a procedure is undertaken it need not be repeated so long as the geometry of the experiment is not changed for the spectra under study. The set of Fourier coefficients characterizing the component gamma ray responses is initially stored on the disk file of the McMaster 7040 computer. The input data includes the values of A and X_o, the energy of the gamma ray lines present in the spectrum, the spectrum to be analyzed and background or chance contributions. The required Fourier coefficients are selected from the disk file and with the aid of A_o and X_o are transformed into responses at the required gain and intensity. The Gaussian portion is calculated and integrated into position in order to take account of finite channel width. The spectrum is corrected for chance or background, the weighting matrix is formed and the least squares fit carried out. The changes in A and X_o are calculated and the component responses re-computed and the process recycled. Three cycle iterations of a spectrum with about 30 components typically required about twenty minutes of computer time.

i NaI(Tℓ) Efficiency Curves

The efficiency of detection of gamma radiation by a detector is an essential piece of information to the experimenter since it enables him to relate the number of events observed to the number that occurred.

A computer programme was written to evaluate the function $(i - e^{-u\gamma})dx$ along all possible paths from the source through the detector, using tabulated values of the absorption coefficients[78]. In addition, the effect of the beta stoppers was included in a calculation which, as a first approximation, assumed that all radiation scattered in the forward cone from the 2.54 cm thick beta stopper contributed to the total response of the gamma ray and therefore to the total efficiency. Figure 25 shows the effect of the beta stopper on the efficiency. The upper curve is identical with that obtained by Heath[79].

j Coincidence Quotients and Coincidence Probabilities

The reduction of the corrected γ-γ coincidence data to quantitative numbers is carried out by either of two related methods. These methods reduced the data to "coincidence quotients" or to "coincidence probabilities" which are terms used to describe the existence of time correlations between events.

If N_i represents the number of gamma rays of type i recorded in detector 1 which are in coincidence with a window in the gamma ray spectrum received by counter 2, then the following expression is true

$$N_i = N_o \, (w\epsilon)_{1i} \sum_j F_{2j} \, (w\epsilon)_{2j} \, \delta_{ij} \qquad (16)$$

Here N_o is the absolute source strenghh (disn/sec), F_{2j} is the fraction of gamma ray j detected in the window and δ_{ij} is the coincidence probability (coinc/decay) connecting gamma ray i and j. In this expression the effect of beta stopper absorption is included in the solid angle efficiency factor $(w\epsilon)$, while angular correlation effects are ignored.

In terms of coincidence quotients the coincidence relationship

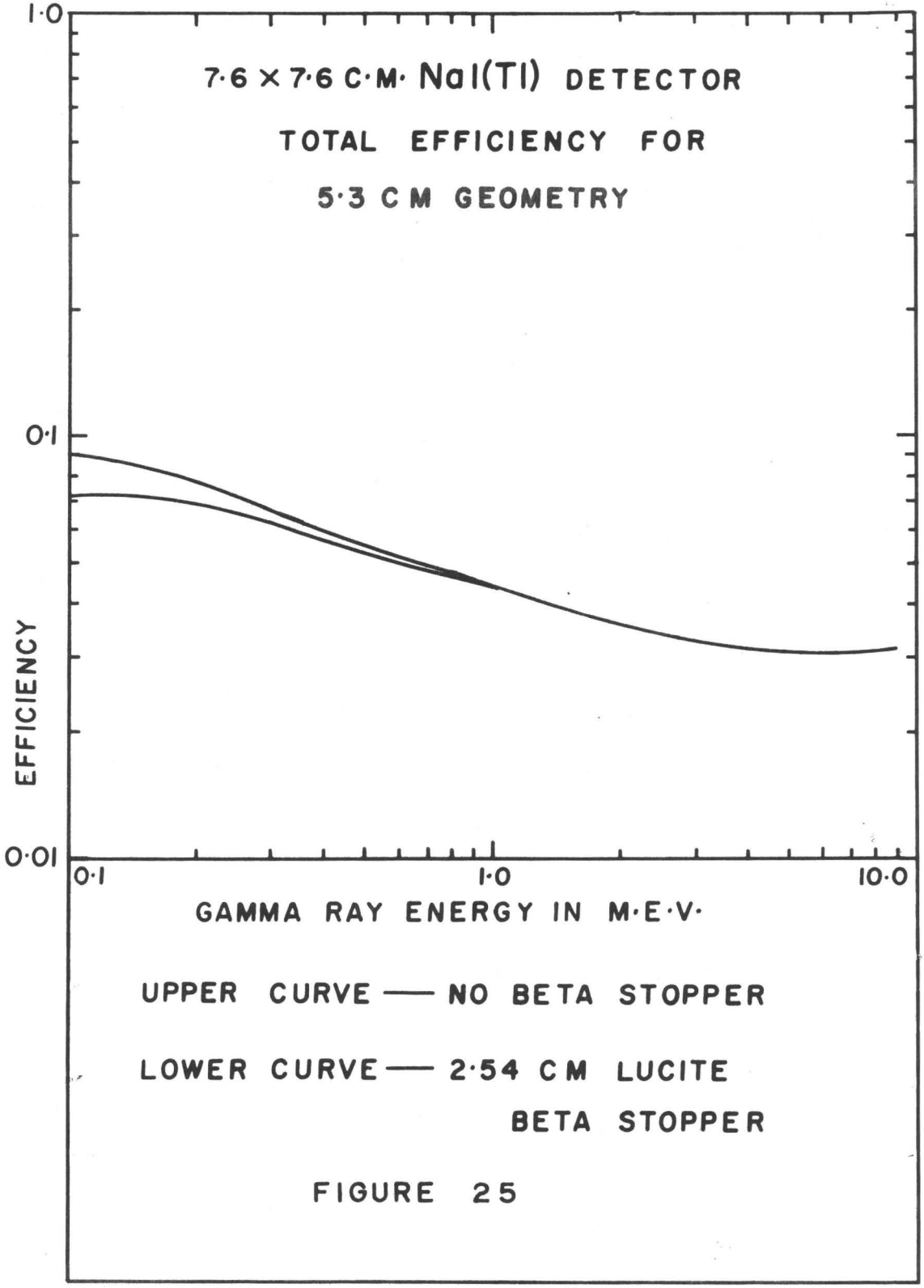
1·0
0·1
0·01
EFFICIENCY
7·6 × 7·6 C·M· NaI(Tl) DETECTOR
TOTAL EFFICIENCY FOR
5·3 C M GEOMETRY
0·1
1·0
10·0
GAMMA RAY ENERGY IN M·E·V·
UPPER CURVE — NO BETA STOPPER
LOWER CURVE — 2·54 C M LUCITE
BETA STOPPER

FIGURE 25

may be expressed as

$$N_i = (\omega\epsilon)_{1i} N_{2g} \sum_j P_{2j} Q_{ij} \qquad (17)$$

Here N_g is the total number of events passed by the window and P_j represents the fraction of these events belonging to gamma ray j. Q_{ij} is the coincidence quotient expressing the fraction of gamma ray j in coincidence with gamma ray i. The relationship between coincidence probabilities and coincidence quotients may be seen by expanding equation (17) as

$$N_i = N_o (\omega\epsilon)_{1i} \sum_j \lambda_j (w\epsilon)_{2j} F_{2j} Q_{ij} \qquad (18)$$

where λ_j is the absolute intensity of gamma ray j. By comparing equations (16) and (18) one obtains

$$\lambda_j Q_{ij} = \delta_{ij} \qquad (19)$$

Thus the coincidence probability is obtained from a coincidence quotient by multiplication of the quotient by the absolute intensity of the gamma ray in the window. Both of these methods of analysis are used in the present work; the coincidence quotients being used when the absolute source strength is not known.

Since gamma ray i may occur in a number of experiments and since it may be in coincidence with more than one gamma ray one obtains a set of equations involving this radiation. If α labels the different experiments in which this gamma ray occurred then the equations

$$\frac{N_{i\alpha}}{(\omega\epsilon)_{1i}} = N_{2g\alpha} \sum_j P_{2j\alpha} Q_{ij}$$

must be solved in order to determine the various Q_{ij}'s that may arise.

The weight matrix used in this solution is obtained by an iterative technique[66] since the independent variables $P_{2j\alpha}$ are subject to uncertainty. This variance arises from a determination of the gate fractions from an analysed singles spectrum. Moreover these numbers have an additional uncertainty because of the possibility of slight window drifts occurring during the course of the experiments. These drifts, presented in Figure 26 for a typical window fraction determination, are difficult to estimate and are normally ignored.

The first approximation to the weight factor , $w_{i\alpha}$, is $\frac{1}{(\sigma_{i\alpha}^2 + 1)}$, when $\sigma_{i\alpha}^2$ is the statistical error in the number of counts associated with $N_{i\alpha}$. Using this factor a solution for the various Q_{ij}'s is obtained and used in the second approximation for the weight factors given by $\frac{1}{w_{i\alpha}} = \sigma_{i\alpha}^2 + 1. + \Sigma_j \sigma^2(P_{2\alpha}) \cdot (Q_{ij})^2$. These factors are used to obtain the second approximation to the Q_{ij}'s and their variances; this cycle is then reiterated until convergence is obtained.

k Solid State Detector Data

The resolution of solid state detectors is extremely good, with the Gaussian portion of the full energy peak being 3 to 10 keV at F.W.H.M. for the detectors used in this work. The remaining portion of the response is similar to that for a NaI(Tℓ) detector as can be seen by a comparison of Figure 13 with Figure 12. Normally Ge(Li) detectors are used for precise energy determinations and therefore only the full energy or escape peaks are used. For gamma ray energies above 3 MeV visual estimates of the centroids of these peaks are normally sufficient to determine the gamma ray energies to the precision justified by the

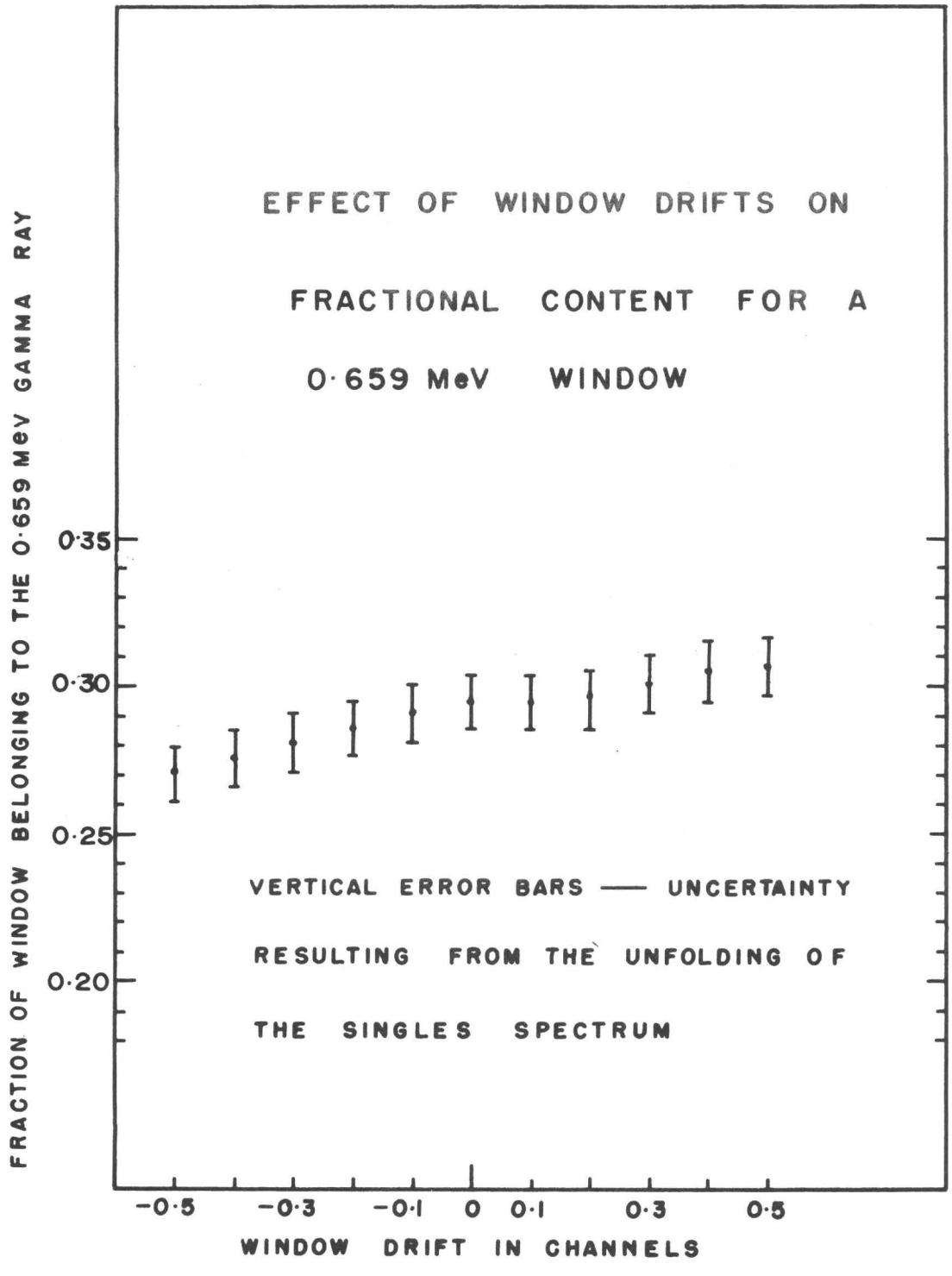
EFFECT OF WINDOW DRIFTS ON
FRACTIONAL CONTENT FOR A
0·659 MeV WINDOW
FRACTION OF WINDOW BELONGING TO THE 0·659 MeV GAMMA RAY
0·35
0·30
0·25
0·20
VERTICAL ERROR BARS — UNCERTAINTY
RESULTING FROM THE UNFOLDING OF
THE SINGLES SPECTRUM
−0·5
−0·3
−0·1
0
0·1
0·3
0·5
WINDOW DRIFT IN CHANNELS

FIGURE 26

available standard calibrations. For low energy gamma rays, on the other hand, there are many precisely known standards available and a least squares fitting procedure may be justified. The precise determination of line energies obtained from Ge(Li) spectra requires that account be taken of the non-linearity of the multichannel analyser. Since this is normally a smoothly varying function of channel number[82], its effects may be minimized by use of standard calibrations which fall close to the line whose energy is desired. Alternatively, one may describe the non-linearity analytically and use this function to correct all the data. This function should be determined for each experiment since the non-linearity is dependent on the properties of the amplification chain as well as the analyser.

1 Magnetic Beta Ray Spectrometer

The response function of the Gerholm spectrometer was symmetric and approximately Gaussian in shape with a full width at half maximum of 2.7% in the experiments to be described. The magnetic spectrometer window width is proportional to momentum, and all the counting rates on the continuum must be corrected for this window width variation by dividing the data by the momentum. The counting rates per unit momentum were then subjected to Fermi analysis to facilitate end point and intensity determinations. A computer program was written to generate the required Fermi function, $F(z,p)$ and to carry out a least squares fit to the data in order to evaluate the end points of the partial beta groups within the total spectrum and their relative intensities. For cases in which many beta groups were present this was done by fitting expressions of the type $K^2(E_o-E)^2$ to the corrected data $\frac{N}{p^3 F(z,p)}$, using

the parabolic method[66]. The energy differences between the end-points of the partial beta spectra were regarded as known from the gamma ray measurements so that the analysis was only required to yield values of the total Q and the intensities of the partial beta spectra. Some preliminary guidance as to the beta groups present was obtained by "hand stripping" the data but the "serious" analyses were all done with the aid of the computer.

m Plastic Beta Detector Data

The response of plastic detectors to monoergic beta particles, as has been previously noted, consists of a Gaussian full energy peak plus a flat backscatter region. Slavinskas et al[82] have shown that the equation

$$\underline{M} = \underline{R}\,\underline{N} + \underline{V} \text{ (see section a)}$$

may be written as

$$\underline{M} = \underline{L}\,\underline{G}\,\underline{N} + \underline{V} \text{ where}$$

The response matrix is written as the product of two triangular matrices, one describing that part of the response due to the backscattered region, ($\underline{L}$) and the second that belonging to the Gaussian portion, ($\underline{G}$). Furthermore these workers have demonstrated that the matrix $\underline{L}$ may be written in closed analytical form. In addition the inverse of this matrix, $\underline{L}^{-1}$, may also be written in closed form thereby greatly facilitating the reduction of data.

A first approximation to the true spectrum N is given by

$$\underline{N}^{1} = \underline{L}^{-1}\,\underline{M} = \underline{G}\,\underline{N} + L^{-1}\,\underline{V}$$

Apart from statistical deviations this transformation leaves the data in a form resembling the true spectrum as seen through a Gaussian res-

ponse. Since the resolution of a plastic scintillator is poor (16% at 0.662 MeV) and since a Gaussian is an effective smoothing function, the unfolding of $\underline{G}$, if it were possible, would produce large statistical amplification in the data. Therefore, since N^1 is a good approximation to $\underline{N}$, a least squares fit to the data is carried out in a solution for the beta end points and intensities. In using this procedure, one must leave out data near the end-point where the "shape" of the spectrum is seriously distorted by the broad Gaussian term in the response. Using the parameters obtained from this fit one may approximately unfold the Gaussian response with the help of the following equation .

$$\underline{S}^2 = \underline{S}^1 + \underline{N}^1 - \underline{G}\,\underline{S}^1$$

where S^1 is the beta spectrum generated from the least squares fit, (this hypothetical spectrum is thus devoid of statistical variation), and $\underline{S}^2$ is a second estimate to the true spectrum $\underline{N}$. Using S^2 as the final corrected data, the procedures outlined in the previous section are used to reduce the data to meaningful numbers. Since plastic scintillator data is recorded on a multichannel analyser which possesses constant width channels, no correction for variable window width is needed.

CHAPTER VI

THE DECAY OF ^{89}Rb

a Introduction

This chapter describes a series of experiments designed to establish a decay scheme for ^{89}Rb, using the various techniques outlined in the last three chapters. The gamma rays were studied by both germanium and sodium iodide detectors and included both "singles" and coincidence measurements. The beta rays were similarly examined with a magnetic spectrometer. Finally a γ-γ angular correlation experiment was carried out with one of the prominent cascades.

b Solid State Detector Spectra

The ^{89}Rb gamma rays spectrum was studied with an R.C.A. 2 mm thick Ge(Li) detector having a resolution of $\approx$ 7 keV at 0.662 MeV. Because of the high resolution of this device a study of the spectrum in reasonable detail required the use of a biased amplifier (Ortec Model 201). The spectrum was studied in sections with suitable overlap to obtain continuity. In some of the experiments standard sources were counted simultaneously with the ^{89}Rb spectrum while in others they were recorded before and after the accumulation of the ^{89}Rb spectrum. In all cases very low counting rates were used to avoid deterioration of the resolution or creating gain shifts. The full energy peak of the 1.031 and 1.246 MeV radiations and the second escape peak of the 2.195 MeV gamma ray were directly compared with the 1.173226

and 1.332423 MeV[83] radiations from ^{60}Co using a composite ^{89}Rb plus ^{60}Co spectrum. The 0.659 MeV radiation was similarly compared with the 0.6616 MeV radiation of ^{137}Cs. These ^{89}Rb lines were then used as secondary standards together with the lines from ^{22}Na, ^{24}Na[83], ^{65}Zn, ^{198}Au, ^{203}Hg and ^{207}Bi to obtain the energies of the remaining ^{89}Rb gamma rays. The more energetic photon energies were normally obtained from the second escape peaks since these fall close to well known calibration lines. The 1.536 MeV radiation was the most difficult to measure since its full energy peak is masked by the intense escape peak of the 2.567 MeV gamma rays. A composite spectrum of ^{89}Rb is presented in Figure 27 while the results are tabulated in Table 6. In this table, the first two columns present the energies and intensities while the third indicates the various ways in which these data were obtained.

c NaI(Tℓ) Coincidence Spectra

Coincidences were recorded using the standard fast-slow coincidence circuit shown in Figure 14 of Chapter IV. The left section of Figure 28 presents part of a typical singles spectrum together with the spectrum in coincidence with the 2.567 MeV radiation. It shows strong coincidences with the 0.659 MeV gamma ray and a weak contamination peak due to coincidences between the very strong 0.832 MeV radiation of ^{90}Rb (see Figure 7) and the Compton distributions of a large number of gamma rays of energies greater than 2.567 MeV in the ^{90}Rb decay. These data suggests that the ^{90}Rb gamma ray contaminant is less than 2% of the ^{89}Rb gamma spectrum in intensity. No coincidences attributable to ^{89}Rb were observed with gamma rays of energy greater than 2.567 MeV. The 2.708 and 3.500 MeV radiations thus are presumed to be ground state transitions.

The right section of Figure 28 presents coincidences with the 1.246 MeV (lower) and 1.031 MeV (upper) gamma rays respectively.

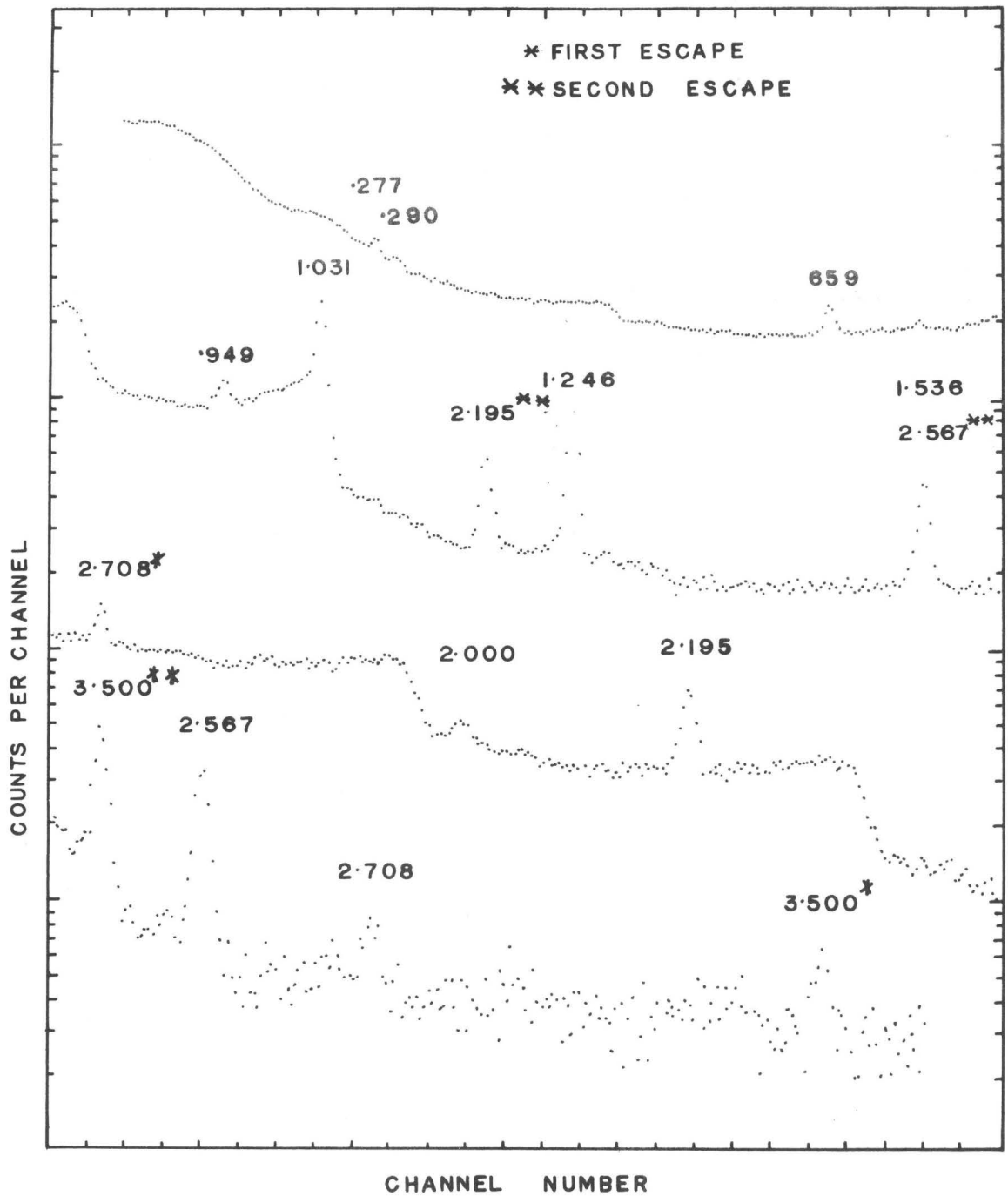

FIGURE 27 Ge(Li) SPETRUM OF ^{89}Rb

TABLE 6

Gamma Ray Energies

and Absolute Intensities

Energy keV	%	Detection Method
0.277 ± 0.004	2.2 ± 0.7	NaI,Ge,γ-γ
0.290 ± 0.004	0.5 ± 0.3	Ge
0.6588 ± 0.0003	10.7 ± 0.8	NaI,Ge,γ-γ,β-γ
0.770 ± 0.010	0.4 ± 0.1	γ-γ
0.9485 ± 0.0005	10.0 ± 0.9	NaI,Ge, γ-γ,β-γ
1.0307 ± 0.0003	60.0	NaI,Ge,γ-γ,β-γ
1.225 ± 0.010	0.75 ± 0.2	γ-γ
1.2464 ± 0.0003	46.6 ± 1.8	NaI,Ge,γ-γ,β-γ
1.536 ± 0.002	3.1 ± 0.3	NaI,Ge,γ-γ,β-γ
2.000 ± 0.004	4.5 ± 0.3	NaI,Ge,γ-γ,β-γ
2.1949 ± 0.0004	17.1 ± 1.0	NaI,Ge,γ-γ,β-γ
2.567 ± 0.001	12.0 ± 0.8	NaI,Ge,γ-γ,β-γ
2.708 ± 0.002	3.0 ± 0.3	NaI,Ge,β-γ
3.500 ± 0.005	2.7 ± 0.3	NaI, Ge

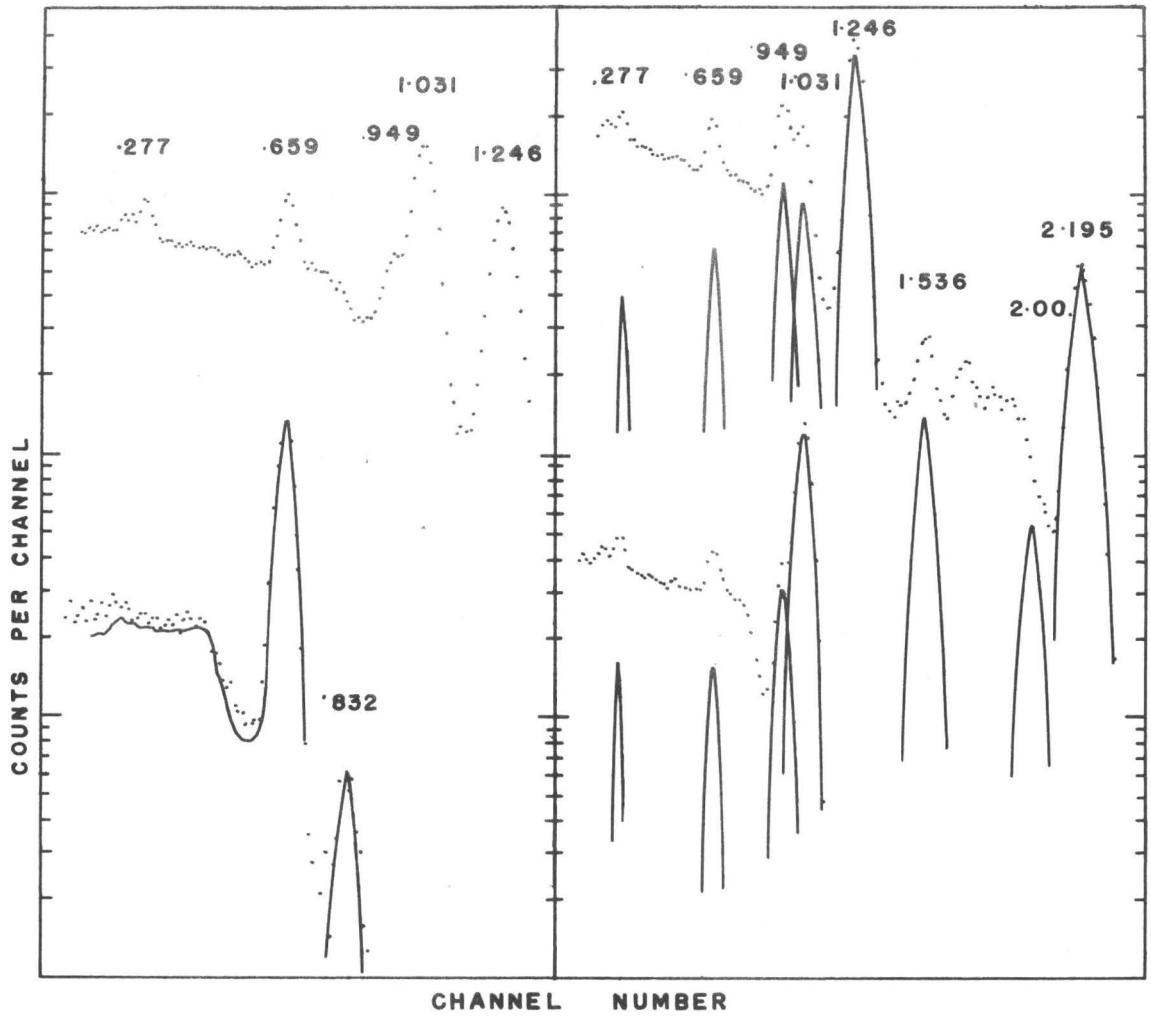

FIGURE 28

UPPER — GAMMA SINGLES
LOWER — COINC· WITH THE 2·567

UPPER — COINC· WITH THE 1·031
LOWER — COINC· WITH THE 1·246

The 0.659, 0.949, 1.246, 1.536 and 2.195 MeV radiations are clearly in strong coincidence with the 1.031 MeV transition while the 0.949 and 1.031 MeV radiations are in strong coincidence with the 1.246 MeV gamma ray. The other peaks are due to Compton distribution of other gamma rays falling in the windows. Figure 29 represents coincidences with the 2.000 MeV (lower) and 0.277 MeV (upper) gamma rays. The 2.000 MeV line is in coincidence with the 0.277, 0.770 and 1.225 MeV radiations, while the 0.277 MeV line is in coincidence with the 2.000 MeV radiation. The other peaks are due to Compton distributions in the gate. The weak 1.225 MeV radiation is observed only in coincidence experiments. This radiation appears as a weak gamma ray shifted from the position of the 1.246 MeV radiation and of intensity well above the chance rate expected. The 1.225 MeV radiation is 60 times weaker than the 1.246 MeV gamma ray; it proved impossible to obtain meaningful data concerning this cascade in the reverse experiment, with a window set on the 1.225 keV photopeak.

The 2.000 - 0.770 MeV coincidence pair also appears in coincidence with a gate set at 0.770 MeV. The 0.770 MeV and 1.225 MeV gamma rays are only observed in γ-γ coincidence experiments from which their absolute intensities of 0.4% and 0.75% respectively were deduced.

A gate set at 1.536 MeV reveals coincidence peaks at 0.659 and 1.031 MeV. Most of the intensity of the latter peak is attributed to coincidences with the 2.195 MeV radiation present in the gate. A gate set at 2.277 MeV produces coincidences with the 0.949 MeV radiation. However, a calculation of coincidence summing of the 1.246 - 1.031 MeV pair results in a 2.277 MeV sum peak of sufficient intensity to account for the observed 0.949 MeV coincidence; there is thus no good evidence

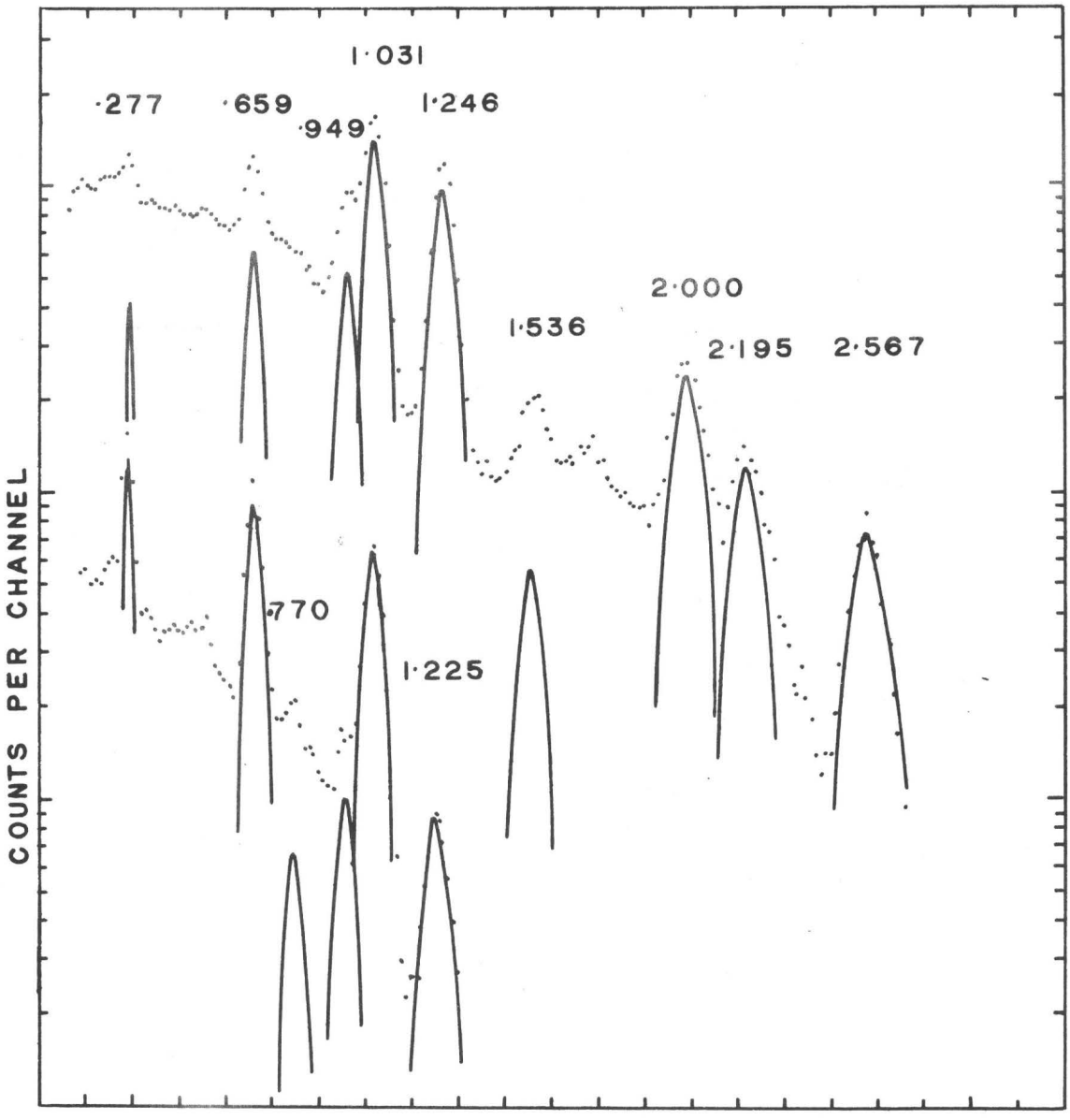

FIGURE 29

UPPER COINC· WITH THE 0·277

LOWER COINC· WITH THE 2·000

for a 2.277 MeV gamma ray in the spectrum.

d Coincidence Probabilities

Two sets of coincidence data comprising approximately twenty spectra each, were analysed by use of the non-linear least squares technique described in Chapter V. Each spectrum was reduced to the total number of counts due to each component gamma ray. During the course of the experiments, the total number of events falling within the windows were recorded. From these data and from an analysed singles spectrum it was possible to reduce the data to coincidence quotients by the methods of Chapter V. From a knowledge of the absolute intensity of each component gamma ray, the coincidence quotients were translated into coincidence probabilities and these are presented in Table 7. As might be expected, the agreement between the direct and reverse experiments is very good on strong cascades, and satisfactory in all cases.

c. Beta-Gamma Coincidence Measurements

The beta-gamma coincidence experiments were performed with the Gerholm beta ray spectrometer, using the arrangement shown in Figure 15 of Chapter IV. Using multiple sources, a sequence of gamma ray spectra in coincidence with beta rays selected from 26 equally spaced points on the beta continuum was obtained. Absolute NaI(Tℓ) detector efficiencies were determined in this geometry by a series of beta-gamma coincidence experiments on known nuclides such as ^{198}Au, ^{56}Mn, ^{51}V and ^{24}Na; and the gamma ray response functions were obtained using these and a wide range of other nuclides. The magnetic

TABLE 7

Coincidence Probabilities

GATES

	.277	.290	.659	.770	.949	1.031	1.225	1.246	1.536	2.000	2.195	2.567	2.708	3.500
.277					.0032 ±.0007					.017 ±.003				
.290														
.659						.026 ±.009			.027 ±.009			.102 ±.005		
.770										.004 ±.001				
.949	.003 ±.003					.100 ±.006		.107 ±.005		.008 ±.002				
1.031			.014 ±.028		.10 ±.03			.500 ±.04	.03 ± .02		.19 ±.01			
1.225										.009 ±.002				
1.246					.115 ± .012	.51 ±.02								
1.536			.021 ±.002			.030 ±.003								
2.000	.0194 ±.0006			.004 ±.001	.007 ± .001									
2.195						.202 ±.003								
2.567			.107 ±.011											
2.708														
3.500														

spectrometer was calibrated using internal conversion lines in the decay of ^{198}Au and ^{137}Cs and external conversion lines from ^{24}Na. Figures 30 and 31 show two typical gamma ray coincidence spectra; one with fairly high and the other with fairly low energy electrons, viz $B\rho$ = 7387 and 4100 gauss-cm respectively. An analysis of the series of spectra thus obtained, yielded the number of counts associated with each gamma ray as a function of momentum data, Fermi plots were calculated; some of these are shown in Figure 32. The 0.659, 0.949 and 2.195 MeV gamma rays are evidently in coincidence with a beta group having an end point of 1.261 MeV, while the 2.000 and 1.246 MeV radiations are associated with a beta group of end point 2.209 MeV. The beta spectrum associated with the 2.567 MeV gamma ray shows a weak beta group of end point 1.919 MeV and a much stronger group of end point 1.261 MeV. The beta spectrum associated with the 1.031 MeV radiation is characterized by strong 1.261 and 2.209 MeV beta components and a weaker 3.455 MeV high energy spectrum. The intensity of this weak high energy beta component was established by recording the weak gamma ray spectrum in coincidence with electrons of energy 2.475 MeV. This spectrum showed only the 1.031 MeV transition. When the focussed beta ray energy was reduced below 2.2 MeV, the 1.246 MeV gamma ray began to appear in the coincidence spectrum. The beta spectra associated with the 1.536 and 2.708 MeV gamma rays were observed but the data were not statistically meaningful for end point analysis.

f Angular Correlation Measurements

There are a number of γ-γ cascades in this decay process which might be studied by angular correlation measurements, while the 0.949 -

FIGURE 30 BETA GAMMA COINC.

FOR BP 7387

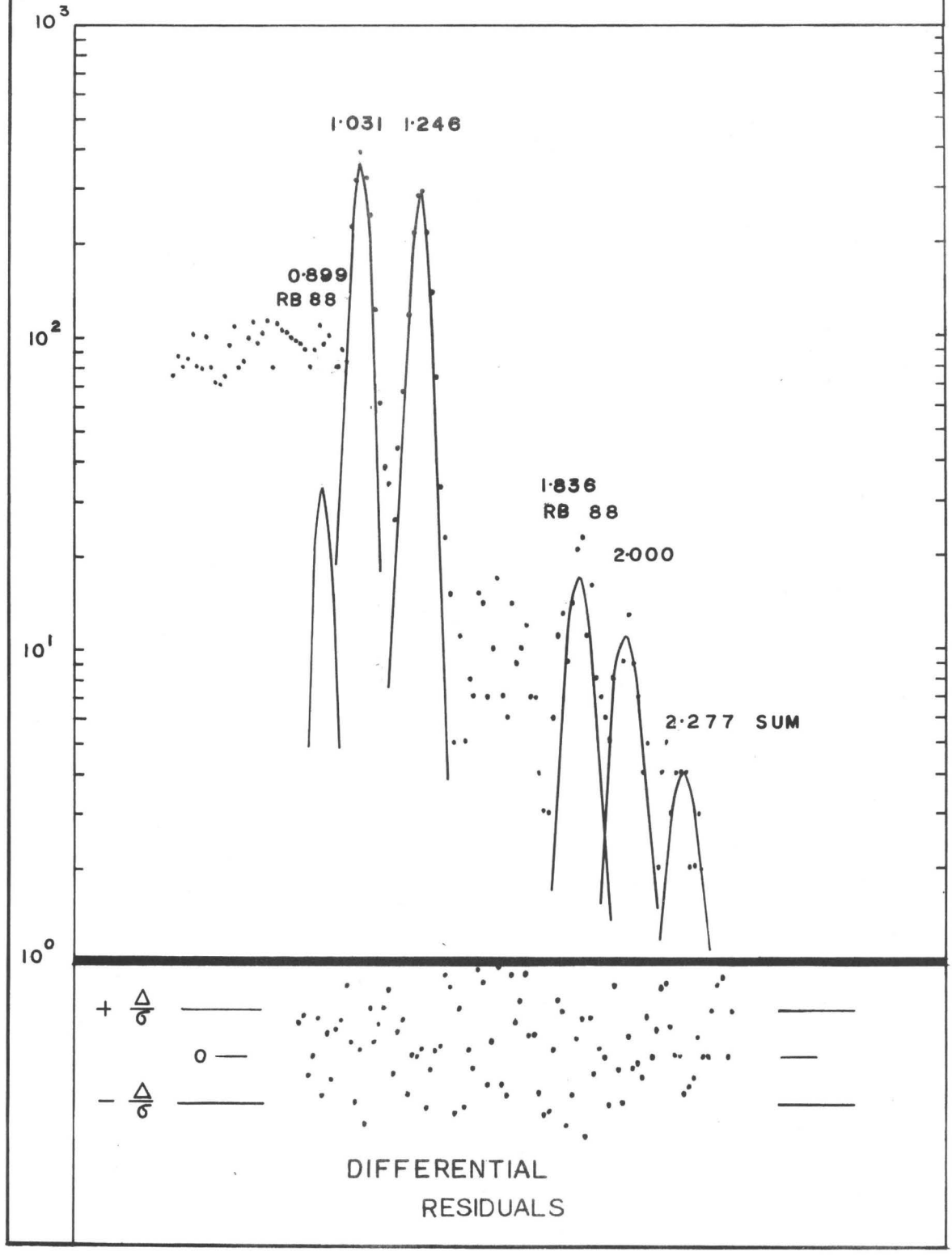

FIGURE 31 BETA GAMMA COINC.

FOR Bρ 4100

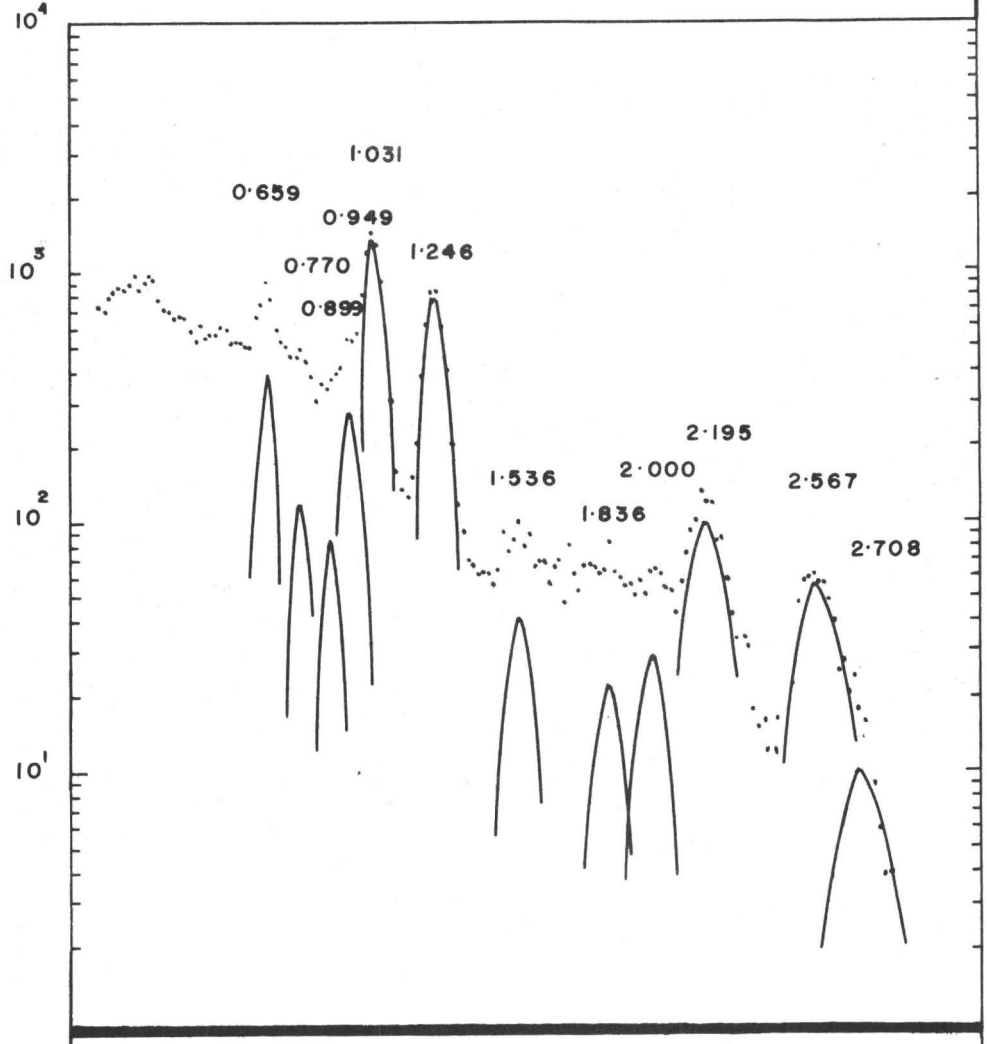

DIFFERENTIAL RESIDUALS

1.246, 0.277 - 0.949, and 0.277 - 2.000 MeV cascades are possible they are difficult candidates for study. The strong cascades proceeding through the 1.031 MeV level are all expected to be isotopic, since the spin of this state is 1/2. The only data reported here are for the 0.659 - 2.567 MeV cascades: work on the remaining cascades is to be undertaken by other members of this laboratory as a part of a larger programme.

The apparatus and techniques employed were described in Chapter IV. The ^{89}Rb activity was held on activated charcoal in small quartz tubes 2 mm in diameter and 4 mm long. The data were analysed in the manner described in Chapters IV and V, to yield a value of $A_2' = A_2/A_0 = 0.044 \pm 0.015$. The theoretical value for a $\frac{1}{2} - \frac{3}{2} - \frac{5}{2}$ cascade with pure dipole transitions is 0.05, in good agreement with these results. The data and the theoretical curves for a $\frac{1}{2} - \frac{3}{2} - \frac{5}{2}$ cascade are presented in Figure 33. This diagram shows the correlation functions expected for a number of other possible spin sequences consistant with the decay.

g Discussion of the Decay Scheme

The results of this sequence of experiments are summarized in the decay scheme of Figure 34. The levels at 1.031, 2.000, 2.277, 2.567 and 3.225 MeV are strongly established by both γ-γ and β-γ coincidence experiments. Since no coincidences were observed with the 2.708 and 3.500 MeV gamma rays, it is assumed that they are ground state transitions. The level at 2.770 MeV is established through the presence of the 0.770 - 2.000 MeV coincidence.

The Q value of 4.486 $\pm$ 0.012 MeV is based on a weighted av-

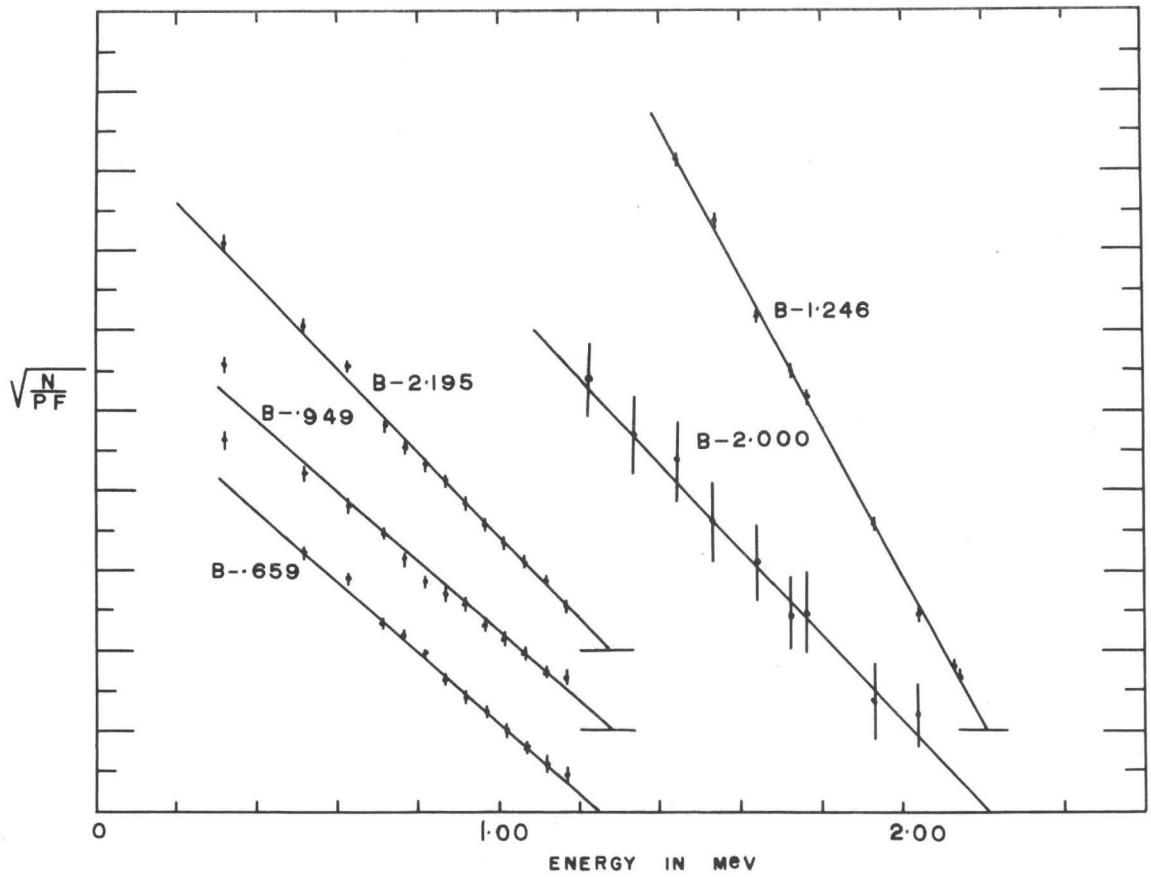

FIGURE 32

FERMI PLOTS FOR BETA-GAMMA COINC· DATA

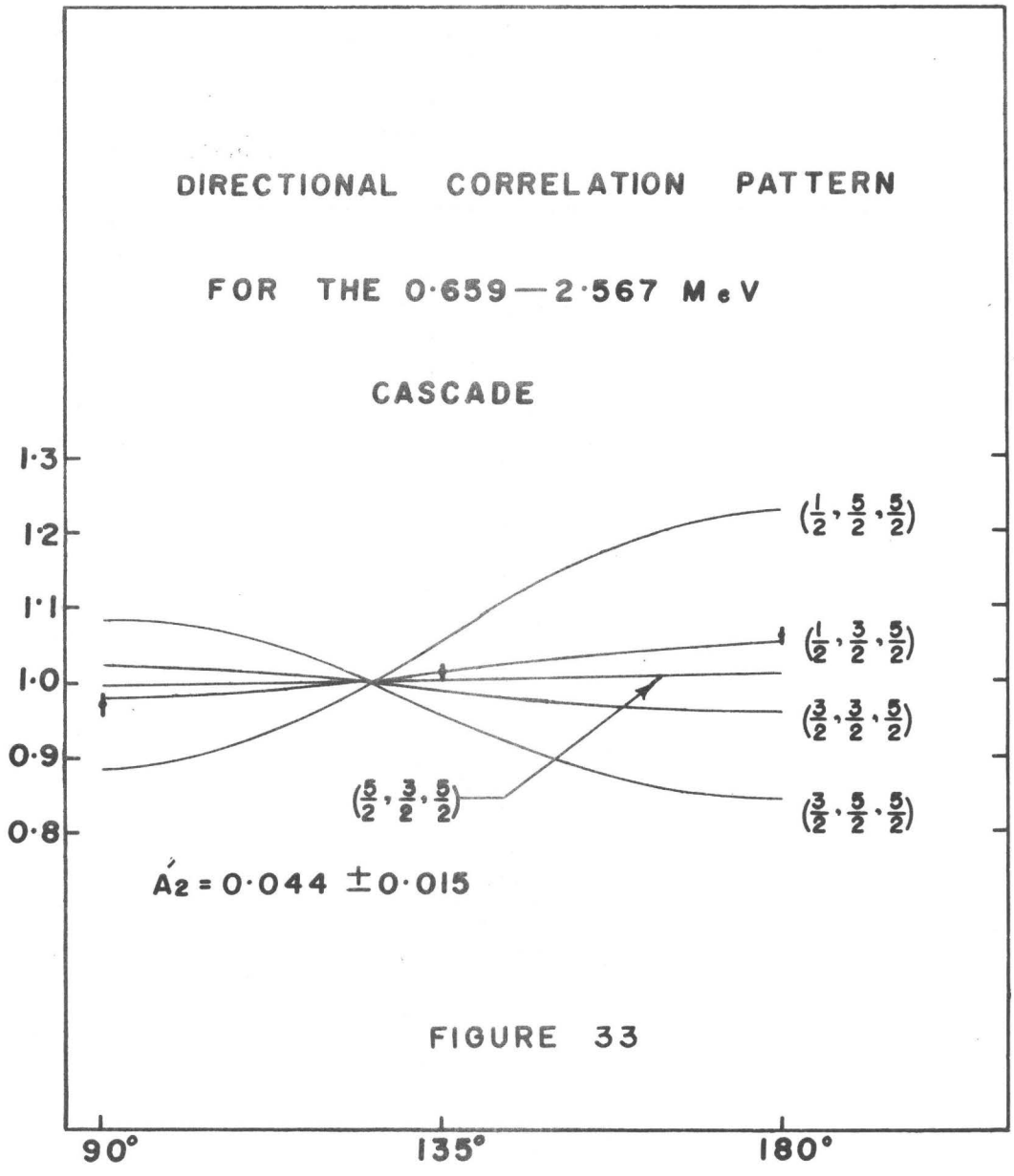
DIRECTIONAL CORRELATION PATTERN
FOR THE 0·659—2·567 MeV
CASCADE
1·3
1·2
1·1
1·0
0·9
0·8
(1/2, 5/2, 5/2)
(1/2, 3/2, 5/2)
(3/2, 3/2, 5/2)
(3/2, 5/2, 5/2)
(5/2, 3/2, 5/2)
A2 = 0·044 ±0·015
90°
135°
180°

FIGURE 33

age of energies derived from the beta coincidence spectra feeding the 1.031, 2.000, 2.277 and 3.225 MeV levels. The momentum range of the magnetic spectrometer did not permit a direct determination of the end-point of the ground state transition. However, the singles spectrum was studied out to 3.8 MeV about 1.6 MeV beyond the intense beta feed to the 2.277 MeV level. The beta intensity feeding the ground state was found by Fermi analysis of the singles spectrum assuming the ground state beta group to be linear between its end point at 4.486 MeV and the highest electron energy measured by the spectrometer. The intensities of the beta groups populating the ground, 1.031 and 2.277 MeV levels, as found from this singles analysis, was 18%, 1% and 37% respectively. The intensities of the remaining groups could not be reliably separated.

The β-γ data yielded absolute values of 56.4, 3.7 and 9.7 % for the total beta intensity coupled to the 1.031, 2.000 and 2.567 MeV gamma rays respectively. The sum of these three intensities, when augmented by the 5% contribution expected for the beta intensity feeding the 2.708 and 3.500 MeV transitions, leads to a total beta intensity of 75%. This value is in excellent agreement with the 82% figure obtained from the intensity of the ground state beta groups of the "singles" analysis. Since the 82% figure was considered to be less subject to systematic error, the total beta intensity feeding all excited states was normalized to this figure. The beta intensities shown in Figure 34 have been obtained from the β-γ coincidence data with the assistance from the gamma ray intensities in the case of unobserved beta transitions, renormalized to the 82% figure.

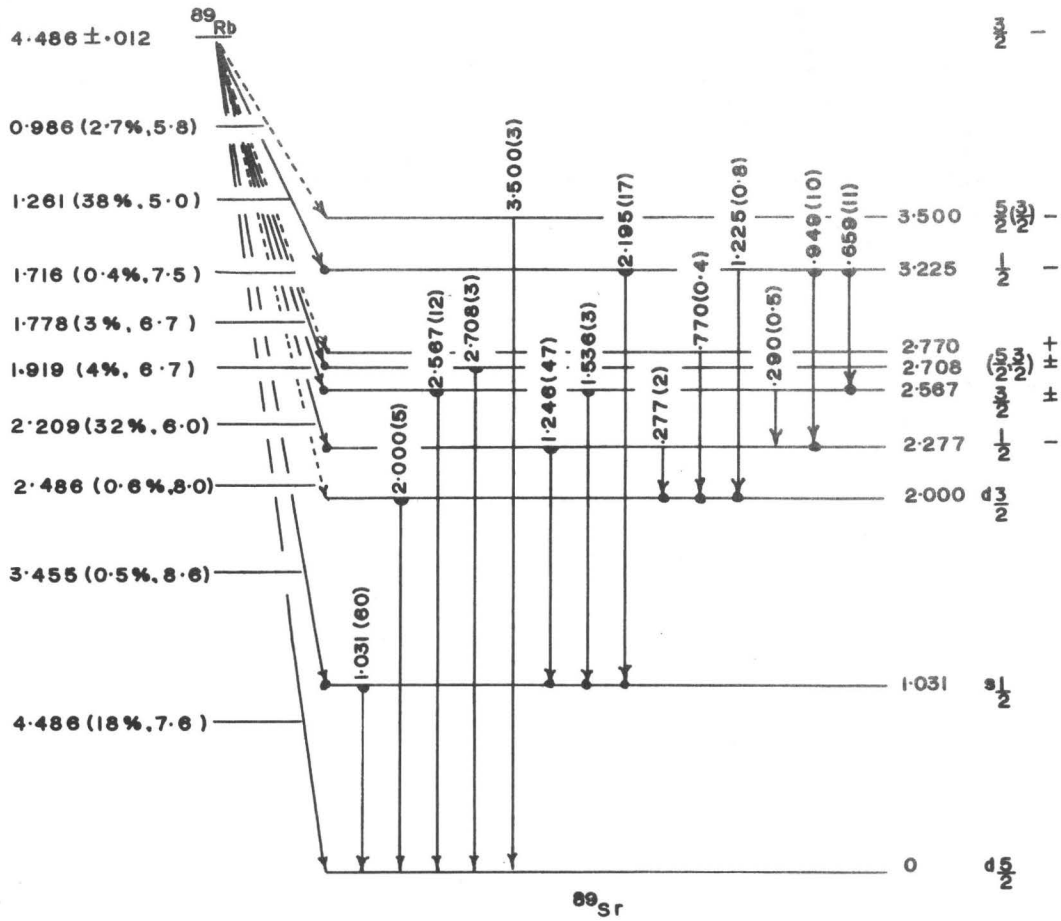

FIGURE 34 DECAY SCHEME OF ^{89}Rb

NOTE÷A HALF DOT INDICATES THE RADIATION WAS OBSERVED IN BETA GAMMA COINCIDENCE EXPERIMENTS

The total intensity of the gamma rays feeding the ground state was also renormalized to 82% to yield absolute transition probabilities for the photons found in this decay. The photon intensities of Table 6 may also be used with the decay scheme to calculate beta intensities. The values obtained in this way can readily be seen to be in good agreement with those found from the direct β-γ coincidence measurements supporting the consistency of the decay scheme.

Spin Assignments

The d-p reaction studies of Cohen[62], Preston et al[63], and of Sass et al[64] have shown that the ground 1.031 and 2.000 MeV levels in $^{89}_{38}Sr_{51}$ are the $d_{5/2}$, $s_{1/2}$ and $d_{3/2}$ configurations respectively. The shell model predicts that the ground state configuration of $^{89}_{37}Rb_{52}$ is either an $(f_{5/2})^{-1}$ or a $(p_{3/2})^{-1}$ hole state. The measured spins of ^{85}Rb and ^{87}Rb are 5/2 and 3/2 respectively, revealing the usual favoring of the low spin choice as the filling of a shell nears completion. Therefore, on the basis of the shell model, the ground state configuration of $^{89}_{37}Rb_{52}$ is expected to be $(p_{3/2})^{-1}$. This assignment is supported by the present experimental results.

The log $f_o t$ values for the beta rays populating the 0 MeV ($d_{5/2}$), 1.031 MeV ($s_{1/2}$) and 2.000 MeV ($d_{3/2}$) levels in $^{89}_{38}Sr_{51}$ are 7.6, 8.6 and 8.0 respectively, and are consistent with first forbidden decays in this region of the mass table. If one were to assume that the beta group feeding the 1.031 MeV state was first forbidden unique, one would expect a log $f_1 t$ value of 8.2; this value is significantly smaller than the 9.1 value found from our data. This result favors a non-unique first

forbidden interpretation of the beta group and leads to a $(p_{3/2})^{-1}$ assignment to the ^{89}Rb ground state. This assumption is strongly supported by other arguments to be given below.

The beta rays populating the 2.277, 3.225 and 3.500 MeV levels have log $f_o t$ values of 6.0, 5.0 and 5.8 respectively, characteristic of allowed transitions. Negative parity is therefore assigned to these levels. An examination of the intensities of the gamma ray depopulating these levels leads to fairly secure spin assignments.

The 0.277 MeV and 1.246 MeV transitions from the 2.277 MeV state have the relative intensities expected for E1 transitions. The spectrum of coincidences with 0.949 MeV radiation can be used to set an upper limit of 0.4% on the intensity of the 2.277 MeV ground state transition. This limit is a factor of 1000 times smaller than the intensity one would expect from an E1 ground state transition. One concludes, therefore, that the 2.277 MeV level is a (1/2-) state.

The 3.225 MeV negative parity state is depopulated by transitions to the $d_{3/2}$ and $s_{1/2}$ states. From Ge(Li) detector spectra one can set an upper limit for the intensity of the 3.225 MeV transition of 0.2%. This is a factor of 400 times weaker than can be expected for one E1 transition to the $d_{5/2}$ ground state. From this result one may conclude that the 3.225 MeV level is a (1/2-) state. This conclusion is also arrived at from the angular correlation data.

The 3.500 MeV level shows a 3% transition to the $d_{5/2}$ ground state. The spectrum in coincidence with the 1.031 MeV gamma ray can be used to set an upper limit of 0.1% for the intensity of

the transition from the 3.500 MeV level to the 1.031 MeV level. This is a factor of 10 less intense than one might expect for an E1 transition to this level. This suggests the 3.500 MeV is a (5/2-) state, but a choice of (3/2-)) is not ruled out.

The log $f_o t$ value for the transition to the 2.567 MeV level is 6.7 and therefore does not permit one to draw conclusions concerning the parity of this state. The pattern of γ ray intensities to the ground (12%), 1.031 MeV (3%) and 2.000 MeV ($<$ 0.1%) states is consistent with that expected for dipole radiation. This suggests a spin of 3/2 for the 2.567 MeV level. The angular correlation data provides additional evidence for the correctness of this assumption.

The log $f_o t$ value for the transition to the 2.708 MeV level is 6.7. The pattern of intensities to the ground (3%) and 1.031 MeV ($<$ 0.5%) states is about what one would expect for dipole radiation and indicates that the 2.708 MeV level has a spin of 3/2 or 5/2 and unknown parity. The log $f_o t$ value for beta rays feeding the 2.770 MeV state is greater than 7.5, indicating that this level has positive parity. The only transition observed from this state is the weak 0.770 MeV gamma ray of intensity 0.4% feeding the 2.000 ($d_{3/2}$) MeV state. The transitions to the ground and 1.031 MeV states are unobserved, with upper limits of 0.15% and 0.5% respectively, established on the basis of solid state and coincidence measurements. No conclusions concerning the spin is possible from these observations.

Although only the ground state spin of 5/2 in the 3.225 $\rightarrow$ 2.567 $\rightarrow$ 0 MeV cascade is clearly established the angular correlation data implies the spins of the other two levels as 1/2

and 3/2 respectively. All of the possible cascades which are consistent with the beta decay data are shown in Figure 33.* The (1/2, 3/2, 5/2) choice is the only one that fits the data; the next closest being the (5/2, 3/2, 5/2) sequence which must be rejected since its A_2' coefficient is 0.01, about three standard deviations away from the measured value of 0.044. The 1/2- spin assignment to the 3.225 MeV level coupled with the log $f_o t$ value of 5.0 for the beta group feeding this level is conclusive evidence for the $(p_{3/2})^{-1}$ assignment to the ground state of $^{89}_{37}Rb_{52}$.

---

* These cascades are for pure dipole transitions; and no account has been taken of mixed decay modes. The angular correlation data are regarded as corroborating evidence for the spin assignments.

CHAPTER VII

THE DECAY OF ^{89}Kr

a Introduction

The gamma rays emitted in the depopulation of the excited states of ^{89}Rb were studied with Ge(Li) and NaI(Tℓ) detectors while the beta radiations populating these states were examined by use of a plastic detector. Both γ-γ and β-γ coincidence measurements were used in the elucidation of the decay scheme of ^{89}Kr.

b Ge(Li) Detector Measurements

The gamma ray spectrum of ^{89}Kr was studied with several Ge(Li) detectors including a 6 cc "wrap around", a 3 mm R.C.A. and a 4 mm N.D. detector. The pulses were amplified by a Tennelec Model TC 200 amplifier and stored in a 1024 multi-channel analyser. The spectrum was studied in three sections, 0 - 0.7 MeV, 0 - 1.9 MeV, and 0 - 5 MeV and typical spectra for these regions are presented in Figures 35 to 38 inclusive. The upper curve of each figure shows the data plotted on a logarithmic scale while the lower graph represents a linear plot. The inserts indicate gamma rays obtained by a stripping procedure from incompletely resolved multiplets. Calibration of the low energy section was achieved by the simultaneous recording of the spectra from standard sources (^{141}Ce, ^{203}Hg, ^{51}Cr, ^{198}Au, ^{64}Cu, ^{137}Cs) with a ^{89}Kr spectrum. A parabolic expression for the gamma ray energies characteristic of the gain and linearity of the detection system, was obtained by means of the standard sources and used to calculate the energies of the ^{89}Kr lines

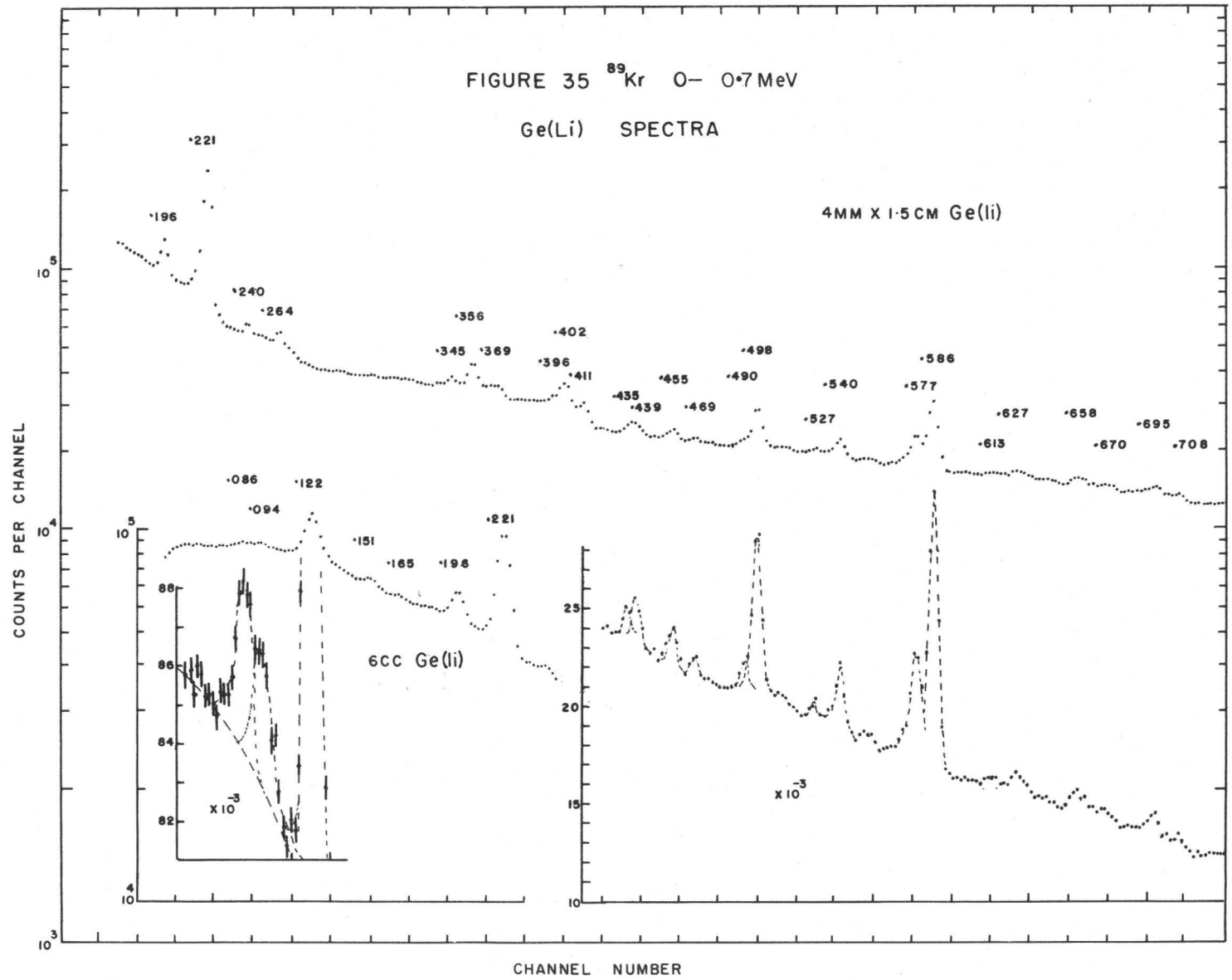
FIGURE 35 ^{89}Kr O– 0·7 MeV
Ge(Li) SPECTRA
4MM X 1·5 CM Ge(li)
6cc Ge(li)
COUNTS PER CHANNEL
CHANNEL NUMBER
·221
·196
·240
·264
·356
·345
·369
·402
·396
·411
·435
·439
·455
·469
·498
·490
·540
·527
·586
·577
·627
·613
·658
·670
·695
·708
·086
·094
·122
·151
·165
·196
·221
x10^{-3}
x10^{-3}

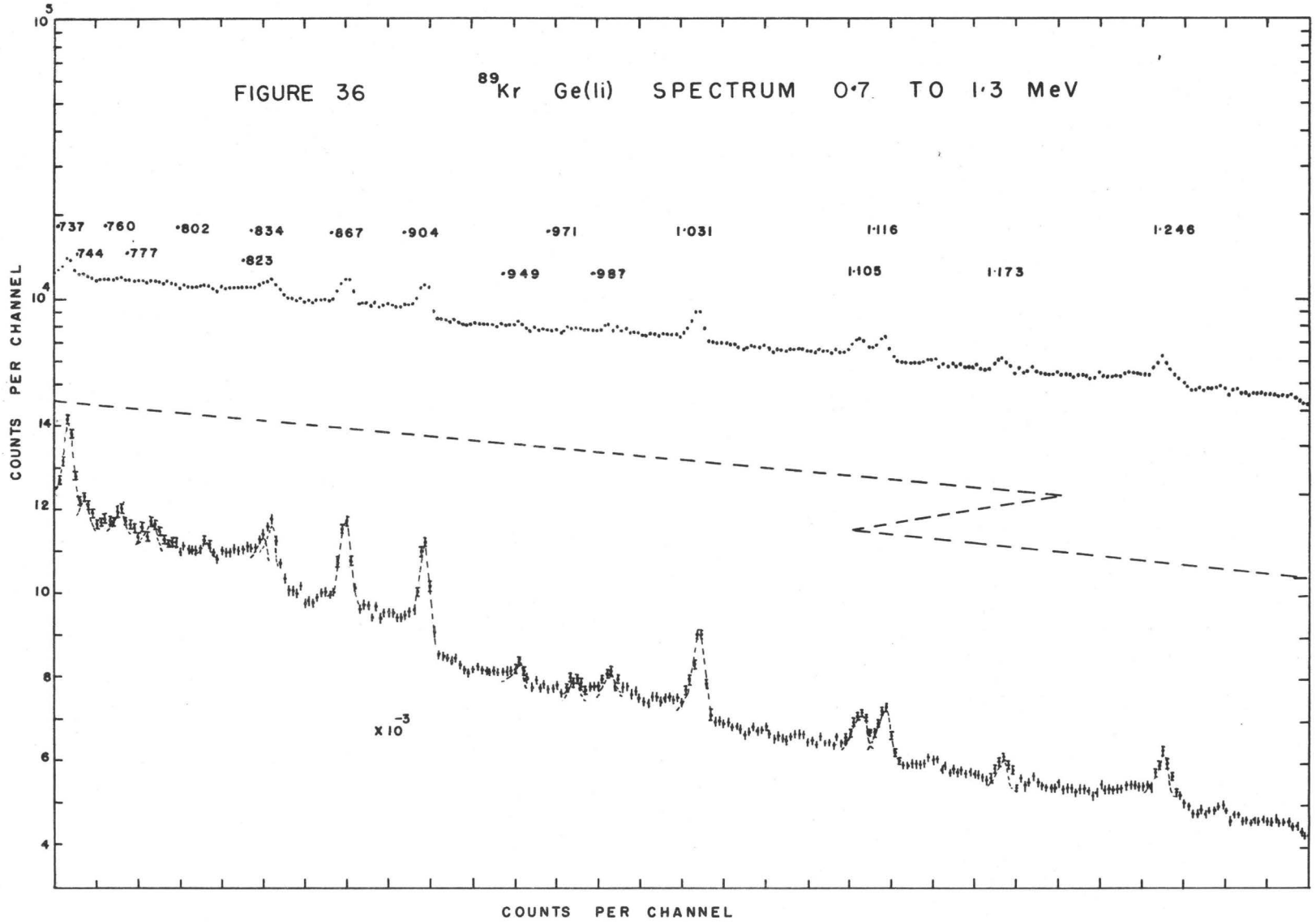
FIGURE 36 ^{89}Kr Ge(li) SPECTRUM 0·7 TO 1·3 MeV
COUNTS PER CHANNEL
COUNTS PER CHANNEL
·737
·744
·760
·777
·802
·823
·834
·867
·904
·949
·971
·987
1·031
1·105
1·116
1·173
1·246
x10^{-3}

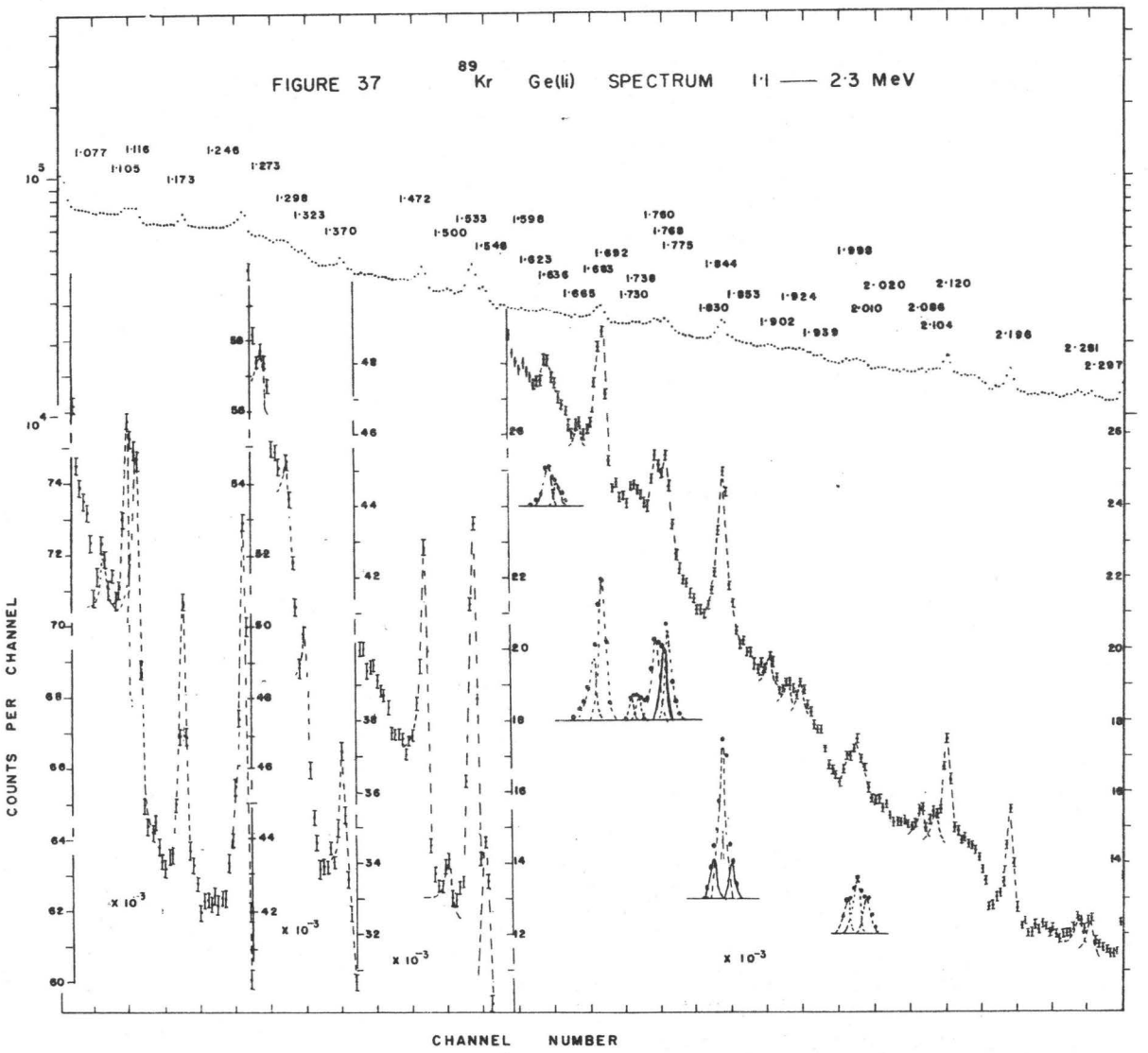
FIGURE 37 89Kr Ge(li) SPECTRUM 1·1 —— 2·3 MeV
1·077
1·105
1·116
1·173
1·246
1·273
1·298
1·323
1·370
1·472
1·500
1·533
1·548
1·598
1·623
1·636
1·665
1·683
1·692
1·730
1·738
1·760
1·768
1·775
1·844
1·902
1·924
1·939
1·998
2·010
2·020
2·086
2·104
2·120
2·196
2·281
2·297
COUNTS PER CHANNEL
CHANNEL NUMBER
x 10⁻³

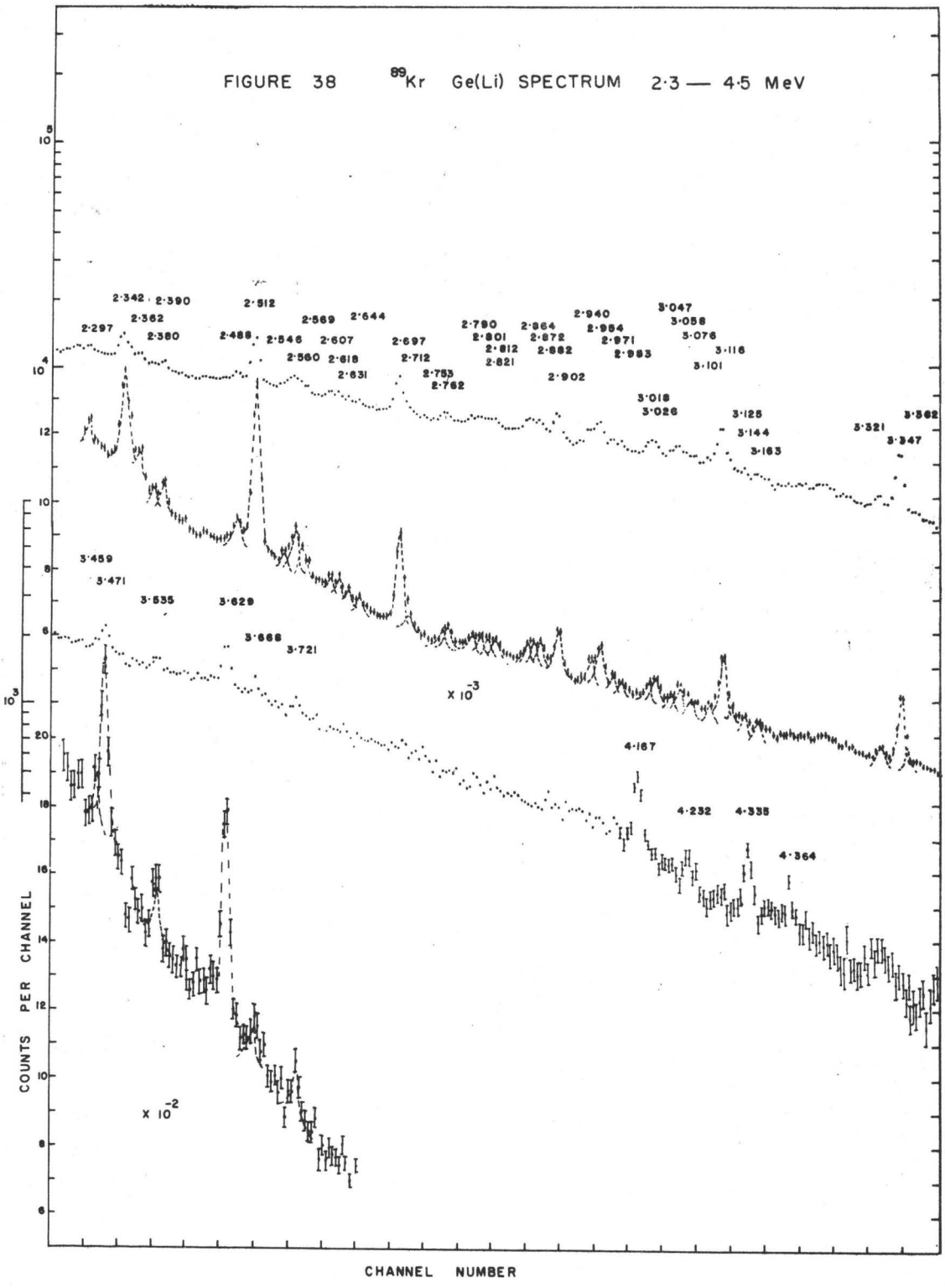
FIGURE 38 ^{89}Kr Ge(Li) SPECTRUM 2·3 — 4·5 MeV
2·297
2·342
2·362
2·380
2·390
2·488
2·512
2·546
2·560
2·569
2·607
2·618
2·631
2·644
2·697
2·712
2·753
2·762
2·780
2·801
2·812
2·821
2·864
2·872
2·882
2·902
2·940
2·954
2·971
2·983
3·018
3·026
3·047
3·058
3·076
3·101
3·116
3·125
3·144
3·163
3·321
3·347
3·362
3·459
3·471
3·535
3·629
3·668
3·721
4·167
4·232
4·335
4·364
x 10^{-3}
x 10^{-2}
COUNTS PER CHANNEL
CHANNEL NUMBER

from 0 to 0.7 MeV. These ^{89}Kr lines were then used as secondary standards for calibration of the mid energy region from 0 to 1.8 MeV. The strong ^{89}Rb lines and a simultaneously recorded ^{24}Na spectrum were used to calibrate the ^{89}Kr lines present in the upper part of this region. The gamma ray peaks and escape peaks of energy greater than 1.8 MeV were measured using the stronger medium energy ^{89}Kr lines plus ^{24}Na and ^{49}Ca calibration lines accumulated before and after the ^{89}Kr runs. Since the ^{49}Ca lines were not known to better than $\sim$ 25 keV, these radiations were separately measured against the photopeaks and escape peak of the well known ^{24}Na[83] lines. The peak-escape peak difference of 1.022 MeV was used as a check on the linearity of the detection system. The energies of the two strong ^{49}Ca lines were found in this way to be 3.084 $\pm$ .002 MeV and 4.072 $\pm$ .002 MeV. The intensities of the ^{89}Kr gamma rays were obtained from either the full energy or second escape peak using an efficiency curve determined experimentally in this laboratory for the 4mm Ge(Li) detector. This curve was determined by comparing the strengths of a number of sources as measured with a 7.6 x 7.6 cm NaI(Tℓ) detector with the strengths found with the Ge(Li) detector and accepting Heath's values[79] for the NaI(Tℓ) detector efficiencies. An independent check of the validity of this efficiency curve was provided by the measurements carried out by other members of this laboratory on the gamma rays from sources of ^{105}Ru and ^{193}Os. The intensities of the gamma rays in these spectra had been measured by external conversion, NaI(Tℓ) detectors and another Ge(Li) detector used at the Chalk River Laboratories.

The four figures show more than 130 peaks, many of which are probably double. Some of these peaks are photo peaks, some are second es-

cape peaks and some are due to contaminants. With the detectors used, the first escape peaks were much too weak to be observed even for the strongest lines in the spectrum. The contaminant lines present are due to the strong transitions in the decay of ^{87}Kr, ^{88}Kr, ^{90}Kr and ^{89}Rb. While it would have been possible to remove the ^{89}Rb component using the water chamber described in Chapter III, the sources produced in this chamber were too weak to obtain satisfactory statistics in a reasonable time with the low efficiency Ge(Li) detectors. The energies and intensities of the ^{89}Rb lines were previously measured by this author (see Chapter VI) while similar information regarding ^{87}Kr and ^{88}Kr was supplied by N. Archer and H. Lycklama of this laboratory [89]. The decay of ^{90}Kr had been studied previously by R. H. Goodman et al [55] and the pertinent information regarding this nuclide was taken from their work. As a further aid in contaminant line identification the spectra of ^{87}Kr, ^{88}Kr and ^{90}Kr were recorded with the same gain as the ^{89}Kr spectra.

All the peaks in Figure 35 are photopeaks with the possible exception of the 0.670 MeV line which may be the second escape peak of the 1.692 MeV radiation. Strong ^{90}Kr lines are in evidence at 0.122, 0.240, 0.490 and 0.540 MeV while ^{88}Kr lines were found at 0.165 and 0.196 MeV and a strong ^{87}Kr line was apparent at 0.402 MeV. The statistical errors in this presentation are smaller than the plotted points on the logarithmic scale, and are about the size of the points shown on the linear graph above .4 MeV. Obviously many of the weak peaks may be multiplets.

The contaminant lines of Figure 36 include the ^{90}Kr line at 1.116

MeV, ^{88}Kr lines at 0.834 and 1.173 MeV and ^{89}Rb lines at 0.949, 1.031, 1.173 and 1.246 MeV. (The portion of this spectrum above 1.100 MeV is also shown in Figure 37 with better statistics). The 0.987 MeV peak is caused by the escape peak of the 2.010 MeV photon.

The high energy spectra of Figures 37 and 38 show a complex array of ^{89}Kr peaks, escape peaks, and contaminant lines. All the lines observed in the spectra are listed in Table 8. Many weak lines are no doubt missed because of the finite resolution of the detector and because of statistical considerations. Above 3.7 MeV little structure is evident. This reflects the rapid decrease of the full energy peak efficiency of the detector, the growing importance of random summing and the contribution of contaminant lines originating in n-γ reactions or background. The four peaks above 4 MeV are second escape peaks associated with these latter effects. These peaks or indeed any radiations of energy greater than 4.7 MeV were not present in spectra accumulated with NaI(Tℓ) detectors inside the "cave" described in Chapter IV.

Column 1 of Table 8 presents the energies of the "lines" observed in spectra of ^{89}Kr. All of the stronger lines were recorded in many runs while the weaker ones were only evident in runs with good statistics and good resolution. The standard deviations quoted in column 2 are weighted means of a number of measurements. The third column presents the absolute intensity of each line on the assumption that it is a full energy peak. Column 5 gives the energy of the gamma ray which would yield a second escape peak of the energy shown in column 1 while column

TABLE 8

Energies and Intensities of Lines Observed in Ge(Li) ^{89}Kr Spectra

Energy of Observed Line E	Estimated $\sigma(E)$	Intensity if a Full Energy Peak I	Estimated $\sigma(I)$	Energy if Observed Line is a 2nd Escape Peak E'	Intensity of Corresponding Full Energy Peak I'	Estimated $\sigma(I')$	Comments
0.0856	.0004	0.45	0.05				
0.0936	.0004	0.37	0.04				
0.1216	.0003	~3.4					^{90}Kr
0.1508	.0005	0.95	0.11				
0.1646	.001	0.25	0.03				^{88}Kr
0.1959	.0003	~3.4					^{88}Kr
0.2206	.0003	25	3.0				
0.2402	.0005	0.68	0.08				^{90}Kr
0.2642	.0005	0.93	0.11				
0.3453	.0003	2.0	0.3				
0.3563	.0003	6.5	0.7				
0.3688	.0009	2.0	0.5				
0.3960	.001	1.5	0.3				
0.4023	.0003	~3.9					
0.4114	.0006	1.50	0.25				
0.4345	.0008	0.50	0.10				
0.4393	.0008	1.25	0.25				
0.4550	.001	1.25	0.13				
0.4687	.0006	0.75	0.08				
0.4900	.005	2.0	0.4				^{90}Kr

(continued)

TABLE 8 (continued)

E	σ(E)	I	σ(I)	E'	I'	σ(I')	Comments
0.4978	.0003	11.3	1.5				
0.5270	.0005	0.5	0.2				
0.5395	.0003	~3.8					^{90}Kr
0.5772	.0003	8.0	1.0				
0.5864	.0003	21	2.5				
0.6130	.0015	0.5	0.2	1.625	3.0	1.0	
0.6270	.0015	1.5	0.3	1.649	9.0	2.0	
0.6580	.0015	~2					^{89}Rb
0.6703	.0015	0.63	0.2	1.692	3.3	1.0	
0.6950	.0015	2.0	0.25	1.717	8.4	0.9	
0.7080	.0015	0.73	0.09	1.730	3.1	0.5	
0.7376	.0008	4.0	0.6	1.760	14.6	2.3	
0.744	.001	0.33	0.04	1.766	1.14	0.15	
0.760	.001	0.50	0.07	1.782	1.7	0.25	
0.777	.001	0.57	0.07	1.799	1.83	0.25	
0.802	.002	0.50	0.30	1.824	1.5	0.9	
0.823	.005	2.0	1.0	1.846	6.0	3.0	
0.834	.002	~3					^{88}Kr
0.8675	.0005	6.0	0.90	1.890	14.4	2.2	
0.9035	.0007	7.3	1.0	1.926	16	2.4	
0.9490	.002	~2.5					^{89}Rb
0.9706	.003	0.38	0.05	1.993	0.63	0.1	
0.9874	.003	0.5	0.07	2.009	0.79	0.12	
1.031	.001	~12.5					^{89}Rb
1.077	.002	0.88	0.10	2.099	1.19	0.13	

(continued)

TABLE 8 (continued)

E	σ(E)	I	σ(I)	E'	I'	σ(I')	Comments
1.1053	.0010	5.4	0.7	2.127	6.34	1.1	
1.1165	.001	6.25	0.75	2.139	6.38	1.2	^{90}Kr(60%), ^{89}Kr(20%)
1.173	.001	5.0	0.70	2.195	5.25	1.1	^{88}Kr+^{89}Rb (80%), ^{89}Kr(20%)
1.246	.001	~ 9					^{89}Rb
1.273	.002	0.34	0.06	2.295	0.27	0.04	
1.298	.002	0.53	0.10	2.320	0.4	0.08	
1.324	.0015	1.60	0.40	2.346	1.12	0.3	
1.370	.001	5.6	1.2	2.392	3.45	0.8	^{88}Kr(50%), ^{89}Kr(50%)
1.4721	.0006	9.5	1.5	2.49	4.95	0.8	
1.500	.002	0.79	0.16	2.522	0.38	0.08	
1.5334	.0010	16.6	2.5	2.556	7.8	1.2	^{90}Kr+^{88}Kr+ ^{87}Kr(30%), ^{89}Kr(70%)
1.548	.003	4.3	0.8	2.570	1.9	0.4	^{89}Rb
1.596	.003	1.0	0.2	2.618	0.41	0.08	
1.623	.002	2.3	0.5	2.645	0.80	0.16	
1.636	.002	0.95	0.2	2.658	0.33	0.07	
1.665	.002	0.68	0.14	2.687	0.23	0.04	
1.681	.005	2.00	0.4	2.703	0.75	0.15	^{89}Rb
1.6916	.0006	4.75	0.8	2.714	1.70	0.40	
1.730	.002	0.75	0.16	2.752	0.24	0.05	
1.738	.002	0.75	0.15	2.760	0.24	0.05	

(continued)

TABLE 8 (continued)

E	σ(E)	I	σ(I)	E'	I'	σ(I')	Comments
1.760	.002	3.0	0.6	2.782	0.93	0.25	
1.768	.002	2.5	0.5	2.790	0.77	0.150	
1.775	.002	3.75	0.7	2.797	1.5	0.3	^{90}Kr (15%), ^{89}Kr (85%)
1.830	.005	1.50	0.3	2.852	0.41	0.08	
1.8435	.001	9.0	1.5	2.866	2.40	0.5	
1.853	.002	1.25	0.25	2.875	0.34	0.05	
1.902	.001	1.25	0.25	2.924	0.30	0.05	
1.924	.003	1.25	0.25	2.946	0.29	0.05	
1.939	.003	1.25	0.25	2.961	0.28	0.05	
1.998	.002	1.4	0.28	3.020	0.30	0.05	^{89}Rb (75%)
2.011	.002	2.58	0.5	3.033	0.52	0.10	
2.020	.002	1.70	0.34	3.042	0.34	0.06	
2.086	.002	1.05	0.20	3.108	0.19	0.04	
2.104	.002	0.88	0.17	3.126	0.16	0.03	
2.120	.002	5.25	1.1	3.142	0.89	0.20	
2.1965	.0015	7.50	1.5	3.219	1.13	0.22	^{89}Rb+^{88}Kr (60%), ^{89}Kr (40%)
2.281	.002	1.95	0.40	3.303	0.2	0.05	
2.297	.002	1.95	0.40	3.319	0.25	0.05	
2.342	.002	11.25	1.6	3.364	1.30	0.25	
2.362	.002	2.25	0.4	3.384	0.25	0.05	
2.380	.003	0.40	0.08	3.402	0.047	0.008	
2.390	.002	1.80	0.36	3.412	0.20	0.04	^{88}Kr

(continued)

TABLE 8 (continued)

E	σ(E)	I	σ(I)	E'	I'	σ(I')	Comments
2.488	.002	3.0	0.6	3.510	0.28	0.06	
2.512	.001	17.25	3.0	3.534	1.54	0.30	
2.546	.002	0.75	0.15	3.568	0.085	0.02	
2.560	.002	3.50	0.7	3.582	0.30	0.06	^{87}Kr(50%), ^{89}Kr(50%)
2.569	.003	2.50	0.5	3.591	0.21	0.04	^{89}Rb(100%)
2.607	.002	1.00	0.20	3.629	0.077	0.015	
2.618	.002	1.40	0.28	3.640	0.108	0.02	
2.631	.002	0.88	0.16	3.653	0.07	0.015	
2.644	.002	0.70	0.14	3.666	0.06	0.001	
2.698	.0015	10.75	1.50	3.720	0.73	0.14	^{89}Rb(4%)
2.712	.002	1.75	0.35	3.734	0.17	0.03	
2.753	.002	0.63	0.12	3.775	0.040	0.008	
2.762	.002	1.43	0.28	3.784	0.085	0.017	
2.790	.003	1.50	0.30	3.812	0.083	0.016	
2.801	.003	1.50	0.30	3.823	0.083	0.016	
2.812	.003	1.50	0.30	3.834	0.083	0.016	
2.821	.003	1.50	0.30	3.843	0.083	0.016	
2.864	.003	3.00	0.60	3.886	0.14	0.028	
2.872	.002	3.00	0.60	3.894	0.14	0.028	
2.882	.003	3.00	0.60	3.904	0.14	0.028	
2.902	.002	6.50	1.30	3.924	0.31	0.06	
2.940	.002	3.80	0.76	3.962	0.16	0.03	
2.954	.002	6.10	1.20	3.976	0.26	0.05	
2.971	.002	2.70	0.54	3.993	0.13	0.03	

(continued)

TABLE 8 (continued)

E	σ(E)	I	σ(I)	E'	I'	σ(I')	Comments
2.983	.002	1.75	0.35	4.005	0.073	0.014	
3.018	.003	1.50	0.30	4.040	0.061	0.012	
3.026	.003	2.25	0.44	4.048	0.092	0.018	
3.047	.005	1.18	0.23	4.069	0.043	0.009	
3.058	.002	3.50	0.70	4.080	0.13	0.025	
3.076	.005	1.50	0.30	4.098	0.044	0.01	
3.101	.005	1.43	0.28	4.123	0.048	0.01	
3.116	.003	9.75	1.70	4.138	0.34	0.07	
3.125	.005	1.50	0.30	4.147	0.051	0.01	
3.144	.005	1.0	0.20	4.166	0.028	0.005	
3.163	.005	1.0	0.20	4.185	0.028	0.005	
3.321	.003	2.10	0.42	4.343	0.052	0.010	
3.347	.003	12.0	2.40	4.369	0.29	0.06	
3.362	.003	1.0	0.20	4.384	0.027	0.006	
3.459	.003	0.40	0.08	4.481	0.0075	0.0015	
3.471	.003	4.30	0.86	4.493	0.06	0.012	
3.535	.003	1.10	0.22	4.557	0.017	0.004	
3.629	.003	3.60	0.72	4.651	0.054	0.012	
3.668	.003	0.40	0.08	4.690	0.006	0.0015	
3.721	.003	0.80	0.16	4.743	0.011	0.002	
4.167	.005	2.10	0.42	5.189	0.022	0.005	Contaminant
4.232	.005	0.60	0.12	5.254	0.006	0.002	Contaminant
4.335	.005	1.00	0.20	5.357	0.010	0.003	Contaminant
4.364	.005	0.25	0.05	5.386	0.0025	0.0008	Contaminant

6 indicates its intensity. The last column is reserved for comments on the origin or analysis of the peaks.

The ratio of the observed areas of the full energy peak to the second escape peak is crudely approximated by $r = A \exp(-kE)$ for gamma ray energies from $\sim$ 1.7 to 5 MeV where A and k take the values of 1.77, 1.5/MeV and 0.77, 0.85/MeV for the 4 mm and 6 cc detectors used in this work. Thus a comparison of the photon areas associated with the peaks of the same energy recorded by the two detectors can often yield unambiguous assignments of the origin of the peaks. A second means of distinguishing the origin of the peak is afforded by a comparison of the intensity of a peak at energy E with the peaks observed at $E + 2m_oc^2$ and $E - 2m_oc^2$. For weak peaks, it is unlikely that both the escape and full energy peaks will have been recorded. Under these circumstances, one must rely on NaI(Tℓ) spectra (see Figure 39), or on γ-γ coincidence data. Finally for some very weak lines, the decision has been made on which gamma ray fits into the decay scheme. Even after exhausting these methods of identification, the origins of some of the weak lines remain unknown.

Table 9 presents the energies of the observed ^{89}Kr gamma rays together with their relative intensities. The standard deviations shown in columns 2 and 4 reflect the number of measurements and the strength of the peaks. The sixth column indicates the classification of the gamma ray in the decay scheme to be presented in Figure 46. The final column indicates the difference between the energies predicted from the decay scheme and those measured.

TABLE 9

^{89}Kr Gamma Rays

Photon Energy E	Estimated σ(E)	Photon Intensity I	Estimated σ(I)	Method of Detection	Position in Decay Scheme	E Calculated -E Observed keV
0.0856	.0004	0.45	0.05	Ge		
0.0936	.0004	0.37	0.04	Ge		
0.1508	.0005	0.95	0.11	Ge NaI		
0.2206	.0003	25	3.0	Ge NaI γ-γ	0.221 → 0	0
0.2642	.0005	0.93	0.11	Ge		
0.3453	.0003	2.0	0.3	Ge		
0.3563	.0003	6.5	0.7	Ge NaI γ-γ	0.577 → 0.221	+ .15
0.3688	.0009	2.0	0.5	Ge γ-γ	1.692 → 1.324	- .4
0.396	.001	1.5	0.3	Ge		
0.4114	.0006	1.50	0.25	Ge γ-γ	0.997 → 0.586	- .3
0.4345	.0008	0.50	0.10	Ge		
0.4393	.0008	1.25	0.25	Ge		
0.455	.001	1.25	0.13	Ge		
0.4687	.0006	0.75	0.08	Ge γ-γ	2.161 → 1.692	+ .5
0.4978	.0003	11.3	1.5	Ge NaI γ-γ	0.498 → 0	0
0.527	.005	0.5	0.2	Ge		
0.5772	.0003	8.0	1.0	Ge NaI γ-γ	0.577 → 0	0
0.5864	.0003	21.0	2.5	Ge NaI γ-γ	0.586 → 0	0
0.613	.0015	0.5	0.2	Ge		
0.627	.0015	1.5	0.3	Ge γ-γ	2.161 → 1.533	+ .8
0.695	.0015	2.0	0.25	Ge NaI γ-γ	1.692 → 0.997	+ .2
0.708	.0015	0.73	0.09	Ge γ-γ	2.400 → 1.692	+ .2
0.7376	.0018	4.0	0.6	Ge NaI γ-γ	1.324 → 0.586	+ .3
0.744	.001	0.33	0.04	Ge		
0.760	.001	0.50	0.07	Ge		
0.777	.001	0.57	0.007	Ge γ-γ	0.997 → 0.221	.1
0.802	.002	0.50	0.30	Ge		
0.823	.005	2.0	1.0	Ge γ-γ	1.324 → 0.498	+3.0
0.860	.015	0.3	0.1	γ-γ	4.224 → 3.364	0
0.8675	.0005	6.0	0.90	Ge NaI γ-γ	2.400 → 1.533	- .5
0.9035	.0007	7.3	1.0	Ge NaI γ-γ	2.596 → 1.692	+ .6

(continued)

TABLE 9 (continued)

Photon Energy MeV	Estimated σ(E)	Photon Intensity I	Estimated σ(I)	Method of Detection	Position in Decay Scheme	E Calculated -E Observed keV
0.970	.003	0.38	0.05	Ge		
1.010	.030	1.1	0.40	γ-γ	1.533→0.498	
1.077	.002	0.88	0.10	Ge γ-γ	2.400→1.324	- .6
1.1053	.0010	5.4	0.7	Ge NaI γ-γ	1.692→0.586	+ .4
1.1165	.001	2.5	0.5	Ge NaI γ-γ	1.692→0.577	-1.5
1.173	.001	1.25	0.5	Ge γ-γ	2.866→1.692	+ .6
1.273	.002	0.34	.06	Ge γ-γ	2.596→1.324	+ .5
1.298	.002	0.53	0.10	Ge		
1.324	.0015	1.60	0.40	Ge NaI γ-γ	1.324→ 0	0
1.370	.001	2.8	0.5	Ge	1.370→ 0	0
1.4721	.0006	9.5	1.5	Ge NaI γ-γ	1.692→0.498	+ .6
1.500	.002	0.79	0.16	Ge γ-γ	1.998→0.498	+ .3
1.5334	.001	11.3	2.0	Ge NaI γ-γ	1.533→ 0	+ .1
1.636	.002	0.95	0.2	Ge		
1.665	.002	0.68	0.14	Ge γ-γ	2.161→0.498	-1.4
1.670	.030	1.1	0.4	γ-γ	3.364→1.692	
1.6916	.0006	4.75	0.8	Ge NaI γ-γ	1.692→ 0	+ .5
1.760	.002	3.0	0.6	Ge	1.760→ 0	0
1.775	.002	2.75	0.6	Ge γ-γ	1.998→ .221	+2.4
1.8435	.001	1.1	0.4	Ge γ-γ	3.535→1.692	-1.1
1.902	.001	1.25	0.25	Ge NaI γ-γ	2.400→0.498	+ .6
1.998	.002	0.4	0.2	Ge	1.998→ 0	0
2.010	.002	2.58	0.5	Ge NaI γ-γ	2.596→0.586	- .2
2.020	.002	1.70	0.34	Ge NaI γ-γ	2.596→0.577	- .9
2.120	.002	1.0	0.3	Ge γ-γ	2.618→0.498	+ .3
2.281	.002	1.95	0.40	Ge γ-γ	2.866→ .586	- .17
2.380	.003	0.40	0.08	Ge γ-γ	2.596→ .221	-4.4
2.618	.002	1.38	0.3	Ge	2.618→ 0	0
2.6445	.003	0.78	0.15	Ge γ-γ	2.866→0.221	
2.753	.002	0.63	0.12	Ge		
2.761	.001	1.43	0.28	Ge		
2.790	.002	1.50	0.30	Ge NaI γ-γ	3.364→0.577	-2.7

(continued)

TABLE 9 (Continued)

Photon Energy MeV	Estimated σ(E)	Photon Intensity I	Estimated σ(I)	Method of Detection	Position in Decay Scheme	E Calculated -E Observed keV
2.8657	.002	.40	0.1	Ge NaI γ-γ	3.364 → 0.498	+1.0
2.8657	.002	2.0	0.4	Ge NaI	2.866 → 0	0
2.946	.003	0.29	0.05	Ge γ-γ	3.535 → 0.586	+2.1
3.125	.003	0.16	0.03	Ge		
3.143	.002	0.88	0.20	Ge NaI γ-γ	3.720 → 0.577	0
3.219	.002	0.38	0.07	Ge NaI γ-γ	3.720 → 0.498	+3.3
3.303	.002	0.25	0.05	Ge		
3.320	.002	0.25	0.05	Ge γ-γ	3.905 → 0.586	-1.4
3.363	.002	1.25	0.25	Ge NaI	3.364 → 0	+1.4
3.384	.002	0.25	0.05	Ge	3.961 → .577	0
3.480	.030	0.28	0.10	Ge γ-γ	3.976 → 0.498	-2.
3.510	.002	0.28	0.06	Ge	3.733 → 0.221	+1.9
3.5345	.001	1.54	0.30	Ge NaI	3.535 → 0	0
3.568	.002	0.85	0.02	Ge	4.145 → 0.577	- .1
3.629	.002	.075	0.015	Ge		
3.653	.002	.07	0.015	Ge		
3.720	.0015	0.73	0.014	Ge NaI	3.720 → 0	
3.734	.002	0.17	0.03	Ge	3.733 → 0	0
3.823	.003	0.083	0.016	Ge		
3.834	.003	0.083	0.016	Ge		
3.843	.003	0.083	0.016	Ge γ-γ	4.342 → 0.498	+1.3
3.894	.002	0.14	0.028	Ge	4.481 → 0.586	+ .6
3.904	.003	?		Ge	4.481 → 0.577	- .1
3.904	.003	0.14	0.028	Ge	3.905 → 0	-1.0
3.924	.002	0.31	0.03	Ge NaI γ-γ	4.145 → 0.221	0
3.962	.002	?		Ge	3.961 → 0	-1.0
3.962	.002	0.16	0.03	Ge	4.184 → 0.221	+ 1.0
3.976	.002	0.26	0.05	Ge	3.976 → 0	0
3.993	.002	0.13	0.03	Ge	4.492 → 0.498	+1.3
4.005	.002	0.078	0.014	Ge		
4.040	.003	0.061	0.012	Ge	4.626 → 0.586	- .7
4.048	.003	0.092	0.018	Ge	4.626 → 0.577	+ .6
4.069	.005	0.043	0.009	Ge	4.649 → 0.577	+2.4

(continued)

TABLE 9 (continued)

Photon Energy MeV	Estimated σ(E)	Photon Intensity	Estimated σ(I)	Method of Detection	Position in Decay Scheme	E Calculated -E Observed keV
4.080	.002	0.13	0.03	Ge	4.080 → 0	0
4.098	.005	0.054	0.01	Ge		
4.123	.005	0.048	.010	Ge		
4.138	.002	0.34	0.07	Ge NaI	4.138 → 0	0
4.147	.005	0.051	0.010	Ge γ-γ	4.368 → .221	+ .7
4.185	.005	0.028	0.005	Ge	4.184 → 0	-1.0
4.343	.003	0.052	0.010	Ge	4.342 → 0	-1.0
4.369	.003	0.29	0.06	Ge	4.368 → 0	- .7
4.481	.003	0.008	0.002	Ge	4.481 → 0	0
4.493	.003	0.06	0.012	Ge	4.492 → 0	-1.0
4.651	.003	0.054	0.012	Ge	4.649 → 0	-2.5
4.690	.003	0.006	0.0012	Ge	4.690 → 0	0

E	σ(E)	I	Unclassified Lines			I'	σ(I')
			σ(I)	or	E'		
1.830	.005	1.50	0.3		2.852	0.41	0.08
1.853	.002	1.25	0.25		2.875	0.34	0.06
1.939	.003	1.25	0.25		2.961	0.28	0.06
2.086	.002	1.05	0.20		3.108	0.20	0.04
2.560	.002	1.75	0.30		3.583	0.3	0.15

The following paragraphs comment on the interpretation and origin of a number of peaks presented in Figures 35 to 38 and in Tables 8 and 9. The peak at 0.83 MeV of Figure 36 is composed of the Compton edge of the 1.031 MeV gamma ray of ^{89}Rb, the strong 0.834 MeV contaminant from ^{88}Kr and a 0.823 MeV radiation from ^{89}Kr. There may also be a trace of the 0.846 MeV ^{87}Kr line. The 0.823 MeV line represents about one third of the total peak and shows up in the γ-γ coincidence experiments to be described. The 1.116 MeV peak is about 60% due to ^{90}Kr and 40% due to ^{89}Kr. The ^{89}Kr fraction was established by γ-γ coincidence experiments and from simple subtraction of the calculated contaminant contribution. The second escape peaks of the 2.195 MeV ^{89}Rb and the 2.196 MeV ^{88}Kr gamma rays account for the observed intensity of the 1.173 MeV peak. A weak photon, however, is observed in γ-γ coincidence measurements at this energy and therefore a fraction ($\sim \frac{1}{4}$ deduced from γ-γ coincidence data) is believed to originate in the decay of ^{89}Kr. Only this portion is listed in Table 9.

Approximately half of the 1.370 MeV peak in Figure 37 arises from the second escape peak of the 2.392 MeV ^{88}Kr radiation; the remaining 50% is ascribed to a 1.370 MeV ^{89}Kr gamma ray. The strong 1.533 MeV peak is composed of the second escape peak of the 2.557 MeV ^{87}Kr radiation, and the full energy peak of the 1.531 MeV ^{88}Kr and 1.54 MeV ^{90}Kr gamma rays. These contaminants account for about 30% of the observed intensity; the remainder is a strong ^{89}Kr photon.

The observed triplet at 1.77 MeV includes a contribution originat-

ing in the decay of ^{90}Kr. By recalculating the decay scheme of Goodman et al on the basis of ^{90}Kr lines observed as contaminants in the ^{89}Kr spectra it is possible to deduce this line has energy 1.777 MeV and an intensity of ~ 25% of the observed 1.775 MeV line. From γ-γ coincidence data, on the other hand, one deduces this contaminant must be 40% of the observed line.

About 60% of the 2.196 MeV peak is associated with the full energy peak of the 2.195 and 2.196 MeV contaminants lines discussed above. The remaining 40% is associated with the second escape peak of a 3.219 MeV ^{89}Kr radiation whose presence is confirmed in γ-γ coincidence studies.

Half of the intensity of the peak at 2.560 MeV in Figure 38 is due to the 2.557 MeV ^{87}Kr line while the remainder is associated with the second escape peak of a 3.582 MeV ^{89}Kr radiation. There are a number of other peaks which include traces (a few percent) of known contaminant lines and allowances have been made for these as is indicated in the fourth column of Table 8.

In this spectrum of radiations from ^{89}Kr there are undoubtedly many cases of unresolved multiplets and of overlaps between the full energy peaks of one gamma ray and the second escape peaks of another. Only a few of these have been uniquely identified by the γ-γ coincidence studies. One such case is the peak at 2.120 MeV, 20% of whose intensity is associated with the full energy peak, while the remainder is created by the second escape peak from a 3.142 MeV ^{89}Kr line.

c γ-γ Coincidence Measurements

The γ-γ coincidence experiments were performed with two 7.6 x 7.6 cm NaI(Tl) detectors using the circuitry outlined in Figure 14 of Chapter IV. The source holder was the water chamber described in Chapter III. Sources of ^{89}Kr prepared with this chamber showed no trace of ^{89}Rb daughter activity in either a Ge(Li) spectra or the NaI(Tl) coincidence spectra.

Figure 39 presents an ^{89}Kr singles spectrum recorded with the sum-coincidence circuit outlined in Figure 17 of Chapter IV. It is evident from this spectrum that most of the stronger peaks contain several gamma rays. A comparison of this spectrum with those of Figures 35 to 38 indicates the degree of difficulty that would have been faced if one had to depend on NaI(Tl) spectra alone. The contributions of random and coincidence summing to the singles spectrum is also shown in this figure. Although such distortional effects occur in the coincidence spectra they are serious only in the interpretation of weak events.

Figures 40 and 41 present a sequence of γ-γ coincidence spectra recorded with narrow windows placed over the 0.221, 0.356, 0.498 and 0.577 + 0.586 MeV gamma rays present in the ^{89}Kr spectrum. Analysis of these and other spectra reveal that the 0.221 MeV radiation is in coincidence with gamma rays of energy 0.356, 0.695, 0.777, 0.903, 1.116, 1.472, 1.775, 2.020, 2.380, 2.644, 2.790, 3.143, 3.924 and 4.147 MeV. The other radiations present in the spectrum are accounted for by Compton distributions of higher energy gamma rays present in the window or are weak photons whose origin is discussed below. A window placed on the 0.196 MeV ^{88}Kr photo peak demonstrated by its spectrum of coincidence gamma rays (not

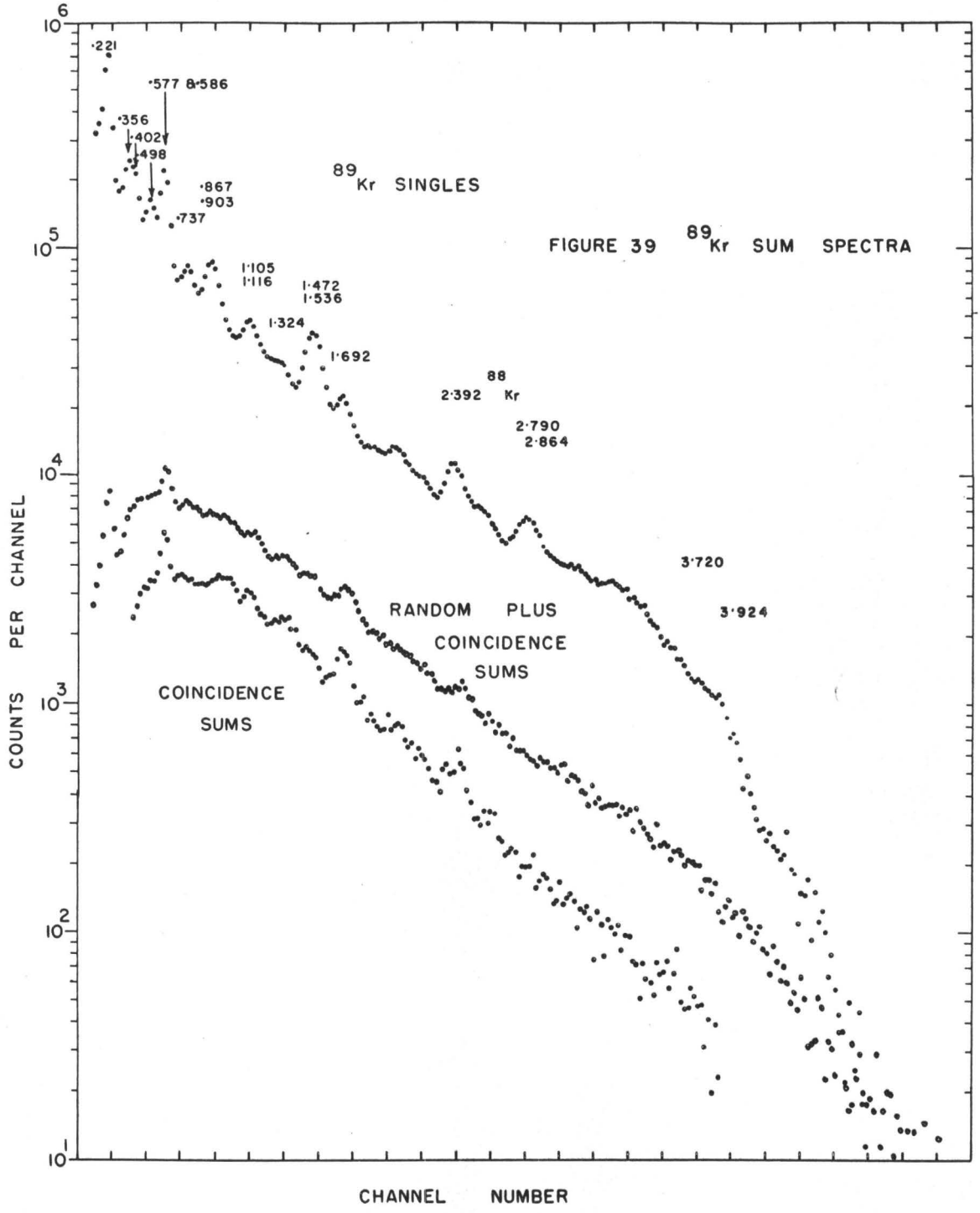

FIGURE 39 ^{89}Kr SUM SPECTRA

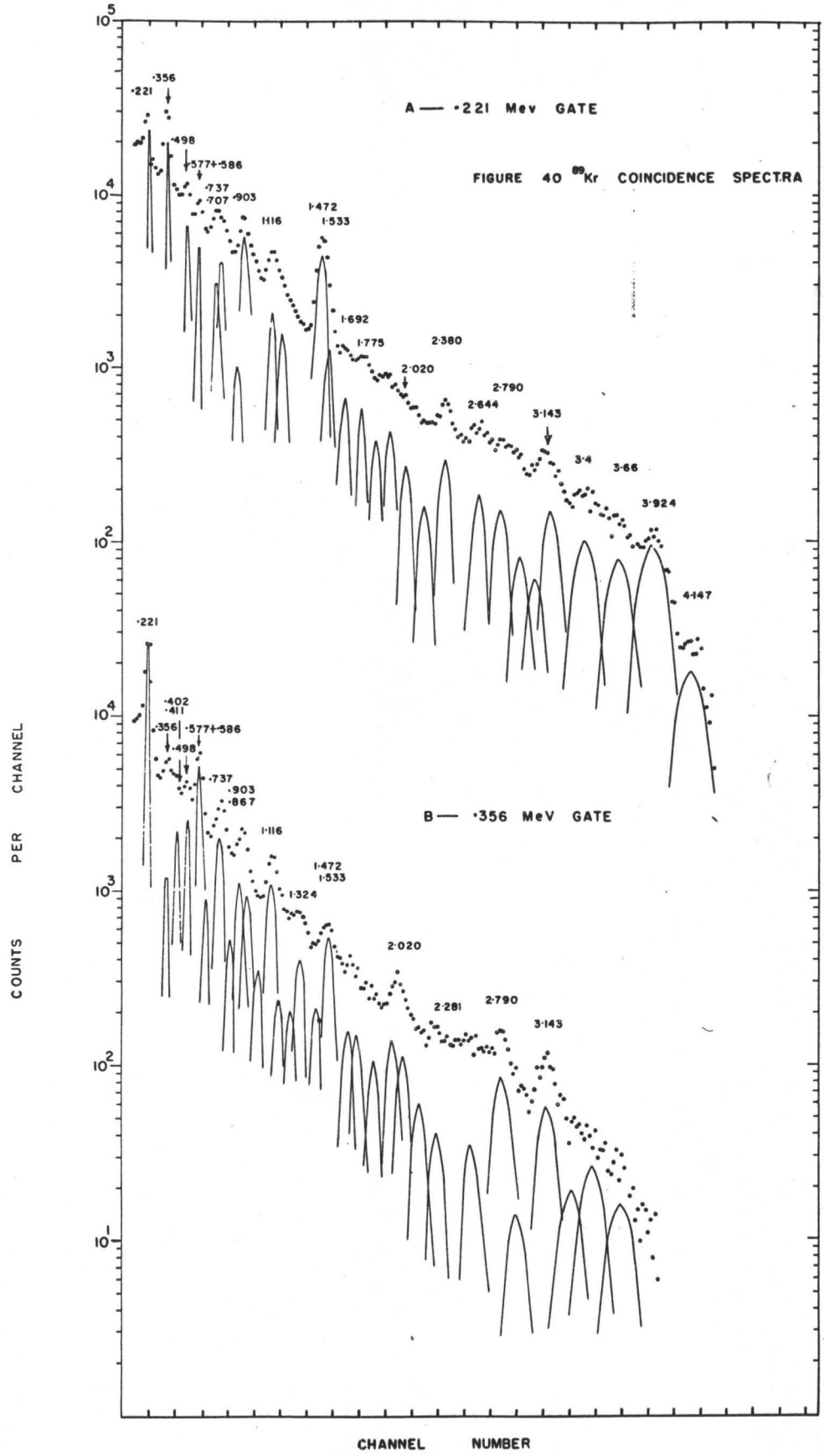

FIGURE 40 ^{89}Kr COINCIDENCE SPECTRA

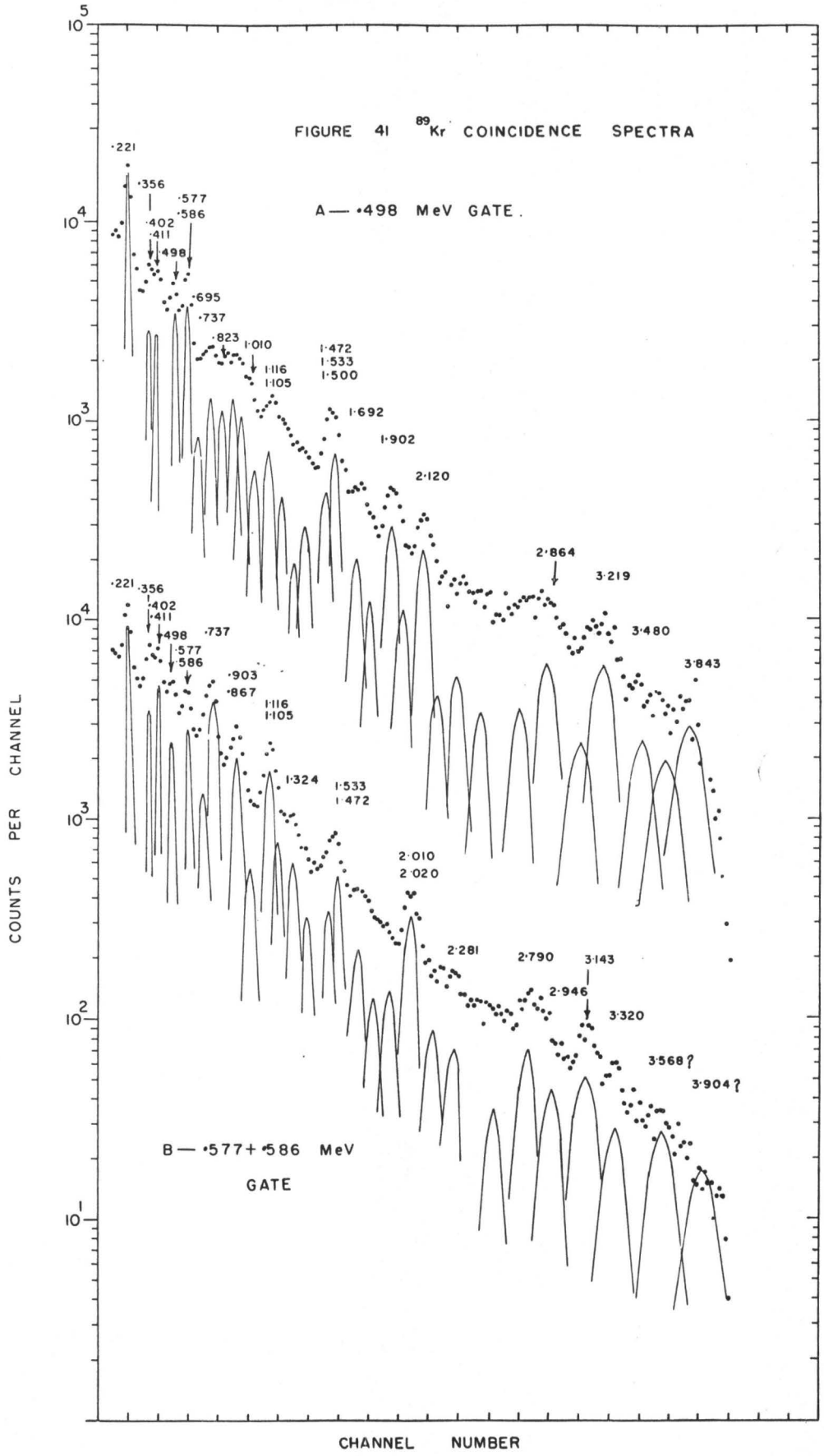
FIGURE 41 ^{89}Kr COINCIDENCE SPECTRA
A — ·498 MeV GATE.
B — ·577 + ·586 MeV GATE
·221
·356
·402
·411
·498
·577
·586
·695
·737
·823
1·010
1·116
1·105
1·472
1·533
1·500
1·692
1·902
2·120
2·864
3·219
3·480
3·843
·903
·867
1·324
1·533
1·472
2·010
2·020
2·281
2·790
3·143
2·946
3·320
3·568?
3·904?
COUNTS PER CHANNEL
CHANNEL NUMBER

shown) that the 0.221 MeV window was devoid of this contaminant and in particular that the 0.221-2.380 MeV coincidences originate in ^{89}Kr. (There is a very strong 2.390 MeV line in ^{88}Kr which appears in the singles spectrum).

The 0.356 radiation is in coincidence with gamma rays of energy 0.221, 1.116, 2.020, 2.780 and 3.143 MeV while a window placed on the 0.498 MeV radiation reveals coincidences with the 0.823, 1.010, 1.500, 1.902, 2.120, 2.865, 3.219 and 3.480 MeV photons. Finally, the spectrum of radiations in coincidence with the (0.577+0.586) MeV window include the 0.369, 0.411, 0.695, 0.7376, 0.803, 1.077, 1.105, 1.116, 1.273, 2.010, 2.020, 2.790, 2.946, 3.143 and 3.320 MeV gamma rays.

In both Figures 40 and 41 there are a number of gamma rays which have not been assigned an energy value. This has been done both for purposes of clarity in presentation and because the origin of some of these weak lines is uncertain. In the present decay scheme many gamma ray doubles and triplets occur which are not resolved in NaI(Tl) spectra and which appear as a single broadened peak in the coincidence spectra. The model functions and the reduction techniques used in the analysis are not adequate to meet such situations* with the result that weak peaks situated near strong lines may be "created" in the analysis. Moreover, since the γ-γ coincidence technique offers an order of magnitude increase in sensitivity over the Ge(Li) spectra, a large number of real but weak gamma transitions will appear in the coincidence spectra which were missed in the Ge(Li) studies. There is no way of distinguishing these real photons from the "analysis-created" ones. Hence, the policy has been adopted of

---

* Additional distortions result from Bremstraulung, random and coincidence summing, etc.

not including a gamma ray in the decay scheme unless it was observed in the germanium spectrum. This rule has been broken in a few cases which involved "clean" experiments or which involved relatively intense peaks in the coincidence spectrum.

It is evident from figures 40 and 41 that the spectra of coincidence gamma rays taken with these windows show a large number of coincidence photons of high energy thus leading one to postulate that these radiations are associated with the lowest lying levels. An analysis reveals that levels exist at 0.221, 0.498, 0.577 and 0.586 MeV while the 0.356 MeV radiation is a stopover transition from the 0.577 to 0.221 MeV levels. Thus the difference between the spectra in coincidence with the 0.356 MeV and 0.577 + 0.586 MeV windows gives information concerning transitions to the 0.586 MeV level. These four well established levels at 0.221, 0.498, 0.577 and 0.586 MeV provide a secure base for the determination of higher lying excited states.

The existence of levels at 2.596 and 1.692 MeV is based on a set of strong coincidence pairs evident from the previous list. The 0.221-1.472 MeV and 0.221-0.903 MeV coincidences result from a triple cascade originating in the 2.596 MeV level and proceeding by the 2.596 → 1.692 → 0.221 → 0 MeV levels. Transitions from the 2.596 MeV level to the 0.221, 0.577 and 0.586 MeV levels occur via 2.380, 2.020 and 2.010 MeV photons. A similar set of coincidence photons occurs from the 1.692 MeV level in the form of 1.105 - 0.586 MeV and 1.116 - 0.577 MeV coincidence pairs. In addition, the 1.692 MeV level depopulates by a strong ground state transition. Both the 2.596 and 1.692 MeV levels are strongly supported

in many ways by evidence to be discussed below.

A level at 1.324 MeV is defined by virtue of strong 0.586-0.7376 MeV and weaker 0.498 - 0.823 MeV coincidence pairs.

A level at 0.997 MeV is established as a stopover in the 0.695 - 0.411 - 0.586 MeV cascade which involves the well established 0.586 MeV and 1.692 MeV levels. The order of this cascade was determined through the existence of a weak 0.777 - 0.221 MeV coincidence pair.

The existence of gamma rays of energy 1.500, 1.902 and 2.120 MeV in coincidence with the 0.498 MeV window establishes levels at 1.998, 2.400 and 2.618 MeV respectively. Ground state transitions from the 1.998 and 2.618 MeV levels plus a 1.775 - 0.221 MeV coincidence pair securely establish two of these levels while clear evidence for the 2.400 MeV level will be demonstrated below.

An examination of Figures 40 and 41 reveal a number of high energy transitions populating the levels at 0.221, 0.498, 0.577 and 0.586 MeV. A 2.644 - 0.221 MeV coincidence cascade is evidence for a level at 2.865 MeV. Part of the intensity of a strong 2.865 MeV photon observed in Ge(Li) spectra is due to a ground state transition from this level. The remaining fraction of the intensity is associated with a weaker 2.865 MeV gamma ray which is in coincidence with the strong 0.498 MeV photon. This latter cascade originates in a 3.364 MeV level which also depopulates by a 2.790 MeV photon to the 0.577 MeV level and an intense ground state transition. A weak 2.946 - 0.586 MeV coincidence pair plus a 3.534 MeV ground state transition is deemed evidence for a 3.534 MeV level. The observed cascading pairs of photons of energy

3.143 - 0.221, 3.143 - 0.356, 3.143 - 0.577 and 3.219 - 0.498 MeV leads one to postulate a level at 3.720 MeV. This level depopulates by a direct ground state transition in addition to the other modes listed. A set of coincidence pairs of energy 3.321 - 0.586, 3.480 - 0.498, 3.924 - 0.221, 3.840 - 0.498 and 4.147 - 0.221 MeV define levels at 3.905, 3.976, 4.145, 4.371 and 4.369 MeV. These levels also depopulate by direct ground state transitions.

The coincidence spectra presented in Figures 42 and 43 add support to the levels defined above and provide evidence for several others. The first of these presented in Figures 42A and B represents the spectrum of coincidence gamma rays observed with the 0.7376 and 0.695 MeV windows. These spectra clearly demonstrate the 0.695 - 0.411 MeV and 0.737 - 0.586 MeV coincidence pairs observed previously. No photon of energy 0.7 MeV is known to exist in ^{87}Kr and therefore the possibility that the former pair is an 0.7 - 0.402 MeV coincidence cascade arising from the ^{87}Kr contaminant is excluded. Weak gamma rays of energy 1.273 and 1.077 MeV are observed in coincidence with the 0.737 MeV window which are the 2.596 $\rightarrow$ 1.324 MeV and 2.618 $\rightarrow$ 1.324 MeV transitions. The remaining photons labelled in these spectra are accounted for by Compton distributions of other gamma rays in the gates with intensities consistent with the proposed decay scheme.

Sections C and D of Figure 42 present the coincidence spectra observed with windows placed on the 0.903 and 0.867 MeV photons respectively. These data clearly reveal a strong 0.867 - 1.533 MeV coincidence pair which is created by the 0.867 MeV transition from the 2.400 MeV level to

FIGURE 42 ^{89}Kr COINCIDENCE SPECTRA

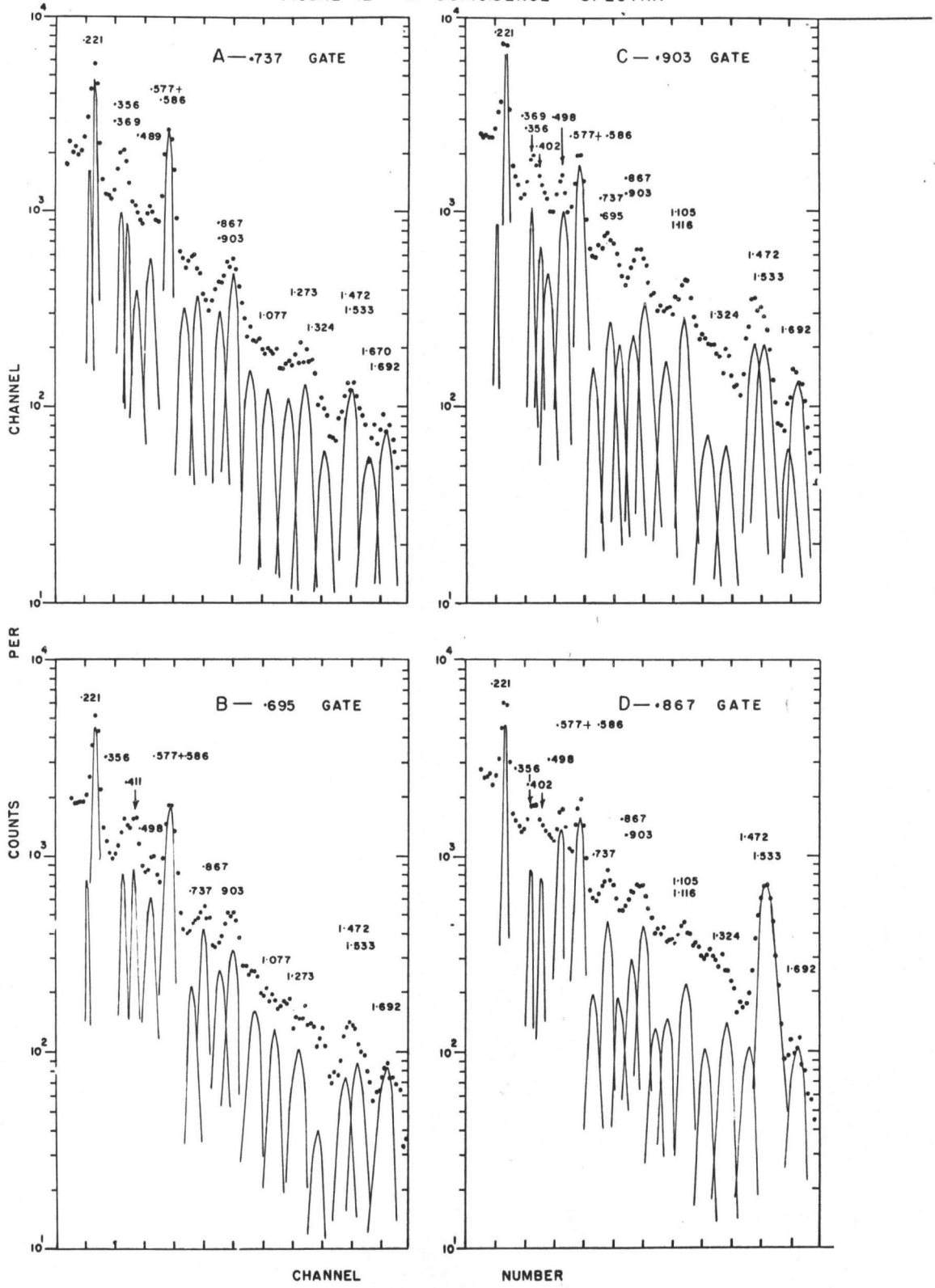

the 1.533 MeV level. A weak 1.010 - 0.498 MeV coincidence cascade was previously noted; this is due to a 1.010 MeV transition from the 1.533 MeV to the 0.498 MeV levels. It is clear from the spectrum of gamma rays observed with a 0.903 MeV window that this radiation is strongly in coincidence with photons of energy 1.692, 1.472, 1.105, 1.116, 0.695, 0.411, 0.369 and 0.221 MeV. These coincidences confirm the levels at 2.596, 1.692, 0.997, 0.586, 0.577 and 0.221 MeV. In these spectra both the 0.867 and 0.903 MeV windows contain large amounts of 0.903 and 0.867 MeV radiations in their windows respectively, in addition to Compton distributions of higher energy photons. These contributions to the gates account for other coincidence gamma rays observed in the spectra.

Complimentary to the 0.867 and 0.903 MeV coincidence experiments are the reverse experiments with windows on the 1.533 and 1.472 MeV photons. The results of these runs are presented in Figures 43E and 43F respectively. These data confirm the previous interpretation of the levels and firmly establish the existence of the 1.500 - 0.498 coincidence cascade originating in the 1.998 MeV level. Coincidences observed with the 1.472 MeV radiation in addition reveal weak photons of energy 0.469, 1.173, 1.670 and 1.844 MeV thus confirming the levels at 2.865, 3.364 and 3.533 MeV and defining a level at 2.161 MeV. Further evidence for these transitions is given by the 1.692 and 1.100 MeV windows, while proof for the 2.161 MeV level is given by a weak 0.627 - 1.533 MeV coincidence pair. Spectrum C of Figure 43 shows the portion of the singles spectrum corresponding to the coincidence spectra of the same figure. It is included merely to assist the reader in interpreting the spectra of Figures

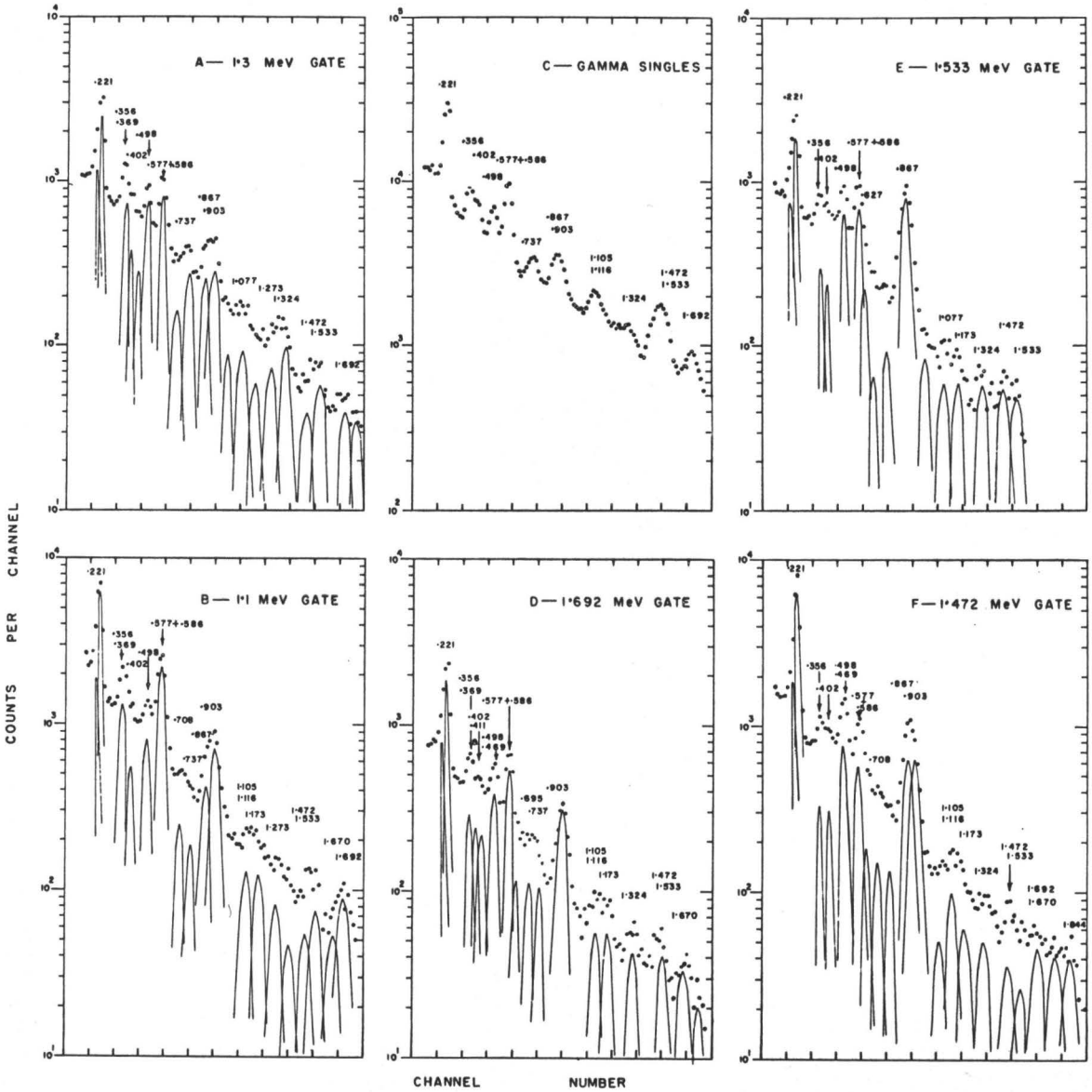

FIGURE 43 ^{89}Kr COINCIDENCE SPECTRA

42 and 43.

Section D of Figure 43 presents the spectrum of coincidence gamma rays recorded with a window placed on the 1.692 MeV peak. An analysis of this spectrum reveals coincidence gamma rays of energy 0.469, 0.903, 1.173 and 1.670 MeV which were previously identified as transitions from the 2.161, 2.596, 2.865 and 3.364 MeV levels. The presence of the 1.324, 1.472 and 1.692 MeV peaks in this spectrum is a result of the contribution of the 1.670 MeV gamma ray to the gate.

The spectrum of coincidence gamma rays recorded with windows on the 1.324 MeV and (1.105 + 1.116) MeV radiations is presented in sections A and B of Figure 43. The 1.324 MeV coincidence spectrum reveals peaks at 0.369, 1.274 and 1.077 MeV corresponding to coincidence cascades involving levels at 1.692 $\rightarrow$ 1.324, 2.596 $\rightarrow$ 1.324 and 2.400 $\rightarrow$ 1.324 MeV respectively. These data confirm the location of these transitions in the decay scheme as established by other coincidence experiments. The appearance of strong 1.1 - 0.221, 1.1 -(0.577 + 0.586), 1.1 - 0.903, 1.1 - 1.173, 1.1 - 1.670 and 1.173 - 1.692 MeV coincidence pairs as seen in the figure is that expected on the basis of the levels already defined.

Figure 44 presents typical coincidence spectra accumulated for windows placed on high energy photons. It was found that a marked similarity occurred between the coincidence spectra recorded for all windows from 1.7 to 4 MeV with only slight shifts in the relative intensities of the 0.221, 0.356, 0.498, 0.577 and 0.586 MeV photons being observed as the window position was shifted. These observations reflect the abundance of weak high energy gamma rays which feed the lowest lying levels.

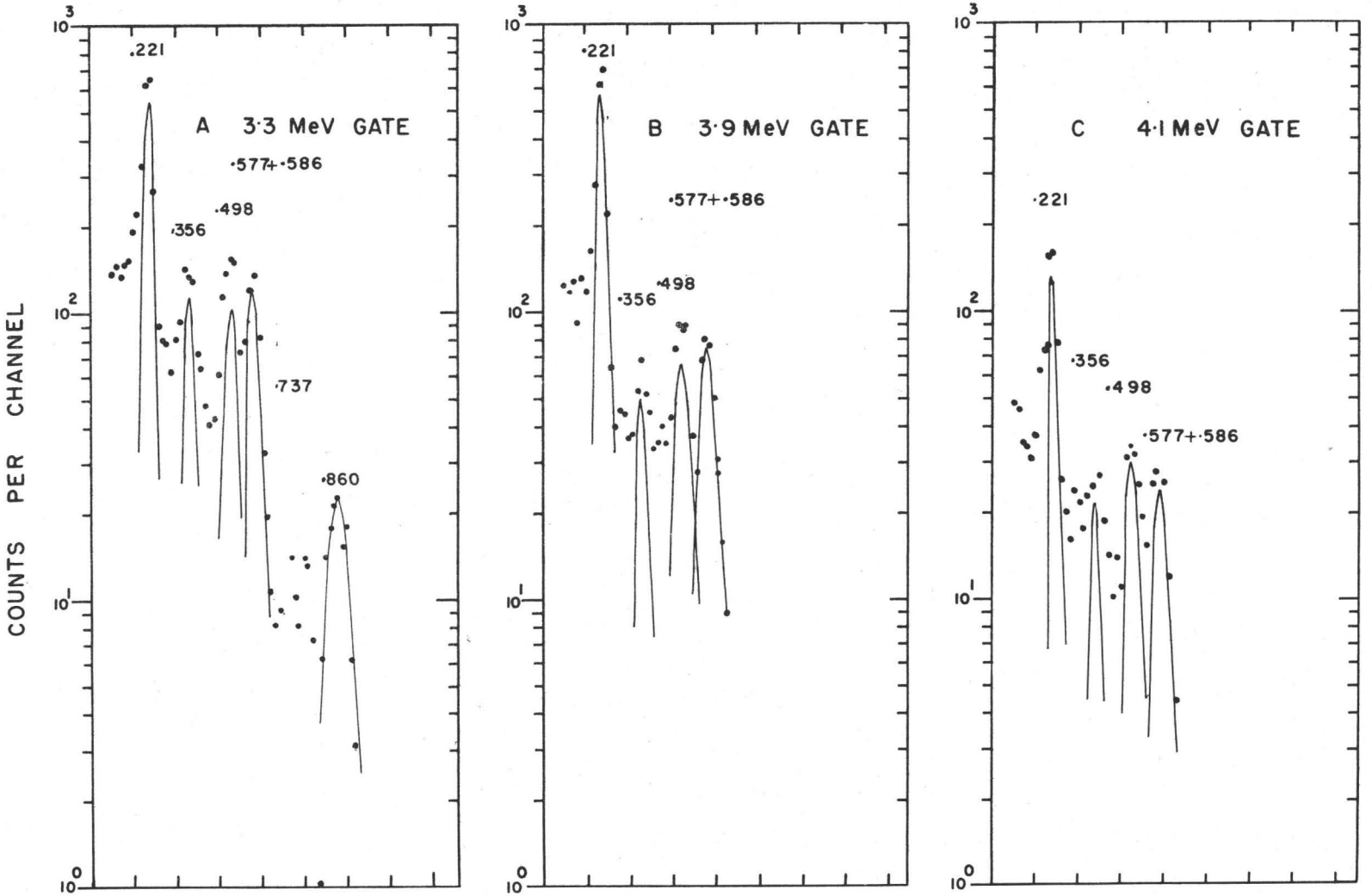

FIGURE 44 ^{89}Kr COINCIDENCE SPECTRA

An exception to this general observation is the spectrum in coincidence with the 3.3 MeV window (Section A of Figure 44) which revealed an 0.86 MeV coincidence peak. This coincidence photon disappeared for higher energy gates but was still weakly present for windows of slightly lower energy. When the window was shifted to the 2.7 - 2.8 MeV region this photon again appeared strongly. This pattern of events is explained by a 0.86 MeV photon populating the 3.364 MeV level from a level at $\sim 4.224 \pm .020$ MeV.

d Coincidence Quotients

Two sets of coincidence data comprising approximately 30 spectra each were reduced to component gamma rays by means of the non-linear least squares fitting procedure outlined in Chapter V. From these data and from the number of events falling in each window a translation into coincidence quotients was carried out. This translation made use of analysed singles spectra, from which the fractional window content was obtained, and computed NaI(Tl) efficiency curves for the geometry used (see Chapter V). In making these calculations, it was assumed to a first approximation that the actual physical size of the water chamber was equivalent to a line source $\simeq 5$ cm in length placed 5.3 cm from the detector face. A computed efficiency* curve for such an arrangement was found to deviate by 2% at 0.2 MeV from the curve presented in Chapter V. This deviation vanished for higher energy photons.

Table 10 presents measured coincidence quotients for each coincidence pair. Column 1 indicates the gate, column 2 the coincident photon,

---

* Programmed by Mr. J. Mason of this laboratory.

TABLE 10

^{89}Kr Coincidence Quotients

Gated Photon MeV	Coincidence Photon MeV	Experimental Q_{ij}	Computed Q_{ij}	Comments
0.221	0.356	0.25	0.26	
	0.695	0.02	0.023	
	0.777	0.015	0.023	
	0.903	0.06	~0.11	
	1.116	0.03	0.041	
	1.472	0.46	0.38	
	1.775	0.07	0.11	
	2.020	0.033	0.031	
	2.380	0.028	0.015	
	2.644	0.035	0.028	
	2.790	0.033	0.026	
	3.143	0.03	0.018	
	3.924	0.034	0.012	
	4.147	0.0038	0.0021	
0.356	0.221	1.03	1.0	
	1.116	0.18	0.17	
	2.020	0.12	0.12	
	2.790	0.09	0.1	
	3.143	0.033	0.07	
0.369	0.737	0.32	0.53	Gate content uncertain because of intense 0.356
	0.903	0.41	0.28	
	1.324	0.14	0.2	
0.411	0.695	~.96	1.0	
0.498	0.823	0.13	0.18	
	1.010	0.096		Observed in γ-γ only
	1.500	0.083	0.06	
	1.902	0.096	0.11	
	2.120	0.089		Masked by other photons in Ge spectra
	2.865	0.036		
	3.219	0.057	0.033	
	3.480	0.024		Observed in γ-γ only
	3.843	0.004	0.007	
0.577	1.116	0.16	0.17	
	2.020	0.074	0.012	
	2.790	0.15	0.1	
	3.143	0.075	0.07	
0.586	0.369	0.064	~0.005	Weak coincidence photon
	0.411	0.042	0.07	
	0.695	0.10	0.05	
	0.737	0.23	0.19	
	0.903	~0	~0.002	

TABLE 10 (continued)

^{89}Kr Coincidence Quotients

Gated Photon MeV	Coincidence Photon MeV	Experimental Q_{ij}	Computed Q_{ij}	Comments
	1.077	0.02	0.021	Masked by 1.105
	1.105	0.25	0.25	
	1.273	~ 0	.009	
	2.010	0.08	0.13	
	2.281	0.033	0.093	
	2.946	0.021	0.012	
	3.321	0.024	0.010	
0.695	0.411	~.14	0.72	Gate content uncertain because of strong 0.737 photon
	0.586	~.4	0.72	
	0.777	~.1	0.28	
	0.903	~.14	0.076	
0.737	0.369	~.22	0.25	Gate content uncertain because of other unresolved photons
	0.586	1.09	1.0	
	1.077	~.17	0.11	
	1.273	.12	0.045	
0.777	0.695	~1	1.0	Gate content uncertain
0.867	1.533	~1	0.90	
0.903	0.221	0.44	0.36	
	0.356	0.04	0.042	
	0.369	0.061	0.075	
	0.577	0.042	0.047	
	0.586	0.21	~0.25	
	0.695	0.005	0.076	
	0.737	0.06	0.004	
	0.823	0.06	0.02	
	1.105	0.15	0.21	
	1.116	0.07	0.09	
	1.324	0.05	~0.015	Weak coincidence photon
	1.472	0.27	0.36	
	1.692	0.19	0.18	
1.077	0.737	~ 0.3	0.55	Weak Gated photon
	1.324	~ 0.13	0.2	
1.105	0.586	0.91	1.0	
	0.903	0.26	0.28	
	1.670	0.1		Observed in γ-γ only
1.116	0.221	0.68	0.45	
	0.356	0.41	0.45	
	0.577	0.50	0.55	
	0.903	0.26	0.28	
	1.670	0.1		Observed in γ-γ only
1.273	1.324	0.42	0.4	Weak gated photon

TABLE 10 (continued)

^{89}Kr Coincidence Quotients

Gated Photon MeV	Coincidence Photon MeV	Experimental Q_{ij}	Computed Q_{ij}	Comments
1.324	0.369	0.04	0.21	Weak gated
	0.903	0.2	0.7	photon
	1.077	0.14	0.11	
	1.273	0.07	0.045	
1.472	0.221	1.22	1.0	
	0.903	0.23	0.28	
	1.173	0.05		Observed in
	1.843	0.042		γ-γ only
1.500	0.498	~.6	1.0	Gate content uncertain
1.533	0.867	0.53	0.49	
1.692	0.708	0.03	0.028	
	0.903	0.25	0.28	
	1.173	0.05		Observed in
	1.670	0.055		γ-γ only
1.902	0.498	~.97	1.0	Gate content uncertain
2.010	0.586	~.6	1	
2.020	0.356	~.35	0.45	
	0.577	~.34	0.55	
2.120	0.498	~1	1	

column 3 the measured coincidence quotient and the fourth column the quotient predicted from the decay scheme. The final column is reserved for comments. Since most of the peaks in the NaI(Tl) spectra of ^{89}Kr occur as unresolved multiplets, the calculation of the coincidence quotients proved to be difficult, and agreement between measured and expected quotients within a factor of two is considered to be good. For high energy transitions the number of gamma rays present in the window makes a reliable estimate of the fractional gate content impossible. The analysis of these coincidence experiments was therefore carried out in another way which made use of the following approximate equation.

$$N_i \approx N_o (\omega\epsilon)_i \, (\underline{\omega\epsilon})_{jo} \sum_j F_j \lambda_j Q_{ij} \qquad (1)$$

In this expression N_o is the source strength, N_i is the number of observed coincidences of gamma ray i with the gate centered on an energy jo, while $(\omega\epsilon)_i$ and $(\underline{\omega\epsilon})_{jo}$ refer to the solid angle efficiency factors appropriate to energies i and jo. F_j, λ_j and Q_{ij} are the computed fractional gamma ray content in the window, the absolute intensity of the gated photon, and the coincidence quotients Q_{ij}.

Transposing (1) yields

$$\frac{N_i}{N_o (\omega\varepsilon)_i \, (\underline{\omega\epsilon})_{jo}} \approx \sum_j F_j \lambda_j Q_{ij} \qquad (2)$$

By comparing the experimentally determined left member with the computed right member of equation (2) one may establish the presence of coincidence makers in the gate.

All of the coincidence spectra associated with the high energy gates show prominent peaks at 0.221, 0.356, 0.498 and 0.577 + 0.586 MeV

with intensities which vary with gate position. Since it has already been well established that there are strongly populated levels at 0.221, 0.498, 0.577 and 0.586 MeV, it is clear that the 0.356 MeV peak arises from the depopulation of the 0.577 MeV level and that part of the 0.221 MeV coincidence photon is due to γ - 0.356 - 0.221 MeV cascades. The observed $\frac{N_i}{N_o(\omega\epsilon)_{0.221}(\omega\epsilon)_{jo}}$ ratio for the 0.221 MeV peak was therefore corrected for this effect by subtracting the ratio associated with the 0.356 MeV peak. Since the 0.356 and 0.577 MeV transitions both originate in the same level, the relative intensities of these gamma rays were used to obtain a scaling factor which was applied to the $\frac{N_i}{N_o(\omega\epsilon)_{.356}(\omega\epsilon)_{jo}}$ value to get a $\frac{N_i}{N_o(\omega\epsilon)_{.577}(\omega\epsilon)_{jo}}$ ratio. This value was then subtracted from the value for the 0.577 + 0.586 MeV peak to get a $\frac{N_i}{N_o(\omega\epsilon)_{0.586}(\omega\epsilon)_{jo}}$ value for the gamma rays feeding the 0.586 MeV level.

Table 11 compares the experimentally determined values of $\frac{N_i}{N_o(\omega\epsilon)_i(\omega\epsilon)_{jo}}$ with the values of $\sum_j F_j \lambda_j Q_{ij}$ computed by projecting out of the list of gamma rays known to be in the window (see Table 9) those photons which were consistant with the data and the reverse experiments. Section A compares these numbers for the 0.221 MeV peak appearing in coincidence experiments using windows in the range 4.1 to 2.1 MeV, while sections B, C and D treat the 0.356, 0.498 and 0.586 MeV coincidence photons respectively. Column 1 of this table indicates the nominal gating energy while columns 2 and 3 present the two sides of equation 2. The gamma rays used in the calculations are listed as column headings while the computed value of $F_j \lambda_j Q_{ij}$ for the individual photons in each window

TABLE 11

Coincidence Relationships for High Energy Gated Photons

A - 0.221 MeV Coincidence Radiation

Nominal Gate Energy	$\frac{N_i}{N_o \left(\frac{\omega\epsilon}{}\right)_j (\omega\epsilon)_i}$ x 10^{-2}	$\sum_j F_j \lambda_j Q_{ij}$ x 10^{-2}	$F_j \lambda_j Q_{ij}$ for Preferred Gated Coincidence Makers x 10^{-2}					
			4.147	3.962	3.924	3.510	2.645	2.380
4.1	1.6	1.41	0.58	0.37	0.46			
3.9	8.0	5.3	0.3	1.7	3.3			
3.8	5.3	5.6	0.3	1.7	3.6			
3.75	5.5	3.68	0.4	0.92	2.0	0.36		
3.6	6.0	5.6	0.5	1.1	2.2	1.8		
3.4	7.0	6.55	0.25	1.2	2.5	2.6		
3.3	10	5.3	0.31	1.1	2.2	1.7		
3.0	7	4.23	0.13	0.8	1.6	1.7		
2.8	8	3.81	0.11	0.6	1.2	1.9		
2.7	6	10.4	0.12	0.4	0.9	1.3	7.7	
2.6	30	18.6	0.19	0.7	1.5	2.2	14	
2.4	34	34.1	0.40	1.5	3.0	4.5	17	7.7
2.2	21	12.2	0.15	0.6	1.1	1.2	7.6	1.5
2.1	13	12.4	0.14	0.5	1.0	1.1	6.7	3.0

B - 0.356 MeV Coincidence Radiation

			4.064	4.048	3.568	3.384	3.143	2.740	2.020
3.9	0.7	0.48	0.14	0.34					
3.8	0.84	0.50	0.15	0.35					
3.75	1.9	0.85	0.25	0.5	0.1				
3.5	1.9	1.4	0.3	0.7	0.4				
3.4	3.6	1.89	0.12	0.27	0.25	1.25			
3.3	9.8	5.9	0.2	0.3	0.3	0.7	4.4		
3.0	5.9	6.4	0.05	0.15	0.4	0.5	5.3		
2.8	3.8	4.49	~ 0	0.09	0.3	0.7	1.9	1.5	
2.7	8.8	9.76	0.05	0.11	0.2	0.9	2.5	6.0	
2.6	14	12.5	0.1	0.2	0.4	0.8	6.0	5.0	
2.4	16	28.0	0.1	0.3	0.6	2.0	8.0	17.0	
2.2	9.9	14.2	0.05	0.14	0.2	0.7	2.3	7.0	3.8
2.1	13	24.4	0.05	0.1	0.2	0.5	3.0	4.5	16

TABLE II (cont'd)

Coincidence Relationships for High Energy Gated Photons

* C - 0.498 MeV Coincidence Radiation

Nominal Gate Energy	$\frac{N_i}{N_o\left(\frac{\omega\epsilon}{}\right)_j(\omega\epsilon)_i}$ x 10^{-2}	$\sum_j F_j\lambda_j Q_{ij}$ x 10^{-2}	$F_j\lambda_j Q_{ij}$ for Preferred Gated Coincidence Makers x 10^{-2}						
			3.993	3.843	3.480	3.219	2.866	2.120	1.902
3.9	2.5	1.23	1.23						
3.8	3.8	2.1	1.21	0.9					
3.75	3.9	2.66	1.53	0.73	0.4				
3.5	3.9	2.7	0.9	0.5	1.3				
3.4	3.6	5.22	1.1	0.7	3.15	0.27			
3.3	7.2	8.2	1.0	0.7	1.5	5.0			
3.0	6.7	5.9	0.8	0.4	1.5	3.2			
2.8	9.8	8.5	0.4	0.3	1.9	1.5	4.4		
2.7	8.7	5.85	0.35	0.3	1.4	2.19	1.6		
2.6	21	10.5	0.6	0.4	2.2	4.8	2.5		
2.4	25	22.4	1.1	0.8	3.6	8.0	8.4	.5	
2.2	20	24.9	0.4	0.3	1.2	2.4	2.5	18.0	
2.1	27	18.4	0.4	0.3	1.1	2.3	2.4	7.0	4.9

* Uncertain because of annihilation radiation

D - 0.586 MeV Coincidence Radiation

			4.040	3.894	3.320	2.846	2.281	2.010
3.9	3.0	1.95	0.45	1.4				
3.8	3.6	2.4	0.7	1.7				
3.75	3.5	1.46	0.72	0.74				
3.5	4.0	1.94	0.93	0.98	0.03			
3.4	7.0	2.96	0.36	1.1	1.5			
3.3	15	4.1	0.5	1.1	2.5			
3.0	10	1.78	0.18	0.5	0.9	0.2		
2.8	6	4.67	0.12	0.55	1.0	3.0		
2.7	16	4.05	0.15	0.4	2.3	1.2		
2.6	24	8.65	0.2	0.7	2.8	3.0	1.95	
2.4	26	35.2	0.5	1.3	5.2	5.2	23	
2.2	17	24.9	0.2	0.5	1.7	1.6	12	9
2.1	40	68.2	0.2	0.5	1.5	1.5	14.5	50

are indicated in the column below. A window with no entry for a $F_j \lambda_j Q_{ij}$ under a particular photon simply means this photon was not present in the gate. In view of the discussion above it will be evident that the ratios quoted in Table 11 include only the effect of gamma rays directly feeding the 0.221, 0.498, 0.577 and 0.586 MeV levels respectively.

It was found in this analysis that a number of weak photons had to be included as coincidence makers in order to achieve reasonable agreement with the data. These photons would normally be masked in the reverse experiments and therefore not directly detected. Similarly the analysis showed that a number of gamma rays were of such intensity that they had to be ground state transitions.

As can be seen from Table 11, the agreement between the experimentally determined and theoretically obtained members of equation 2 is reasonable in view of the complexity of the spectra and the resolution of the NaI(Tl) detectors. The discrepancies in these values may be attributed to the uncertainty in the determination of N_o, the precise location of the window boundaries, the presence of unknown coincidence makers and the 20% error associated with the λ_j values.

e Levels Defined by Ground State Transitions

It is expected that in the decay of nuclides with high Q values, the density of high lying levels will be such as to give rise to many weak high energy transitions to the ground and lowest excited states. In principle, γ-γ coincidence experiments involving these high energy gamma rays should be capable of unravelling these transitions, however, the inherent resolution of the NaI(Tl) detectors makes such an analysis untrustworthy, except for the strongest photons. Thus the strongest

lines observed with Ge(Li) detectors ought to appear in γ-γ coincidence measurements and the absence of strong coincidence peaks of the appropriate energy may be taken as evidence that the gamma ray in question is a ground state transition. Such arguments lead to the establishing of levels at 4.649, 4.492, 4.368, 4.138, 4.080, 1.760 and 1.370 MeV.

f Transitions and Levels Based on Energy Fits

It is evident from the Ge(Li) spectra that a number of weak high energy gamma rays exist which have not as yet been classified. Because of their intensity the γ-γ coincidence experiments are unable to yield unambiguous evidence for their existence. Experiments performed with high energy windows demonstrate that many of these weak photons must be included in the decay scheme in order to account for the observed data. Therefore on the basis of these experiments and on energy fits a number of photons has been incorporated into the decay scheme mainly as stop-over transitions from previously defined levels. In addition several levels have been defined on this basis - 3.732, 3.961, 4.184, 4.481 and 4.626 MeV.

g ^{89}Kr Beta Ray Spectrum Measurements

The ^{89}Kr beta ray spectrum was studied by use of a 5 cm x 5 cm plastic beta detector. The method of source preparation and the techniques used in this study were described in Chapters III and IV. The detection system was calibrated by accumulation of the beta ray spectra of ^{38}Cl (end point at 4.915 $\pm$ .008 MeV)[85], ^{106}Ru (end point at 3.540 $\pm$ .010 MeV)[7] and ^{90}Sr - ^{90}Y (end points at 0.544 $\pm$ .004, 2.270 $\pm$ .010 MeV)[7]. Two ^{89}Kr beta spectra (source strengths differing by a factor of two) were accumulated on the same gain as the standards. These spectra as well as

those of the standards were corrected for background, random sum contributions[74]* and the response functions of the plastic beta detector using techniques previously described (see Chapter V). These corrected spectra were then computor analysed for their end points and partial beta groups by means of the parabolic least squares technique[66] which made use of the energies of the levels populated in the decay of ^{89}Kr which were accurately known from the Ge (Li) and γ-γ coincidence data.

The left section of Figure 45 presents Fermi plots of an ^{89}Kr spectrum and a ^{38}Cl calibration spectrum. The end points of these spectra occur within one channel ($\sim$ 26 keV) of each other and hence a comparison between them is insensitive to non linearities in the detection system. The ^{89}Kr end points derived from the analysis depend slightly on the assumptions made concerning which levels in ^{89}Rb are fed by the beta rays. Table 12 summarizes the information obtained from two analysis of the two beta spectra.

TABLE 12

Intensity Analysis of Beta Singles Spectra

Source Number	MeV Maximum End Point	Q Value MeV	Level Fed			$\chi^2/_f$	Total Intensity	
			0	0.221	0.577+0.586		from Betas	from γ's
1	4.939	5.16		8.2	4.8	1.24	13.0	
2	4.925	5.15		10.3	3.7	0.94	14.0	19 ± 10
1	4.909	4.91	9.8		7.1	2.1	16.9	
2	4.902	4.90	11.2		4.5	1.4	15.7	

* A computer program which calculated these contributions was kindly provided by Dr. G. L. Keech of this laboratory.

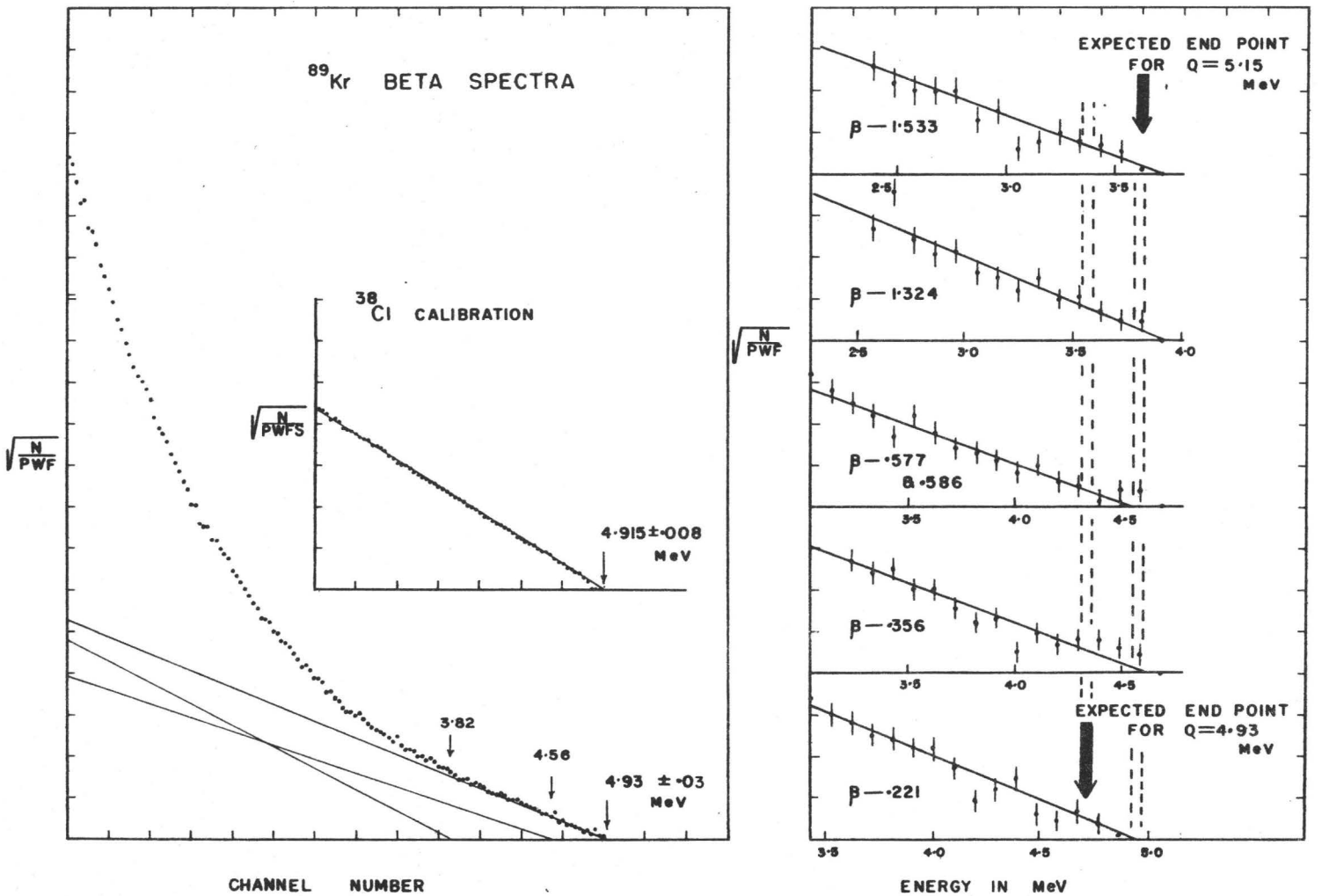

FIGURE 45 Kr BETA SINGLES AND BETA GAMMA COINCIDENCE SPECTRA

In the first analysis it was assumed that the highest energy beta rays fed the 0.221 MeV level, that the first inner group fed the closely spaced levels at 0.577 and 0.586 MeV and that the remaining beta rays populated higher lying levels at 1.324, 1.692 etc. MeV. The end points of the beta rays feeding the 0.221 MeV state and the intensities of the partial beta groups populating this level and the 0.577 + 0.586 MeV doublet are tabulated in the first rows of Table 12. The second two rows present the results of a similar analysis carried out on the assumption that the beta rays fed the ground and the 0.577 + 0.586 MeV states. Although the intensities of the partial beta spectra vary from analysis to analysis and depend on the assumptions made, the total intensity feeding the first four levels in ^{89}Rb is relatively insensitive to the model assumed. The mean value of 15% is in excellent agreement with the 19% figure derived from the gamma intensities. It might be remarked that the 19% figure represents an upper limit since almost certainly, transitions to these levels have been missed.

Although from these data, it is impossible to decide whether the Q value of the decay is 5.15 MeV or 4.93 MeV, the coincidence data shows a clear preference for the higher value. It may be significant that the goodness of fit of the model to the data is better for the higher Q value assumption.

Accepting the conclusion that there are very few beta rays feeding the ground state, the two experiments yielded ^{89}Kr end points of 4.925 and 4.939 MeV populating the 0.221 MeV level. The agreement of these values is better than one has any right to expect with an energy dispersion of 26 keV/channel and is considered fortuitous. A value of 4.93$\pm$.03

MeV has therefore been adopted for this end point.

h Beta Gamma Coincidence Measurements

The beta gamma coincidence measurements were performed with a 7.6 x 7.6 cm NaI(Tl) detector and a 5 cm x 5 cm plastic beta detector in conjunction with a 64 x 64 multi channel analyser. Calibration of the detection system was achieved by a β-γ coincidence experiment performed with ^{38}Cl. This method of calibration removed the possibility of analyser created channel shifts between the accumulation of standard and ^{89}Kr coincidence spectra. A computor analysis of the ^{89}Kr beta-gamma coincidence data produced a set of corrected Fermi plots of the beta rays in coincidence with ^{89}Kr gamma rays some of which are shown in the right section of Figure 45.

Despite the fact the data was acquired on a analyser grid of 94 kev/channel, the data of Figure 45 clearly shows that the Q of the decay is 5.15 MeV, corresponding to 4.93 + 0.22 MeV rather than 4.93 MeV. To demonstrate this fact, the energy scales of the various β-γ coincidence spectra presented in the figure have been shifted laterally to place the end points expected on the basis of a Q of 5.15 MeV vertically above one another. The observed end points of these spectra are consistant only for the higher Q value. The width of the two heavy arrows in the figure and the separation of the dotted lines represent the uncertainty in the end points expected from errors in calibration. The ^{38}Cl sources were obtained by irradiating 1.5 mg/cm^2 "saran-wrap" so the beta rays from this source passed through an average thickness of 0.75 mg/cm^2. The ^{89}Kr gas, on the other hand, was observed through a 0.91 mg/cm^2 window of

mylar. Since the stopping power of these materials for beta rays of energy 4 MeV is $\approx$ 1.9 keV/mg/cm^2, the corrections for window or source absorption are completely negligible.

i Decay Scheme - Discussion

The results of the sequence of experiments described in the previous sections are summarized in the decay scheme of ^{89}Kr presented in Figure 46. The Q value of the decay is 5.15 $\pm$ .03 MeV. The intensities of the photons shown in the figure and in Tables 8 and 9 are absolute values computed on the basis of the total gamma ray intensity populating the ground state. For purposes of normalization this total intensity has been increased by 1.5% to allow for possible beta transitions to the ground state and by 1% to account for ground state gamma ray transitions unclassified or unobserved in this study. The intensities of the partial beta groups populating the excited states have been arrived at in a similar manner; that is by computing the total intensity of the depopulating gamma rays less the total intensity of the radiations entering the level. These values as well as the computed $\log_{10} f_o t$ values are presented in Table 13. This table also lists the energies and estimated errors of the levels defined, the end points of the beta transitions to the levels, and the variances associated with both the intensities and computed $\log_{10} f_o t$ values. The final two columns of this table will be discussed below.

The levels defined at 0.221, 0.498, 0.577, 0.586, 0.998, 1.324, 1.533, 1.692, 2.400, 2.596, 2.618, 2.866, 3.364, 3.534, 3.720, 3.905, 3.976, 4.145, 4.342 and 4.368 MeV are strongly supported in many ways and are regarded as securely established. The levels at 1.998, 2.161 and 4.224 MeV have been established on the basis of coincidence data

FIGURE 46 DECAY SCHEME OF $^{89}_{36}Kr_{53}$

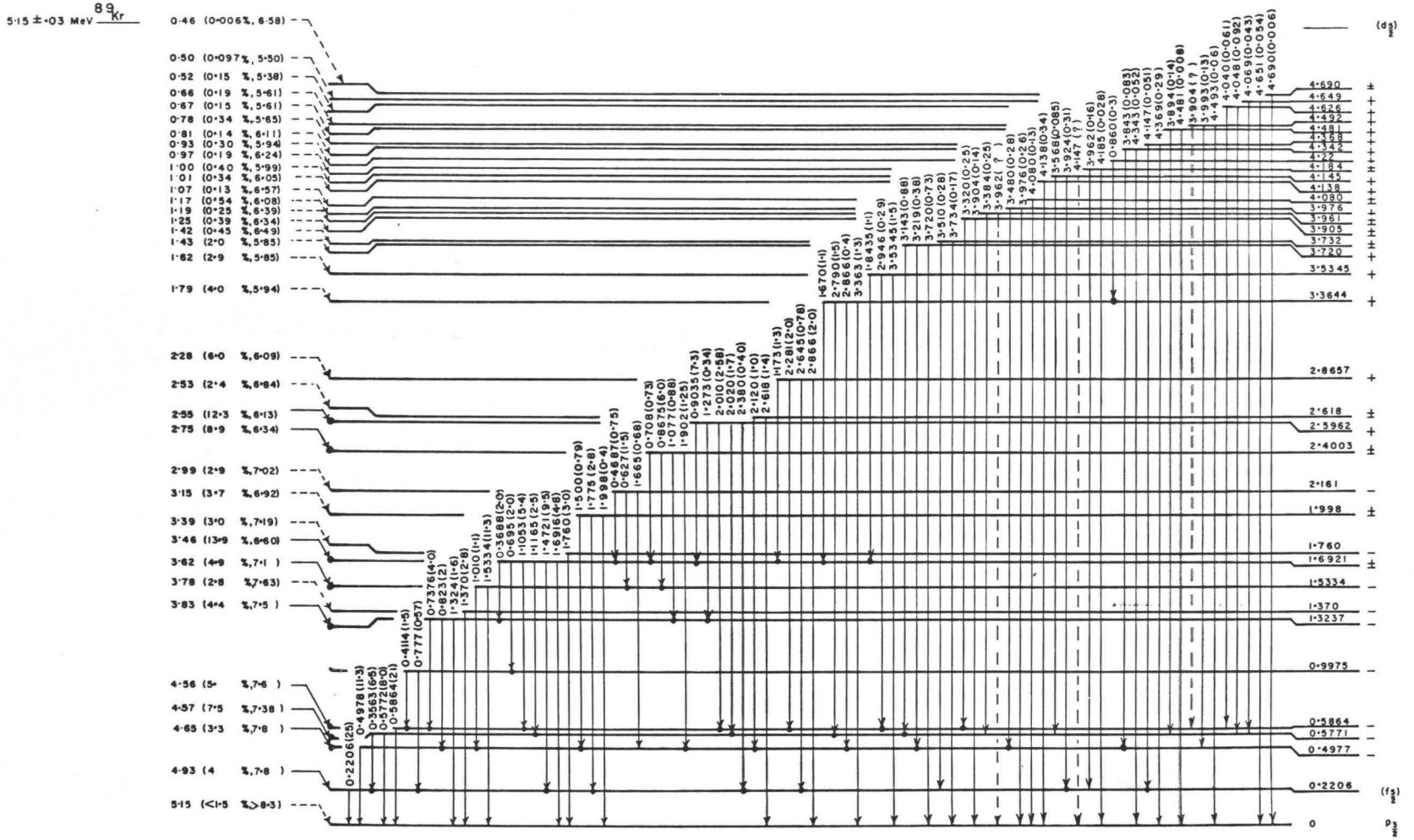

TABLE 13

Beta End Points and $Log_{10} f_o t$ Values

Proposed Level Energy E MeV	Estimated $\sigma(E)$ MeV	Beta End Point MeV	γ Intensity out-γ intensity in ΔI %	Estimated $\sigma(\Delta I)$	$Log_{10} f_o t$	Estimated σ(log ft)	Level parity	Spin
0		5.15	$\leq$ 1.5		$\geq$ 8.31		-	3/2
0.2206	.0003	4.93	3.70	3.48	7.84	$^{+1.2}_{-.3}$	-	(5/2)
0.4977	.0003	4.65	3.34	1.88	7.76	$^{+.4}_{-.2}$	-	
0.57705	.00025	4.57	7.45	1.4	7.38	$^{+.1}_{-.08}$	-	
0.5864	.0003	4.56	4.83	2.73	7.57	$^{+.46}_{-.2}$	-	
0.9975	.0010	4.15	0.07	0.36				
1.3237	.0007	3.83	4.38	1.34	7.46	$^{+.17}_{-.12}$	-	
1.370	.001	3.78	2.8	0.5	7.63	$^{+.08}_{-.09}$	-	
1.5334	.001	3.62	4.9	2.25	7.12	$^{+.27}_{-.2}$	-	
1.6921	.0007	3.46	13.92	2.42	6.60	$^{+.08}_{-.07}$	$\pm$	
1.760	.002	3.39	3.0	0.6	7.19	$^{+.1}_{-.08}$	-	
1.998	.001	3.15	3.74	0.63	6.92	$^{+.07}_{-.07}$	$\pm$	
2.161	.001	2.99	2.93	0.12	7.02	$^{+.02}_{-.02}$	-	
2.4003	.0008	2.75	8.86	0.94	6.34	$^{+.05}_{-.05}$	$\pm$	
2.5962	.0008	2.55	12.32	1.18	6.13	$^{+.05}_{-.04}$	+	
2.618	.0008	2.53	2.38	0.42	6.84	$^{+.13}_{-.07}$	$\pm$	
2.8657	.0015	2.28	5.98	0.77	6.09	$^{+.06}_{-.05}$	+	

(continued)

Proposed Level Energy E MeV	Estimated $\sigma(E)$ MeV	Beta End Point MeV	γ Intensity out-γ intensity in ΔI %	Estimated $\sigma(\Delta I)$	$\text{Log}_{10} f_o t$	Estimated σ(log ft)	Level parity	Spin
3.3644	.0020	1.79	3.95	0.57	5.94	$^{+.02}_{-.09}$	+	
3.5345	.0020	1.62	2.93	0.50	5.85	$^{+.08}_{-.07}$	+	
3.720	.0015	1.43	1.99	0.21	5.85	$^{+.06}_{-.04}$	+	
3.732	.002	1.42	0.45	0.067	6.49	$^{+.07}_{-.07}$	±	
3.905	.002	1.25	0.39	0.058	6.34	$^{+.07}_{-.06}$	±	
3.961	.002	1.19	0.25	0.05	6.39	$^{+.11}_{-.05}$	±	
3.976	.002	1.17	0.54	0.11	6.08	$^{+.1}_{-.08}$	+	
4.080	.002	1.07	0.13	0.03	6.57	$^{+.11}_{-.09}$	±	
4.138	.002	1.01	0.34	0.07	6.05	$^{+.1}_{-.06}$	+	
4.145	.002	1.00	0.395	0.036	5.99	$^{+.04}_{-.04}$	+	
4.184	.004	0.97	0.188	0.03	6.24	$^{+.10}_{-.04}$	±	
4.224	.020	0.93	0.30	0.10	5.94	$^{+.20}_{-.11}$	+	
4.342	.002	0.81	0.135	0.019	6.11	$^{+.07}_{-.06}$	+	
4.368	.003	0.78	0.341	0.078	5.65	$^{+.11}_{-.09}$	+	
4.481	.002	0.67	0.148	0.028	5.61	$^{+.09}_{-.07}$	+	
4.492	.002	0.66	0.19	0.032	5.61	$^{+.08}_{-.06}$	+	
4.626	.002	0.52	0.153	0.024	5.38	$^{+.08}_{-.06}$	+	
4.649	.003	0.50	0.097	0.015	5.50	$^{+.07}_{-.07}$	+	
4.690	.003	0.46	0.006	0.0015	6.58	$^{+.1}_{-.1}$	±	

$\Sigma \Delta I = 99.653$

involving weaker gamma rays which are partially masked by more intense photons and are therefore supported by a less firm body of data than the levels of the previous list. In this category of reasonably secure levels one must place those of energy 4.080, 4.138, 4.481, 4.492 and 4.649 MeV, which although depopulated by intense ground state transitions, are not supported by coincidence data. Finally, the levels at 1.370, 1.760, 3.732, 3.961, 4.184, 4.626 and 4.690 must be regarded as tentative.

From the previous work on ^{89}Rb decay and from the shell model it is expected that the ground states of ^{89}Rb and ^{89}Kr will be $p_{3/2}^{-1}$ and $d_{5/2}$ respectively. In addition, systematics of rubidium nuclei in the region show that the $f_{5/2}^{-1}$ level will occur as the first excited state. Thus first forbidden beta transitions are expected to the lowest lying levels of ^{89}Rb. Although our data is not conclusive for the ground state transition, it does appear as if first forbidden transitions are involved in the population of the lowest 4 levels. Therefore on this basis negative parity is assigned to these levels and their spins restricted to the range (3/2, 5/2, 7/2). The beta decay processes to the levels from $\sim$ 2.6 to 4.6 MeV appear to be made up primarily of allowed transitions. To these levels we assign positive parity and spin values in the range (3/2, 5/2, 7/2).

It does not appear that any information regarding spins can be meaningfully extracted from the data on the basis of gamma ray transitions. In the study of ^{89}Rb decay, this technique proved useful since there were relatively few transitions, little contamination and the spins of the lowest lying levels had been established from reaction work.

In the present study the number of gamma rays, both real and contaminant, allows the placing of lower limits on possible transition intensities in the region below 0.67 MeV to values differing only by a factor of ~ 50 from the strongest lines. Thus the basis of the method is destroyed and the absence of a transition proves nothing.

CHAPTER VIII

DISCUSSION OF RESULTS

a Introduction

The results of d-p, d-t, d-d' reaction experiments on strontium [62,63,64], yttrium[86,87], zirconium[68,88,89], niobium[90,91] and molybdenum[92] nuclei with $Z \geq 38$ and $N \geq 50$ have shown that the level structure of these nuclei are predominately single particle in nature or are simple configurations involving $d_{5/2}$, $s_{1/2}$ and $d_{3/2}$ neutrons and $p_{1/2}$ and $g_{9/2}$ protons. Since these orbitals are separated by fairly large energies the shell model is expected to give an accurate picture of the level structure of these nuclei. Talmi et al[20] were the first workers to carry out shell model calculations using the effective interaction method to some of these nuclei. When more refined data became available, these workers[93] and many others[90,94,95] greatly extended their calculations and showed that the shell model representation does give an excellent account of the observed structures. An extension of the original work by Talmi et al[20] to nuclei immediately below Z = 38 has been hampered by lack of experimental data. D-p reactions, however, performed by Sass et al[64] on ^{87}Kr, have shown that the lowest lying levels of this nuclide are reasonably pure single particle states. Thus the shell model would appear to be adequate to account for the observed structures of nuclei falling immediately below the closed 38 proton-shell.

The pairing plus quadrupole model of Kisslinger and Sorensen is an alternative mode of description for nuclei in this mass region. In this

representation the level structures may be interpreted as arising from $d_{5/2}$, $s_{1/2}$ and $d_{3/2}$ neutron quasiparticles and $p_{1/2}$ and $g_{9/2}$ or $p_{3/2}$ and $f_{5/2}$ proton quasiparticles. The coupling of these quasiparticles to collective core excitations should yield a large number of additional low lying levels. Alster et al[96] by means of α-α' reactions have attempted to identify such particle-vibrational levels in ^{88}Sr and ^{89}Y. Their preliminary results indicate that such couplings are questionable and that the observed level structures of these nuclei are better accounted for by the simple shell model. The evidence of these workers suggests that the previously considered vibrational levels of ^{88}Sr at 1.83 and 3.21 MeV are in fact configuration mixtures of proton and neutron particle-hole states. Thus, although alternative representations are available, it appears that the shell model gives better results when applied to low lying levels of nuclei in the mass 90 region.

b The Level Structure of ^{89}Sr

The Q value of 4.486 ± 0.012 MeV for the decay of ^{89}Rb to ^{89}Sr is in sharp disagreement with the value of 3.92 MeV obtained by O'Kelley et al[60] but is in good agreement with the aluminum absorption value of 4.5 MeV obtained by Bleuler and Zunti[59]. Our value of 4.486 MeV agrees well with the mass table value of Everling, Gove and Van Lieshout[97] and with the 1964 Mass Table of Mattauch et al[85].

Sass et al[64] have shown that the $d_{5/2}$ ground state and the $s_{1/2}$ and $d_{3/2}$ excited state at 1.03 and 2.00 MeV have spectroscopic factors of 0.7, 0.8 and 0.5 respectively. These results indicate that while collective effects cannot be completely ignored the lower lying levels of ^{89}Sr are predominantly single particle in character. The 1.031 and 2.000

MeV levels are thus interpreted as arising from the excitation of a single $d_{5/2}$ neutron outside the closed shell of 50 neutrons to $s_{1/2}$ and $d_{3/2}$ orbitals respectively.

It is interesting to speculate on the origin of the negative parity states that are populated in the beta decay process. Since no such levels are energetically available above the closed neutron shell these levels are interpreted as arising from the breaking of a $p_{1/2}$ neutron pair below the closed shell and the promoting of one of these neutrons to higher orbitals. The observed 1/2- states may be described by configurations of the form $(p_{1/2})^{-1}\left[\alpha^2(d_{5/2}{}^2)_o + \beta^2(s_{1/2}{}^2)_o + \gamma^2(d_{3/2}{}^2)_o\right]$. In the same way the 5/2- states may arise from the coupling of the $p_{1/2}$ hole states to configurations involving $d_{5/2}{}^2$ and $d_{3/2}{}^2$ particle states of seniority two.

The ground state of $^{89}_{37}Rb_{52}$ is presumably a configuration mixture of the form

$p_{3/2}^{-1}\left[\alpha'^{\,2}(d_{5/2}{}^2)_o + \beta'^{\,2}(s_{1/2}{}^2)_o + \gamma'^{\,2}(d_{3/2}{}^2)_o\right]$. Since the beta decay matrix elements involve one body of operators, it would be expected that in the event the β' and γ' coefficients are small the beta transitions to the $s_{1/2}$ and $d_{3/2}$ levels of ^{89}Sr would be hindered relative to the $d_{5/2}$ ground state transition. Such a hindrance accounts for the large first forbidden $\log_{10} f_o t$ values observed. In the same fashion, fast, allowed transitions would be expected to the 1/2- states because of the excellent overlap between these and the ^{89}Rb ground state wave functions. This expectation is verified for the transition to the 3.225 MeV level which has a $\log_{10} f_o t$ value of 5.

c The Level Structure of ^{89}Rb

The Q value of 5.15 ± 0.03 MeV reported in this work is in considerable disagreement with the 4.6 MeV value found by Wahlgren et al[53]. Mattauch et al[85] in their mass table have used Wahlgren's value but have pointed out that an increase in the Q value of ^{89}Kr by 0.7 ± 0.5 MeV is indicated from regularities in Q value systematics.

The d-p reaction work of Sass et al[64] on ^{87}Kr has shown that this nuclide has a $d_{5/2}$ ground state configuration. On the basis of these results and the shell model, it is expected that ^{89}Kr will have a $|\, d_{5/2}{}^{3}\ J = 5/2\rangle$ ground state configuration. Since ^{89}Rb and ^{87}Rb[7] both have $p_{3/2}{}^{-1}$ ground state configurations the level structures of these nuclei as seen through the decay of their krypton parents should possess a certain degree of similarity.

It is evident from Figure 47, that the addition of a neutron pair to ^{87}Rb results in a large number of additional levels in ^{89}Rb. The lowest lying of these are mainly negative parity states whose origin may be attributed to configuration mixtures of $p_{3/2}^{-1}$ and $f_{5/2}^{-1}$ proton holes and $d_{5/2}{}^{2}$ and $d_{3/2}{}^{2}$ states of seniority two and $d_{5/2}{}^{2}$, $s_{1/2}{}^{2}$ and $d_{3/2}{}^{2}$ states of seniority zero. Such configurations give rise to a large number of states whose spins are consistant with the observed beta decay patterns.

Positive parity states first appear in ^{87}Rb at about 3 MeV and in ^{89}Rb at ≈ 2.5 MeV. These states are associated with large excitation energies and complex configurations are thus expected. These high lying levels in ^{89}Rb may be accounted for by configurations of the form

$$|g_{9/2}\ (p_{3/2}^{-2}(o))\ d_{5/2}{}^{2}(v=2)\ \ J\rangle\ ,\ |g_{9/2}\ (f_{5/2}^{-2}\ (o))\ d_{5/2}{}^{2}(v=2)\ J\rangle$$

FIGURE 47 LEVEL STRUCTURE OF ^{89}Rb AND ^{87}Rb

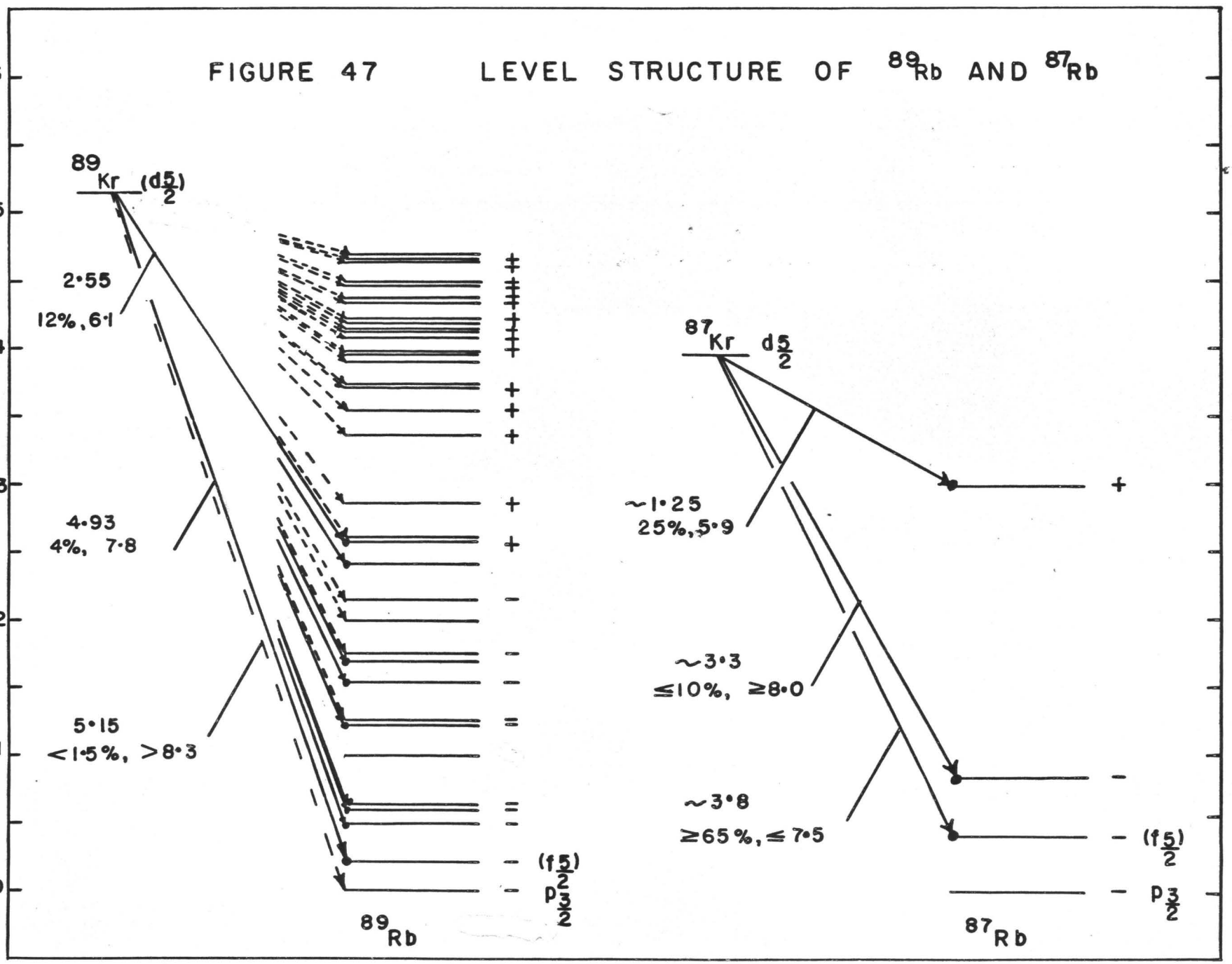

$|g_{9/2}\ (p_{3/2}^{-2}(v=2))\ d_{5/2}{}^{2}(o)\ J\rangle$ and $|g_{9/2}(f_{5/2}^{-2}(v=2))\ d_{5/2}{}^{2}(o)\ J\rangle$.

The beta decay patterns to the lowest lying levels of both ^{87}Rb and ^{89}Rb are quite similar in that the ground state transitions appear to be hindered relative to the transitions to the first excited states. It is reasonable to assume that the first excited states of both these nuclei are $f_{5/2}^{-1}$ hole configurations. If the ground state wave functions of the ^{87}Kr and ^{89}Kr parent nuclides are predominantly in $|f_{5/2}^{-2}\ d_{5/2}\ J=5/2\rangle$ and $|f_{5/2}^{-2}\ d_{5/2}{}^{3}\ J=5/2\rangle$ states respectively then the beta transitions to the $p_{3/2}^{-1}$ states in the rubidium daughters will be hindered. Thus the beta decay patterns to the lowest lying states of these nuclides may be accounted for by configuration mixing.

REFERENCES

1. Pauli, W. 1933, Noyaux Atomique, Proc. of the Solvay Congress, Brussels.

2. Cowan, C. L., Reines, F. Phys. Rev. 107, 528 (1957).

3. Fermi, E. Physik, 88, 161 (1934).

4. Segre, E., Nuclei and Particles, W. A. Benjamin, Inc., New York (1964).

5. Kotani, T., Ross, M. Phys. Rev. 113, 662 (1959).

6. Preston, M.A., Physics of the Nucleus, Addison Wesley Pub. Co., Reading Massachusetts (1962).

7. Nuclear Data Sheets (Natl. Acad. Sci. National Research Council Publ. Washington, D.C.)

8. Blatt, J. M., Weisskopf, V.F., Theoretical Nuclear Physics (J. Wiley and Sons, New York, 1952).

9. Siegbahn, K., editor, Alpha-Beta and Gamma-Ray Spectroscopy (Interscience Publishers Inc. New York).1965.

10. Brink, D. M., Nuclear Forces (Pergamon Press, Oxford 1965).

11. Bruec ner, K. A., Phys. Rev. 96, 508 (1954).

12. Brueckner, K. A., Levinson, C. A., Mahmoud. Phys. Rev. 95, 217 (1954).

13. Brueckner, K. A., Phys. Rev. 97, 1353 (1955).

14. Brueckner, K. A., Levinson, C.A., Phys. Rev. 97, 1344 (1955).

15. Mayer, M., Phys. Rev. 75, 1969 (1949).

16. Haxel, O., Jensen, J. H. D. and Suess, H. E., Phys. Rev. 75, 1766 (1949).

17. De Shalit, A., Talmi, I. Nuclear Shell Theory, (Academic Press, New York 1963).

18. Racah, G., and Talmi, I., Physica 18, 1097 (1952).

19. French, J. B., Nuclear Phys. 15, 393 (1960).

20. Talmi, I., Unna, I., Nuclear Phys. 19, 225 (1960).

21. Nilsson, S. V., Dan. Mat. Fys. Medd. 29 No. 16 (1955).

22. Bohr, A. and Mottelson, B., In β and γ-Ray Spectroscopy (edited by K. Siegbahn) North Holland, Amsterdam (1955).

23. Bohr, A., Mottelson, B. R. and Pines, D., Phys. Rev. 110 (936) (1958).

24. Bardeen, J., Cooper, L. N. and Schrieffer, H. Phys. Rev. 108, 1175 (1957).

25. Belyaev, S. T., Mat. Fys. Medd. 31, 11 (1959).

26. De Benedetti, S. (John Wiley and Sons, New York) (1964).

27. Kisslinger, L. S. and Sorensen, R. A., Mat. Fys. Medd., 32,9 (1960).

28. Hahn, O. and Strassman, F., Naturwiss 27, 11 (1939).

29. Hahn, O. and Strassman, F., Naturwiss 27, 89 (1939).

30. Meitner, L. and Frisch, R. O., Nature 143 239, 471 (1939).

31. Anderson, H. L., Fermi, E., Grosse, A. V., Phys. Rev. 59, 52 (1941).

32. Katcoff, S., Nucleonics 18, 201 (1960).

33. Thode, H. G., Graham, R. L., Can. J. Research 25A, 1 (1947).

34. Farrar, H., Tomlinson, R. H., Can. J. Phys. 40,1017 (1962).

35. Farrar, H., Tomlinson, R. H., Nuclear Phys. 34, 367 (1962).

36. Wahl, A. C., Paper No. SM-60/22, IAEA Symposium on Physics and Chemistry of Fission, Salzburg, Austria 1965.

37. Glendenin, L. L., Coryell, C. D. and Edwards, R. R. (Radiochemical Studies: "The Fission Products", Coryell, C. D., and Sugarman, N., Editors, National Nuclear Energy Series, Plutonium Project Record, McGraw Hill Book Co. Inc., New York (1951)).

38. Norris, A. E., Wahl, A. C. Phys. Rev. 146,926 (1966).

39. Wolfsberg, K., Phys. Rev. 137 4B 929 (1965).

40. Wahl, E., Ferguson, R. L., Nethaway, D. R., Troutner, D. E., Wolfsberg, K. Phys. Rev. 126,1112 (1962).

41. Hyde, E. K. (The Nuclear Properties of the Heavy Elements) Prentice Hall Inc., Englewood Cliffs, New Jersey (1964).

42. Wolfsberg, K., LA-3169 (1965).

43. Events, J. E., Fluharty, R. G., Nuc. Sci. Eng. 8, 66 (1960).

44. Safford, G. J., Havens, W. W., Nucleonics 17 NO61 134 (1959).

45. Leonard, B. R. in "Neutron Physics", M. L. Yeater, Ed., Academic Press, New York (1962).

46. Glueckauf, E., Proc. Phys. Soc. 61, 25 (1948).

47. Dewdney, J.W., Nuclear Phys. 43, 303 (1963).

48. Dillard, J. W., Adams, R. M., Finston, H. and Turkevich, A. (Radio-Chemical Studies "The Fission Products", Coryell, C. D. and Sugarman, N. Editors, National Nuclear Energy Series, Plutonium Project Record, McGraw Hill Book Co. Inc., New York (1951).

49. Kofoed-Hansen, O. and Nielson, K. O., Phys. Rev. 82, 96 (1951).

50. Wahl, A. C. and Bonner, N. A. (Radioactivity Applied to Chemistry), Chapt. 9, John Wiley, New York (1951).

51. Prakash, S., Z. Electrochem. 64, 1037 (1960).

52. Koch, R. C. and Grady, G. L. , Anal. Chem. 33, 43 (1961).

53. Wahlgren, M. A. and Meinke, W. W., J. Inorg. Nucl. Chem. 24, 1527 (1962).

54. Ockenden, D. W. and Tomlinson, R. H., Can. J. Chem. 40, 1594 (1962).

55. Goodman, R. H., Kitching, J. E. and Johns, M. W., Nuclear Phys. 54, 1 (1964).

56. Seelman-Eggebert and Born, H. J., Naturwiss, 31, 59 (1943).

57. Hahn, O. and Strassman, F., Naturwiss 28, 455 (1940).

58. Glasoe, G. N. and Steigman, J., Phys. Rev. 58, 1(1940).

59. Bleuler, E., and Zunti, W., Helv. Phys. Acta, 19, 375 (1946).

60. O'Kelley, G. D., Lazar, N. H. and Eichler, E.,(1956)Phys. Rev. 102, 223.

61. Johnson, N. R., O'Kelley, G. D., Eichler, E., Phys. Rev. 135 B 36 (1964).

62. Cohn, B. L., Phys. Rev. 125, 1358 (1962) .

63. Preston, R. L., Sampson, M. B. and Martin, H. J., Can. J. Phys. 42, 1321, (1964).

64. Sass, R. E., Rosner, B., Schneid, J., Phys. Rev. 138 B 397 (1965).

65. Fiedler, H. J. To be published.

66. Archer, N. P., Ph.D. Thesis, McMaster University 1965.

67. Klein, O., and Nishina, Y., Z. Physik 52 853 (1929).

68. Breitenberg, E., (Progress in Nuclear Physics) Vol. 4, p 56, Pergamon Press, New York (1955).

69. Crouthamel, C. E. (Applied Gamma-Ray Spectroscopy) Pergamon Press, New York 1960.

70. Engelkemeir, D., Rev. Sci. Instr., 227 (No. 8), 589 (1956).

71. Pell, E. M. J. Appl. Phys. 31, 291 (1960).

72. Freedman, M. S., Novey, T. B., Porter, F. T. and Wagner, F. Jr., Rev. Sci. Instr. 27, 716 (1956).

73. Habib, E. E., Ph.D. Thesis, McMaster University, Hamilton (1961).

74. Kennett, T. J., Prestwich, W. V., Keech, G. L., Nuc. Inst. and Meth. 29 325 (1964).

75. Guinn, V. P. and Lash, J. E. NAS-NS-3107 (1962).

76. Heath, R. L. IDO-16784 (1962).

77. Milne, W. E., Numerical Calculus (Princeton University Press, Princeton, New Jersey 1949).

78. Storm, E., Gilbert, E., Israel, H. La-2237 (1958).

79. Heath, R. L. iDO-16408 (1957).

80. Johnson, N. R., Eichler, E., O'Kelley, G.D., Chase, J. W., Wasson, J. T., Phys. Rev. 122, 1546 (1961).

81. Eichler, E., O'Kelley, G. D., Robinson, R. L., Marinsky, J. A., Johnson, N. R., Nuclear Phys. 35, 625 (1962).

82. Slavinskas, D. D., Kennett, T. J. and Prestwich, W.V., Nuc. Inst. and Meth. 37, 36 (1965).

83. Murry, G., Graham, R.L. and Geiger, J. S., Nuclear Phys. 63, B53 (1965).

84. Archer, N. P., Lycklama, H., private communication.

85. Mattauch, J.H., Thiele, W., Wapstra, A. H., Nuc. Phys. 67, 1 (1965).

86. Hamburger, A.I. and Hamburger, E. W. Phys. Lett. 4 (1943) 223.

87. Watson, C., Moore, C.F., Sheline, R. K., Nuclear Physics 54 (1964) 519.

88. Cohen, B. L., Chubinsky, O.V. Phys. Rev. 131 (1963) 2184.

89. Jolly, R. K., Lin, E. K., Cohn, B.L. Phys. Rev. 128 (1962)2292.

90. Sweet, R. F., Bhatt, K. H., Ball, J. B. Phys. Lett. 8 (1964) 131.

91. Sheline, R. K., Watson, C., Hamburger, E.W., Phys. Lett. 8 (1964) 121.

92. Hjorth, S. A., Cohen, B. L. Phys. Rev. 135 (1964) B920.

93. Auerbach A., Talmi, I. Nuclear Physics 64 (1965) 458.

94. Cohen, S., Lawson, R.D., Macfarlane, M. H., Soga , M., Phys. Lett. 10 (1964) 195.

95. Vervier, J. Nuclear Physics 75 (1966), 17.

96. Alster, J., Shreve, D.C., Peterson, R.J. Phys. Rev. 144 (1966) 999.

97. Everling, F., Gove, N.B., Van Lieshout, R. 1961
Nuclear Data Sheets, NRC 61-3-146.